The Henryk Niewodniczański Institute of Nuclear Physics

Polish Academy of Sciences

ELECTRON INJECTION AT HIGH MACH NUMBER NONRELATIVISTIC PERPENDICULAR SHOCKS

Artem Bohdan

**Thesis submitted for the degree of Doctor of Philosophy
prepared under the supervision of dr. hab. Jacek Niemiec**

Kraków, 2017

ACKNOWLEDGEMENT

I would like to extend my gratitude to my PhD supervisor dr. hab. Jacek Niemiec, who gave me the possibility to start this project at The Henryk Niewodniczański Institute of Nuclear Physics Polish Academy of Sciences, and great thanks for his guidance, enormous help and support during all the time of my studies and thesis preparation.

Many thanks to my colleagues dr. Oleh Kobzar, Arianna Ligorini and Oleksandr Sushchov for their valuable advices and help in my research. I also thank prof. Martin Pohl for great support and interesting and fruitful discussions. Finally, I express sincere thanks to my family for their love and confidence through the past years.

ABSTRACT

It is generally believed that galactic component of cosmic rays (CRs) are produced by supernova remnant (SNR) shocks. SNR paradigm states that CR are accelerated via diffusive shock acceleration (DSA). To be accelerated via DSA mechanism particles with relativistic energies are needed. This, the so-called injection problem, is the most difficult and still unresolved issue of DSA theory. Electron injection mechanisms at high Mach number non-relativistic perpendicular shocks for the parameters that are applicable to young SNR shocks are under consideration here. Using two-dimensional kinetic particle-in-cell (PIC) simulations we explore the nonlinear shock structure and electron injection mechanisms for plasmas with low and moderate temperature (plasma beta $\beta_e = 5 \cdot 10^{-4}$ and $\beta_e = 0.5$), various orientations of the large-scale perpendicular magnetic field with respect to the simulation plane ($\varphi = 0^o, 45^o$ and 90°). Ion reflection off the shock leads to the formation of magnetic filaments in the shock ramp, resulting from Weibel-type instabilities, and electrostatic Buneman modes in the shock foot. In all cases electrons are strongly energized via the shock-surfing acceleration (SSA) mechanism in the shock foot. SSA efficiency and further acceleration mechanisms beyond SSA strongly depends on the large-scale magnetic field orientation. For strictly out-of-plane field ($\varphi = 90^o$) the fraction of supra-thermal electrons is much higher than for other configurations. Shocks in plasma with moderate temperatures provide more efficient electron pre-acceleration. For runs with $\varphi = 0^o$ and 45° the large-scale magnetic field configuration spontaneous turbulent magnetic reconnection in the shock ramp present additional channel of electron acceleration to nonthermal energies. Magnetic vortex statistics and properties are investigated. We demonstrate a dependence of the magnetic vortex generation rate on the temperature of the upstream plasma and also on numerical parameters of the simulations, such as the ion-to-electron mass ratio and the magnetic field orientation. We discuss the resulting electron spectra and the relevance of our results to the physics of fully three-dimensional systems.

STRESZCZENIE

Powszechnie uważa się, że galaktyczny składnik promieniowania kosmicznego jest produkowany w falach uderzeniowych pozostałości po wybuchach supernowych. Paradygmat ten przyjmuje, że cząstki promieniowania kosmicznego przyspieszane są w procesie dyfuzyjnej akceleracji na frontach fal uderzeniowych (*Diffusive Shock Acceleration*, DSA). Aby uczestniczyć w procesie DSA, cząstki muszą jednak wcześniej zostać przyspieszone do relatywistycznych energii. Jest to tak zwany problem injekcji (wrzucania) cząstek do procesów przyspieszania na szokach. Ten trudny problem w teorii DSA stanowi jedno z wciąż nierozwiązanych zagadnień. Przedmiotem badań przedstawionych w niniejszej pracy są mechanizmy wrzucania elektronów w nierelatywistycznych prostopadłych szokach o dużej liczbie Macha, z zastosowa-niem do szoków młodych pozostałości po supernowych. Badania prowadzone są za pomocą dwuwymiarowych kinetycznych symulacji numerycznych typu Particle-In-Cell (PIC) i dotyczą nieliniowej struktury szoków oraz procesów wrzucania elektronów w plazmie o niskiej i umiarkowanej temperaturze (parametr beta dla plazmy $\beta_e = 5 \cdot 10^{-4}$ i $\beta_e = 0.5$), dla różnych orientacji średniego prostopadłego pola magnetycznego względem płaszczyzny symulacji (kąty $\varphi = 0^o, 45^o$ and 90°). Odbicie jonów od fali uderzeniowej prowadzi do powstania włóknistej struktury pola magnetycznego w prekursorze fali, będącej wynikiem niestabilności Weibla, oraz wzbudzenia elektrostatycznych modów bunemanowskich w stopce szoku. We wszystkich badanych przypadkach elektrony zostają silnie przyspieszone w stopce szoku wskutek tzw. procesu serfowania na szoku (*Shock-Surfing Acceleration*, SSA). Efektywność tego mechanizmu, jak i następujących po nim procesów przyspieszania, silnie zależy od orientacji średniego pola magnetycznego. Dla konfiguracji z polem prostopadłym do płaszczyzny symulacji ($\varphi = 90^o$) frakcja nietermicznych elektronów jest znacznie większa niż dla innych orientacji. Szoki w plazmie o umiarkowanej temperaturze wrzucają elektrony efektywniej. Dla kątów $\varphi = 0^o$ oraz 45° obserwuje się w prekursorze zjawisko spontanicznej turbulentnej rekoneksji magnetycznej, które umożliwia dodatkowe przyspieszanie elektronów do wysokich energii. Badania efektywności występowania rekoneksji magnetycznej wykazują silną zależność tempa produkcji wirów magnetycznych od temperatury plazmy przed szokiem. Tempo to także zmienia się w badanym zakresie parametrów numerycznych, takich jak wielkość zredukowanej masy jonów oraz orientacja średniego pola magnetycznego. Wyznaczone rozkłady energetyczne elektronów są poddane szczegółowej analizie. Uzyskane wyniki omawiane są w kontekście Na podstawie uzyskanych wyników wsnioskuje się także o naturze badanych procesów w pełni trójwymiarowych układach.

TABLE OF CONTENTS

CHAPTER 1 – INTRODUCTION

CHAPTER 2 – COSMIC RAYS

CHAPTER 3 – SHOCKS IN COLLISIONLESS PLASMAS

CHAPTER 4 – PARTICLE ACCELERATION AT SHOCKS

CHAPTER 5 – PARTICLE-IN-CELL SIMULATIONS

CHAPTER 6 – PIC SIMULATIONS OF PERPENDICULAR SHOCKS

CHAPTER 7 – SUMMARY AND CONCLUSIONS

CHAPTER 1
INTRODUCTION

The Earth's atmosphere is constantly bombarded by high-energy cosmic ray particles coming from the Sun, the Galaxy, and extragalactic sources. It is generally believed that the main part of the galactic cosmic ray flux is produced at supernova remnants. Supernova star explosions release enormous amounts of matter moving with supersonic speeds. Interactions of this matter with interstellar medium lead to formation of shock waves. Theoretical models elaborated already in 1970s predict that charged particles can be accelerated to highly relativistic energies at strong shocks of supernova remnants via diffusive shock acceleration (a so-called first-order Fermi process). The resulting energy distribution of particles has a power-law form with spectral index $\alpha \sim 2$. Multiwavelength studies of supernova remnants provide direct evidence for high-energy particle production in these objects and particle spectra measured at sources are in good agreement with theoretical predictions. The most tantalizing still unresolved question in the diffusive shock acceleration theory concerns the particle injection problem. The first-order Fermi process works only for high-energy particles whose Larmor radii are larger than the width of the shock transition layer, which is typically of the order of several gyroradii of the thermal plasma protons. Thus to take part in the acceleration process particles need to be extracted from the thermal pool and pre-accelerated by some internal shock mechanism. The problem is more severe for electrons, on account of their lower mass and consequently smaller Larmor radii and inertial lengths, compared to protons.

The aim of this work is to investigate electron injection (pre-acceleration) processes at young supernova remnant shocks. Such shocks have nonrelativistic propagation velocities and are characterized by high sonic and Alfvénic Mach numbers. This work concentrates on perpendicular shocks, in which large-scale magnetic field is aligned with the shock surface. The physics of such shocks is governed by ion reflection at the shock ramp, interaction of which with the incoming plasma excites a variety of instabilities upstream of the shock. The most important instabilities in the regime of high Mach numbers is the electrostatic two-stream Buneman instability resulting from the interaction between cold incoming electrons and reflected ions and electromagnetic Weibel filamentation instability driven by the interaction of the incoming and reflected ions. As it will be presented in this theses these two instabilities are of profound consequence for the electron injection processes.

Electron injection is studied in this work with the method of kinetic particle-in-cell computer

simulations that offer a fully-self consistent description of collisionless plasmas. Large-scale shock simulations that resolve the electron scales with high precision are computationally demanding, and so our simulations are performed with two-dimensional numerical grids. However, a wide numerical parameter range covered in the simulations allows us to draw conclusions on the physics of fully three-dimensional systems. The numerical code used in this study can follow individual particle trajectories, thus providing detailed information on the acceleration processes.

Two electron pre-acceleration processes are scrutinized here in detail – the shock-surfing acceleration in the Buneman instability region in the shock foot and spontaneous turbulent magnetic reconnection in the shock ramp. These processes are studied systematically in a wide range of the physical and also numerical parameters.

The plan of this thesis is as follows:

- Chapter 2 gives a short introduction to the cosmic ray physics – the observed energy spectrum and current theories on galactic and extragalactic cosmic ray origin.

- Chapter 3 contains a description of the shock physics in collisionless plasmas. A basic structure of nonrelativistic perpendicular shocks is introduced and the main properties of the Buneman and the Weibel filamentation instabilities are presented.

- In Chapter 4 diffusive shock acceleration theory is described. The particle injection problem is introduced and the current status of the injection processes relevant to high Mach number shocks is summarized.

- Chapter 5 overviews the particle-in-cell simulation method. Application of this method to the shock physics is presented and a description of our simulation setup and test simulation runs is given.

- Chapter 6 describes results of numerical simulations performed in this work. Special attention is paid to the investigation of the shock surfing acceleration mechanism and the acceleration via spontaneous turbulent magnetic reconnection.

- Results of in this thesis, are summarized in the last Chapter 7. The importance and relevance of our results to the physics of astrophysical systems is discussed.

CHAPTER 2
COSMIC RAYS

2.1 Cosmic ray spectrum

More then a century ago Hess balloon experiments (Hess, 1912) showed an existence of ionized radiation at altitudes above 1 km which later become to be known as cosmic rays (CRs). CRs are charged particles with energies above 1 MeV which reach the Earth from our Galaxy and extragalactic sources. At energies less than about 1 GeV per nucleon CR spectra undergo strong variations because of the Solar activity. This phenomenon is known as the solar modulation. CR particles diffusively move from the interstellar space into the Earth's direction through the outflowing solar wind and therefore the flux of low-energy CRs becomes smaller during periods of high solar activity and larger when the solar activity is low.

CR flux strongly varies with energy and equals one particle per m^2 per second at energies about 10^{11} eV and drops to the value of one particle per km^2 per century for the highest measured CR energies reaching $3 \cdot 10^{20}$ eV. The energy spectrum of high energy (> 1GeV) CRs can roughly be described by a power-law distribution, $N(\varepsilon) \propto \varepsilon^{-\alpha}$, with the spectral index $\alpha \sim 3$, as shown in Figure 2.1. The spectrum has a few interesting and well known features: the "knee" at $\varepsilon \sim 3 \cdot 10^{15}$ eV, the "ankle" at $\varepsilon \sim 3 \cdot 10^{18}$ eV, and the GZK-cutoff at $\varepsilon \sim 5 \cdot 10^{19}$ eV. The power-law index of the CR spectrum for energies $< 10^{15}$ eV is $\alpha \simeq 2.7$ and it steepens to the value of $\alpha \simeq 3.1$ in the energy region close to 10^{15} eV forming the "knee". At the energy of the "ankle" the spectrum again flattens to $\alpha \simeq 2.7$. For energies higher than 10^{19} eV the spectrum is poorly known because of the low CR flux at such high energies and, consequently, large uncertainties in the flux measurements. However, at the energy range above $5 \cdot 10^{19}$ eV, a suppression of the flux is observed. This feature of ultra-high-energy cosmic rays (UHECR) is most likely due to the Greisen-Zatsepin-Kuzmin (GZK) cutoff (Greisen, 1966; Zatsepin & Kuzmin, 1966). On their way to the Earth the UHECRs undergo significant energy losses via interactions with the cosmic microwave background (CMB) radiation and pion-production processes. Nevertheless, it should be mentioned that the suppression of the CR spectra at high energies could also be related to the limited number of sources capable of producing physical conditions for the production of individual particles with energies up to and beyond 10^{20} eV.

The CR spectra are shaped by the acceleration processes at sources and the propagation in the interstellar or intergalactic medium filled with magnetic and radiation fields. The most basic classification of CRs is based on their origin: galactic and extragalactic CRs are respectively

produced by galactic (e.g., supernova remnants (SNRs), pulsar wind nebulae, binary systems) and extragalactic (e.g., jets of active galactic nuclei (AGN), gamma-ray bursts (GRB), galaxy clusters) sources. Changes of the power-law index of the CR spectrum at $\varepsilon \sim 3 \cdot 10^{15}$ eV and $\varepsilon \sim 3 \cdot 10^{18}$ eV can be explained by a transition between galactic and extragalactic components in the energy range where there is an intersection of the two CR flux components (Wibig & Wolfendale, 2004; Berezinsky et al., 2006; Allard et al., 2007; Hooper et al., 2007).

2.2 Galactic cosmic rays

A current paradigm of CR origin assumes that the most part of galactic CRs are produced at SNRs. Such an idea was first brought forth by Baade and Zwicky (1934). The main argument in support of this paradigm comes from the energy considerations. The average energy density of the galactic CRs is about $\sim 1 - 2$ eV/cm^3 (Webber, 1998). Taking into account the average time CRs spend in the Galaxy before escaping, the CR energy production rate is about 10^{41} erg/s (Ginzburg & Syrovatsky, 1961). An average supernova explosion energy is about 10^{51}erg. This, combined with the average galactic supernova explosion rate of 2-3 per century, gives the mean energy production rate of 10^{42} erg/s which means that about 10% of the total supernova explosion energy should be converted into the CR kinetic energy.

An interaction of supernova ejecta with the interstellar medium creates shock waves expanding into space. These shock waves are considered to be the main CR production sites. Particle energization at shocks proceeds through a so-called first-order Fermi acceleration process or diffusive shock acceleration (DSA, see Sec. 4.1), operating effectively at forward shocks of SNRs. According to theoretical considerations the first-order Fermi acceleration is efficient enough to account for the observed CR flux (e.g., Axford et al., 1977; Krymskii, 1977; Bell, 1978a, 1978b; Blandford & Ostriker, 1978; Drury & Voelk, 1981). The acceleration process leads to a formation of the power-law particle energy distribution with the spectral index $\alpha = 2$. After particles escape the shock region, their spectrum is modified during diffusive propagation through the interstellar medium. More energetic particles easily runaway from the Galaxy, which makes their spectra softer and the overall spectral index α increases by a value $\sim 0.5 - 0.6$ (Mueller et al., 1991). Thus the final spectral index of the CR spectrum at the Earth is predicted to be $\alpha \sim 2.7$, in agreement with observations.

The Larmor radius of a particle with energy 10^{15}eV in the galactic halo magnetic field of 10^{-6}G is of the order of the light year and the presence of turbulent magnetic fields makes the
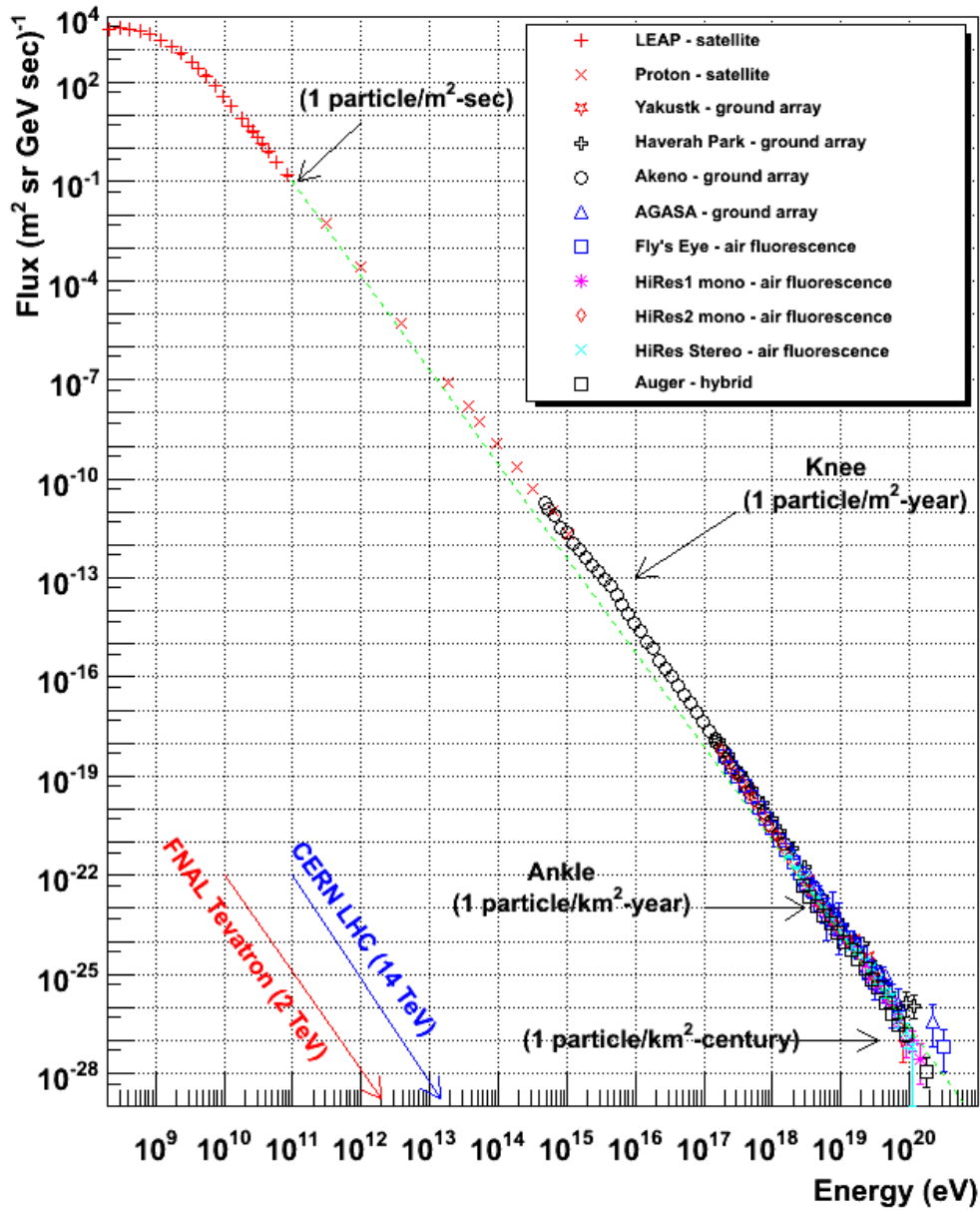
Figure 2.1: Differential all-particle spectrum of CRs above 10^8eV (Cronin et al., 1997). The spectrum combines measurements of several experiments: direct measurements from the LEAP (Seo et al., 1991) and Proton (Grigorov et al., 1971) experiments and extensive air showers measurements done by Yakutsk (Afanasiev et al., 1996), Haverah Park (Lawrence et al., 1991), Akeno AGASA (Nagano et al., 1992), Fly's Eye (Bird et al., 1994), HiRes (Abbasi et al., 2008) and Pierre Auger Observatory (Abraham et al., 2008). For comparison with experimental spectrum measurements, the theoretical spectrum with $\alpha = 3$ is drawn (green dashed line). Also the main spectral features, i.e. the "knee" at $\sim 3 \cdot 10^{15}$eV and the "ankle" at $\sim 3 \cdot 10^{18}$eV, are indicated. The CR flux at the Earth is also shown for different energies (figure copied from Hanlon (2008)).

galactic CR source identification difficult because of the diffusive character of CR propagation. Diffusing CRs thus quickly loose correlations with sources of origin. The CR anisotropy investigations show that spatial distribution of CRs with energies below 10^{15}eV is essentially isotropic with only small departures of the order of 10^{-3} or even 10^{-4} (Ahlers & Mertsch, 2017). This can serve as a proof of a diffusive character of the galactic CR transport.

Multiwavelength studies of supernova remnants give direct evidence of high-energy particle production at these sources. It was first proposed by Shklovskii (1953), that the observed nonthermal radio emission in SNRs has a synchrotron nature and is produced by relativistic electrons. Using typical value of the synchrotron spectral index $\alpha_{syn} \sim -0.5$ (Clark & Caswell, 1976; Green, 1984) measured in SNRs and the formula $\alpha_{syn} = (1 - \alpha)/2$ (e.g., Longair, 2011) one can derive the spectral index $\alpha \sim 2$ of the power-law energy distribution of electrons producing the observed emission. This is clearly in agreement with the DSA theory. The total SNR kinetic energy converted into cosmic rays inferred from X-ray observations of SNRs is of order of 10% (Morlino & Caprioli, 2011; Slane et al., 2014), in agreement with the energy considerations of the SNR paradigm. Recent observations of SNRs in high-energy gamma-rays by satellite and ground-based facilities give also convincing evidence for particle acceleration in shock regions to energies at least 10^{14}eV (Aharonian et al., 2007; Aleksić et al., 2015; Abdalla et al., 2016b; Archambault et al., 2017). Gamma rays can be emitted by high-energy electrons via inverse Compton scattering off the radiation fields and also by energetic protons interacting with the hadronic component of the interstellar medium to produce neutral pions, which in turn decay into gamma rays. The observed gamma-ray emission from SNRs can in most cases be explained by either leptonic or hadronic models (Ackermann et al., 2013; Berezhko et al., 2013; Abdalla et al., 2016a). However, the observed gamma ray spectral distributions of the SNR IC 443 and W44 can be successfully reproduced only using a hadronic scenario (Tavani et al., 2010; Fang et al., 2013). This provides direct evidence for CR acceleration at SNRs. Bright X-ray rims detected in all spatially resolved young supernova remnants (Vink, 2012), whose emission may be variable on short time scales (Uchiyama, Aharonian, Tanaka, Takahashi, & Maeda, 2007), strongly suggest that local magnetic fields in shock regions are substantially amplified, most probably due to nonresonant streaming instabilities excited by shock-accelerated CRs in the shock precursor (Bell, 2004, 2005; Niemiec, Pohl, Stroman, & Nishikawa, 2008; Riquelme & Spitkovsky, 2009; Stroman, Pohl, & Niemiec, 2009; Kobzar, Niemiec, Pohl, & Bohdan, 2017, again supporting hadron acceleration in SNRs.

The existence of the "knee" in the CR spectrum and particles with energies in the range between 10^{15}eV and 10^{17}eV can be at least partially explained by changes in chemical composition of CRs in this energy region. Most acceleration processes, including DSA, are rigidity-dependent. This means that if a proton can be accelerated to the maximum energy of $\varepsilon_{p,max} \sim 5 \cdot 10^{15}$eV, then a fully ionized iron nucleus could reach the energy of $\varepsilon_{Fe,max} = 26E_{p,max} \sim (1-2) \cdot 10^{17}$eV in the same process. The "knee" would thus naturally arise as a superposition of the cutoffs in the spectra of individual elements whose composition changes close to the "knee" (Hörandel, 2004; Blasi & Amato, 2012). Note, however, that such a scenario assumes an intrinsic cut-off in the proton spectrum at $\sim 10^{15}$eV, that needs to be explaned by CR acceleration theories. The existence of particles with energies beyond the maximum iron energy is also not accounted for. Several models assume different ratios between galactic and extragalactic components of CRs at the energy range $10^{17} - 10^{18}$eV, origin of whose is unknown (Wibig & Wolfendale, 2004; Berezinsky et al., 2006; Allard et al., 2007; Hooper et al., 2007). The continuation of the galactic CR spectrum up to 10^{18}eV can be supported by a modification of the SNR paradigm or the existence of other classes of CR sources (Hillas, 2005).

The contribution to the CR flux of other possible galactic sources such as PWNs, interactions with shock waves produced in accretion disks around supermassive black holes (Protheroe & Szabo, 1992), secondary acceleration in the interstellar medium, etc., is estimated to be negligible and in general these processes cannot reproduce the power-law spectrum of cosmic rays (Bhattacharjee, 2000). However, recent observations of gamma rays from the Galactic center (Sagittarius A*, see Abramowski et al. (2016)) suggest that the central supermassive black hole is the source of particles with energies up to 10^{15}eV. Although the current rate of particle acceleration at the supermassive black hole is not sufficient to provide a substantial contribution to galactic CRs (Genzel, Eisenhauer, & Gillessen, 2010), the probable recent activity of this source and outflows from the Galactic center, known as the Fermi bubbles (Su, Slatyer, & Finkbeiner, 2010), can indicate the occurrence of the active phases for the last $10^6 - 10^7$ years. Therefore, the central supermassive black hole can be considered as an alternative to the SNR paradigm as a source of galactic CRs.

2.3 Extragalactic cosmic rays

CRs at energies above 10^{18}eV, the UHECRs, are commonly assumed to be of extragalactic origin and their flux becomes dominant over galactic CR flux in this energy range. Particles with

so large energies cannot be confined by the galactic magnetic fields long enough to produce the observed isotropic flux. For the same reason, at energies in excess of 10^{18}eV the cut-off in the galactic CR component is expected to be observed, so that a transition zone at the energy of $\sim 10^{18}$eV (the "ankle") is formed in the CR spectrum (Axford, 1994).

Mechanisms of UHECR acceleration are still a mystery. There are mainly two basic classes of processes generally invoked for explanation of the particle acceleration up to ultra-high energies: so-called top-down and bottom-up models.

According to the top-down models, UHECRs can be created via processes of decay or annihilation of more energetic or supermassive primary particles. These processes discuss the emission of particles by topological defects such as magnetic monopoles (Aab et al., 2016), cosmic strings (Bhattacharjee, 2000), quantum chromodynamic (QCD) fragmentation (Fodor & Katz, 2001), or decay of super-heavy dark matter particles (Berezinsky et al., 1997; Aloisio, Matarrese, & Olinto, 2015). In general, these processes represent the class of still non well constrained and speculative exotic mechanisms.

Bottom-up models propose the acceleration from low to high energies by shock waves, turbulent structures or some so-called "one-shot" mechanism. Among the extragalactic objects that are powerful enough to accelerate particles to macroscopic energies are sources such as active galactic nuclei (AGN), jets of radio galaxies, gamma-ray bursts, and clusters of galaxies. If one supposes that a particle with charge Z is gradually accelerated when residing in a region with magnetic field strength B and characteristic size L, the maximum achievable energy can be estimated as:

$$\varepsilon_{max} \sim \beta \cdot Z \cdot B \cdot L \tag{2.1}$$

where $\beta = v/c$, v is the characteristic velocity of particle scattering centers, and c is the speed of light.

Figure 2.2, which is a redrawn version of the original plot of Hillas (Hillas, 1984), shows the capabilities of astrophysical objects with size L and magnetic field B to accelerate particles up to ultra high-energy level. Solid and dashed lines, respectively, indicate regions with physical conditions (magnetic field and acceleration region size) suitable to allow proton and iron nucleus acceleration up to 10^{20}eV. Objects that are placed below these lines cannot accelerate corresponding particles to the energy of 10^{20}eV. Lines are drawn for $\beta \sim 1$. For more reasonable plasma velocities (e.g., $v \sim 1000$ km/s), lines will lie even higher cutting off all galactic sources

8
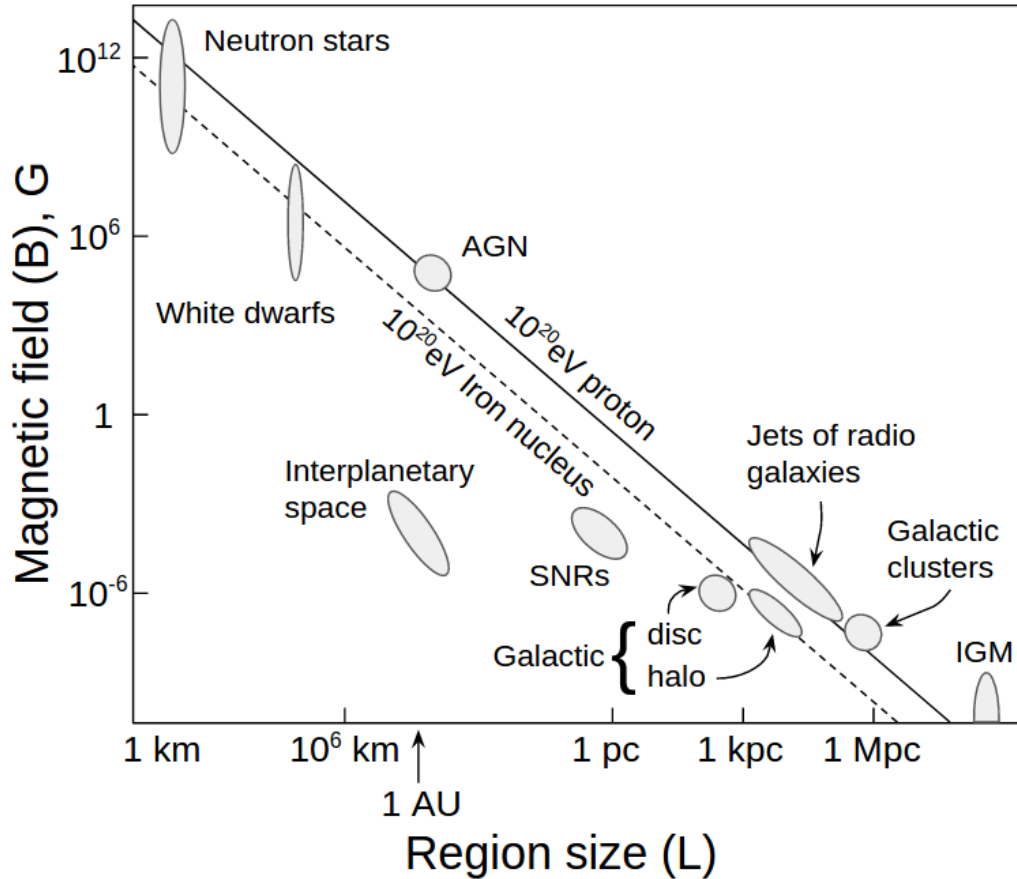
Figure 2.2: Redrawn version of the Hillas plot. Grey regions designate well known astrophysical objects, AU is the astronomical unit (see Hillas (1984)).

and leaving only extragalactic objects, such as AGN, jets of radio galaxies, galactic clusters and turbulence in the intergalactic medium (IGM). However, detailed processes allowing for UHECRs production in these sources are poorly known.

In the "one-shot" mechanism a direct acceleration of particles to high energy is realized through the large-scale induced electric field (Swann, 1933). This scenario can be applicable to objects such as pulsars, black holes (Neronov, Semikoz, & Tkachev, 2009), or jets of AGN (Schopper et al., 2002).

Particle interactions leading to the existence of the GZK-cutoff limit the travel distance of UHECR particles. As an example, a particle with energy 10^{22}eV at a source, after traveling a distance of about 100 Mpc has the energy of 10^{20}eV only (Cronin, 1992), because of the interaction with cosmic microwave background. This leads to the conclusion that particles with energies above 10^{20}eV must be produced in a nearby environment with radius of $10 - 100$ Mpc, depending on the initial energy of particles. Taking into account that UHECRs propagate

through the Galaxy without being significantly deflected by galactic magnetic fields, one could expect to identify their sources easily. However, observational data show largely isotropic UHECR flux, which is not correlated with the observed distribution of potential UHECRs sources (Aab et al., 2015). In addition, poor knowledge about the intergalactic magnetic fields combined with weakly constrained models of galactic magnetic fields lead often to completely different results about sources of UHECR origin (Farrar et al., 2015; Carpio & Gago, 2016). Thus, despite selecting candidate class objects capable of producing UHECRs, poor knowledge of specific acceleration mechanisms combined with weak constraints from observations still prohibit us from drawing definite conclusions on the origin of these particles.

CHAPTER 3
SHOCKS IN COLLISIONLESS PLASMAS

Shock waves are ubiquitous phenomena in the Universe and thereby represent a large section in astrophysical investigations. Great scientific interest in that topic is also supported by a number of interesting plasma processes provided by astrophysical shocks (which are in general impossible to reproduce in the laboratory conditions) and by role of shock waves in CR generation and acceleration processes. A subclass of shocks which are referred to as collisionless and in addition have parameters which are relevant for SNRs is discussed here. Such shocks are the most important ones for investigations of the origin of galactic CRs.

3.1 Collisionless plasma

In a simplified description the plasma consists of charged particles: ions and electrons. Under many astrophysical conditions the plasma is rarefied, particle collisions are rare, and collective particle interactions are dominant. Such plasma is referred to as the collisionless plasma.

To define the notion of a collisionless plasma from the physics point of view it is necessary to describe the main plasma parameters. In the electron-ion plasma the ion and the electron plasma frequencies are defined by the formulas:

$$\omega_{pi} = \sqrt{\frac{N_i\, e^2}{\varepsilon_0\, m_i}}\ , \tag{3.1}$$

$$\omega_{pe} = \sqrt{\frac{N_e\, e^2}{\varepsilon_0\, m_e}}\ , \tag{3.2}$$

where m_i and m_e are the ion and electron mass, N_i and N_e are the ion and electron number density, e is the electric charge, and ε_0 is electric permittivity of the vacuum. The plasma frequency is defined as $\omega_p = \sqrt{\omega_{pi}^2 + \omega_{pe}^2}$. Taking into account that $m_i \gg m_e$ and Equations 3.1 and 3.2, the plasma frequency can be treated as equal to the electron plasma frequency, $\omega_p \approx \omega_{pe}$. Characteristic plasma lengths related to these most basic plasma oscillation modes can be defined as follows:

$$\lambda_{si} = \frac{c}{\omega_{pi}}\ , \tag{3.3}$$

$$\lambda_{se} = \frac{c}{\omega_{pe}}\ , \tag{3.4}$$

11

where λ_{si} and λ_{se} are the ion and electron skin depths, respectively.

Screening or Debye length, λ_D, is the distance which characterizes the electric screening of the Coulomb potential of an individual particle in a plasma. It can be defined as:

$$\lambda_D = \sqrt{\frac{\varepsilon_0 k_B T_e}{N_e e^2}} \; , \qquad (3.5)$$

where k_B is the Boltzmann constant, and T_e is the plasma electron temperature. Using definition of a thermal velocity of electrons, $v_{th,e} = \sqrt{\frac{2k_B T_e}{m_e}}$, the Debye length can be rewritten as:

$$\lambda_D = \frac{v_{th,e}}{\sqrt{2}\omega_{pe}} \; . \qquad (3.6)$$

The number of particles contained within the volume defined by the Debye length, $N_D = N\lambda_D^3$, measures the number of particles that interact collectively in the plasma.

Plasma becomes collisionless when the rate of particle collisions due to Coulomb scattering is much smaller then the plasma frequency. The mean free path of electrons can be defined as $l = \lambda_D N_D$ (Klimontovich, 1997) and thus the collision rate is $v \propto v_{th,e}/l = v_{th,e}/(\lambda_D N_D)$. Using Equation 3.6 one can write:

$$\frac{v}{\omega_{pe}} \propto \frac{v_{th,e}\lambda_D}{\lambda_D N_D v_{th,e}} = \frac{1}{N_D}. \qquad (3.7)$$

The relation 3.7 goes to zero, $(v/\omega_{pe}) \to 0$, when $N_D \gg 1$. It means that for the absence of particle collisions and the dominance of collective interactions the number of particles in a Debye sphere should be large.

To characterize the degree of plasma collisionality, the so-called plasma parameter, g, can be used. It is defined as:

$$g = \frac{1}{N_D} \propto \frac{N_e^{1/2}}{T_e^{3/2}} \; . \qquad (3.8)$$

The collisionless limit, $g \to 0$, is achieved when $N_D \gg 1$. One can see from the formula 3.8 that this limit is achieved for rarefied and hot plasmas.

Under collisionless plasma conditions the kinetic particle energy must be greater than the potential energy of interactions. Noting that the mean kinetic energy $\langle E_{kin} \rangle \propto T_e$ and the mean potential energy $\langle E_{pot} \rangle \propto \langle r \rangle^{-1} \propto N_e^{1/3}$, where $\langle r \rangle$ is the mean distance between plasma particles, the formula 3.8 can be rewritten as:
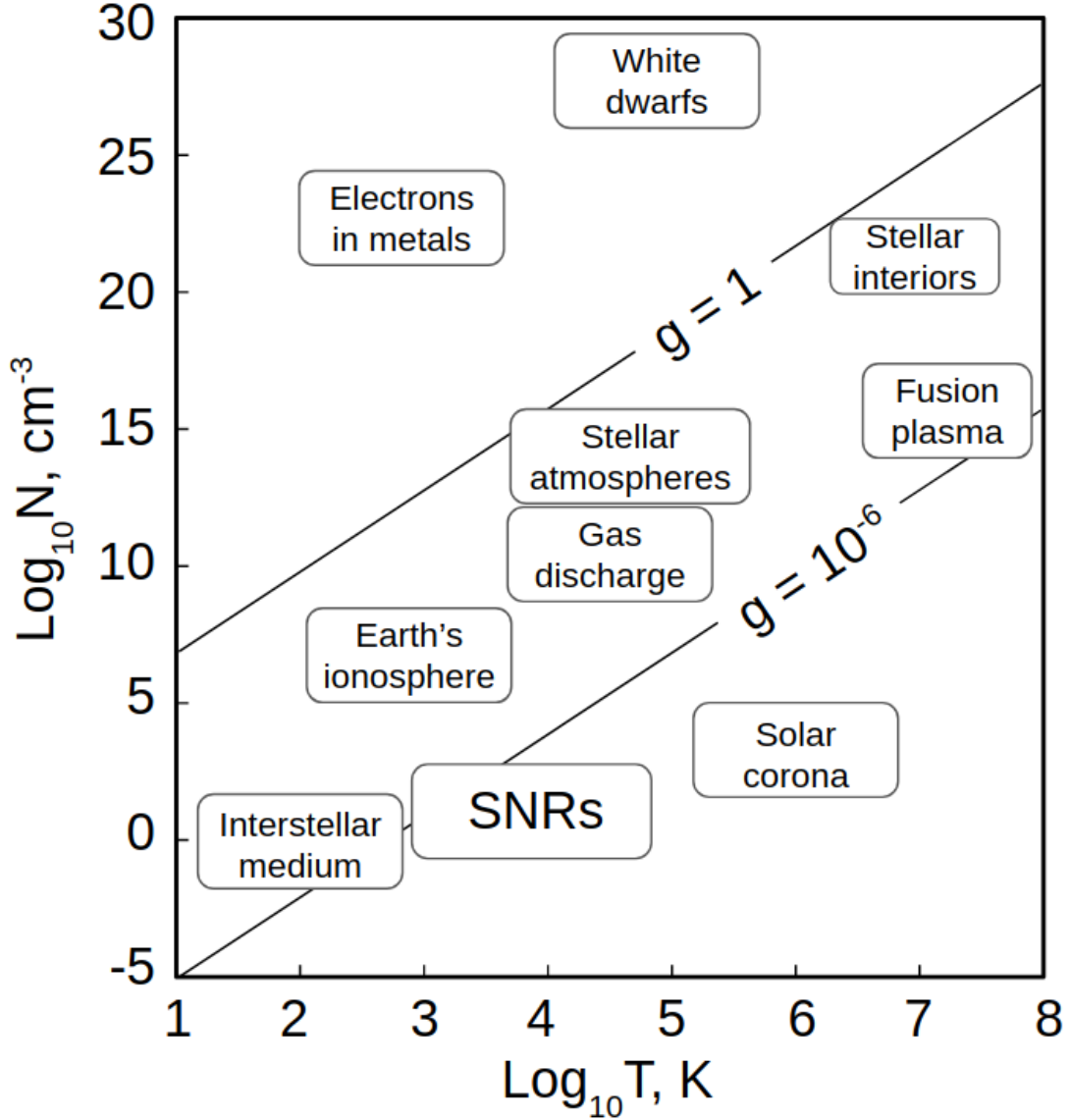
Figure 3.1: Temperature and density range of physical and astrophysical objects. Solid lines indicate conditions for plasma parameter of $g = 1$ and $g = 10^{-6}$.

$$\frac{\langle E_{kin} \rangle}{\langle E_{pot} \rangle} \propto \frac{T_e}{N_e^{1/3}} \propto g^{-2/3} \ . \tag{3.9}$$

This leads to a correct relation between the kinetic and the potential particle energy, $E_{kin} \gg E_{pot}$, in the collisionless limit, in which $g \ll 1$.

Figure 3.1 estimates the plasma parameter for a selected physical systems with corresponding densities and temperatures. All astrophysical plasma systems, except white dwarfs, represent collisionless plasma environments with a wide range of plasma parameter from 10^{-9} in solar corona up to almost one in stellar interiors. SNRs have typical temperatures of about a few to ten thousand Kelvins and densities of the order of $(10 - 100)\text{cm}^{-3}$. Thus the plasma parameter

in SNRs is less then 10^{-6}. This validates the collisionless plasma treatments of shock waves hosted in SNRs.

3.2 MHD description of shock waves

Wave propagation in plasmas can be described by ideal fluid equations (Landau & Lifshitz, 1959), but in conditions of large wave amplitudes the wave steepening leads to shocks. A shock wave can be defined as a narrow transition region which moves in a medium with a supersonic velocity. The shock propagation is accompanied by the entropy growth that implies the energy dissipation. The ideal fluid description breaks down in this very thin plasma layer, a so-called shock transition layer, the thickness of which is defined by the nature of dissipation processes.

The shock separates plasma regions with different densities, pressures, temperatures, and electro-magnetic field amplitudes and structures. It is convenient to consider the shock physics in the shock reference frame, which moves with the shock velocity v_{sh} and in which the shock wave is stationary. Figure 3.2 shows the shock in the shock rest frame. In the following the index "1" refers to upstream and the index "2" to downstream plasma quantities. In the shock reference frame, the undisturbed plasma inflows towards the shock discontinuity with supersonic velocity $u_1 = v_{sh}$ and outflows with subsonic velocity u_2 away from the discontinuity.

Conservation laws of mass, momentum, and energy across the shock in unmagnetized plasma require that:

$$
\begin{aligned}
&\frac{\partial}{\partial x}(\rho u) = 0 \, , \\
&\frac{\partial}{\partial x}(\rho u^2 + P) = 0 \, , \\
&\frac{\partial}{\partial x}\left(\frac{1}{2}\rho u^3 + \frac{\Gamma_p}{\Gamma_p - 1} u P\right) = 0 \, ,
\end{aligned}
\tag{3.10}
$$

where Γ_p is the adiabatic index, P is the plasma pressure, ρ is the plasma density, and u is the velocity of the plasma in the reference frame of the shock. These conservation equations have non-trivial solution, known as the Rankine–Hugoniot relations:
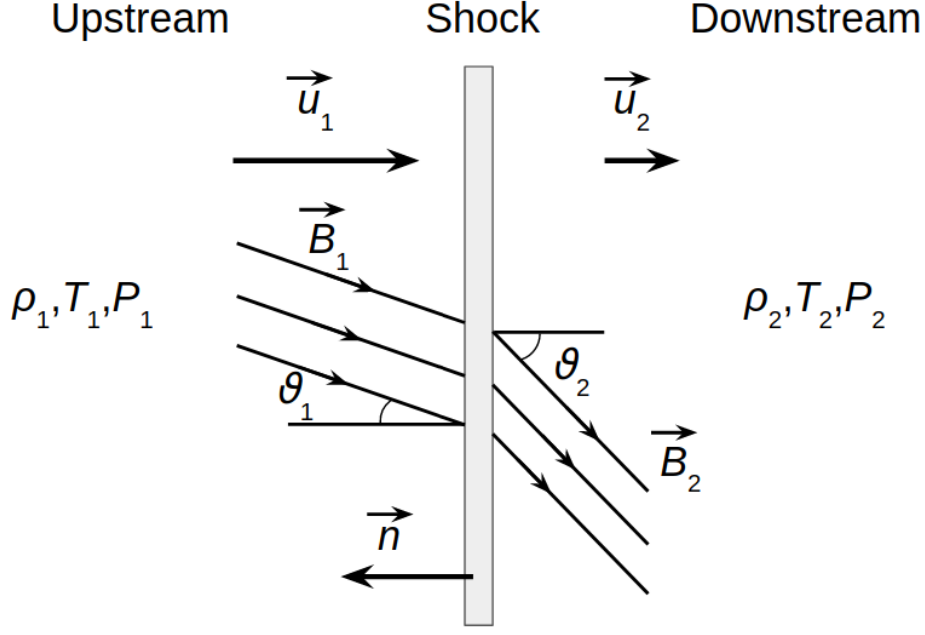
Figure 3.2: Schematic illustration of the shock region in the shock rest frame.

$$\frac{\rho_2}{\rho_1} = \frac{u_1}{u_2} = \frac{(\Gamma_p + 1)M_s^2}{(\Gamma_p - 1)M_s^2 + 2} \, ,$$

$$\frac{P_2}{P_1} = \frac{2\Gamma_p M_s^2}{\Gamma_p + 1} - \frac{\Gamma_p - 1}{\Gamma_p + 1} \, ,$$

$$\frac{T_2}{T_1} = \frac{(2\Gamma_p M_s^2 - (\Gamma_p - 1))((\Gamma_p - 1)M_s^2 + 2)}{(\Gamma_p + 1)^2 M_s^2} \, ,$$

(3.11)

where T_1 and T_2 are temperatures of upstream and downstream plasma, respectively, and M_s is the sonic Mach number of the shock defined by the formula:

$$M_s = \frac{v_{sh}}{c_s} \, ,$$

(3.12)

where $c_s = \sqrt{\frac{\Gamma_i k T_i}{m_i}}$ is the ion sound velocity in the plasma.

In the presence of a weak and dynamically insignificant magnetic field, the jump conditions for hydrodynamical plasma parameters remain unmodified. From Maxwell's equations one can derive condition of the continuity of the normal component of magnetic field. Tangential components in the downstream region become amplified on a factor ρ_2/ρ_1, because of the conditions of frozen-in magnetic fields in the compressed plasma behind the shock. Thus, if

15

the large-scale magnetic field in the upstream region forms an angle θ_1 with respect to the shock normal $\vec{n}$ (Fig. 3.2), then downstream of the shock the field is inclined at the angle $\theta_2 = \arctan(\rho_2/\rho_1 \cdot \tan\theta_1)$. In the following, we use θ to designate the upstream field orientation, $\theta = \theta_1$.

Shocks can be simply classified in terms of the magnetic field orientation. Strictly parallel and perpendicular shocks have angles $\theta = 0^o$ and $\theta = 90^o$, respectively. For intermediate shock obliquities, quasi-parallel ($\theta = 0^o - 45^o$) and quasi-perpendicular ($\theta = 45^o - 90^o$) designations are used. The shocks with angles $\theta \neq 0^o$ and $\theta \neq 90^o$ are also referred to as oblique (Treumann, 2009). The physics of shocks depends on the magnetic field orientation. In the parallel shock case, charged particles can easily escape from the shock region along upstream magnetic field lines. The shock thickness in this case is about $100\lambda_{gi}$, where λ_{gi} is typical thermal ion gyroradius. At perpendicular shocks, particles crossing the shock towards upstream are bent by the magnetic field and remain confined to a narrow region with the size of the order of λ_{gi}.

Present observational data do not to give clear constrains on the large-scale magnetic field configuration in SNR shocks. Different approaches at data modeling suggest either the presence of quasi-perpendicular (Petruk et al., 2009; Schneiter et al., 2010; West et al., 2016) or quasi-parallel (Rothenflug et al., 2004; Bocchino et al., 2011; Schneiter et al., 2015) fields even for the same SNRs. In this thesis perpendicular shocks ($\theta = 90^o$) are examined as the most simple form of the quasi-perpendicular case.

The shock velocity in the magnetized plasma can be described in terms of the Alfvén Mach number:

$$M_A = \frac{v_{sh}}{v_A} \, , \tag{3.13}$$

where $v_A = \sqrt{\frac{B_1^2}{\mu_0(N_e m_e + N_i m_i)}}$ is the Alfvén wave velocity, B_1 is the strength of the large-scale upstream magnetic field, N_i is the ion number density and μ_0 is magnetic permeability of the vacuum. In the following, the term Mach number is used to refer to the Alfvén Mach number, unless specified otherwise.

In the presence of the magnetic field, the plasma beta, β_p, is used to describe the ratio of the plasma pressure, $P_p = (N_e k_B T_e + N_i k_B T_i)$, to the magnetic pressure, $P_m = B_1^2/(2\mu_0)$. The plasma beta thus reads:

$$\beta_p = \frac{P_p}{P_m} = \frac{N_e k_B T_e + N_i k_B T_i}{B_1^2/(2\mu_0)} = \beta_e + \beta_i \; , \tag{3.14}$$

where $\beta_e = \frac{N_e k_B T_e}{B_1^2/(2\mu_0)}$ is the electron plasma beta and $\beta_i = \frac{N_i k_B T_i}{B_1^2/(2\mu_0)}$ is the ion plasma beta.

Magnetic field in a plasma introduces also additional temporal and spatial scales, namely, the ion and electron gyrofrequencies, Ω_i and Ω_e, respectively, and gyroradii, λ_{gi}, λ_{ge}. The gyrofrequencies are defined as:

$$\Omega_i = \frac{eB_1}{m_i} \; , \tag{3.15}$$

and

$$\Omega_e = \frac{eB_1}{m_e} \; . \tag{3.16}$$

The definition of gyroradii is:

$$\lambda_{gi} = \frac{v_\perp}{\Omega_i} \; , \tag{3.17}$$

and

$$\lambda_{ge} = \frac{v_\perp}{\Omega_e} \; , \tag{3.18}$$

where $v_\perp$ is the particle velocity perpendicular to the magnetic field direction.

The relation of the electron and ion gyrofrequencies to the respective plasma frequencies, Ω_e/ω_{pe}, Ω_i/ω_{pi}, is another measure of the level of plasma magnetization. They can be also expressed in terms of the Alfvén velocity:

$$\frac{\Omega_e}{\omega_{pe}} = \frac{v_A}{c} \sqrt{\frac{m_i}{m_e}} \; , \tag{3.19}$$

and

$$\frac{\Omega_i}{\omega_{pi}} = \frac{v_A}{c} \; . \tag{3.20}$$

3.3 Nonrelativistic perpendicular shocks

An average initial expansion velocity of a young supernova ejecta is about $v_{sh} \approx 10\ 000$ km/s (Wang et al., 2009). As $v_{sh} \ll c$, these shocks are nonrelativistic. Furthermore, using averaged values of the interstellar density (~ 1 particle/cm^3), the galactic magnetic field strength ($1 - 10\mu$G) and the interstellar medium temperature ($\sim 0.1 - 1$ eV) the range of the Alfvén

Mach number of SNR shocks can be estimated as $M_A \sim 50 - 500$, sonic Mach number as $M_s \sim 20 - 200$, and plasma beta $\beta_p \sim 1$. SNR shocks thus always host high Mach number shocks. Such shocks are subject to investigation in this thesis.

For a plasma with adiabatic index $\Gamma_p = 5/3$, and for strong shocks with $M_s \gg 1$ the Rankine–Hugoniot conditions (Eq. 3.11) simplify to:

$$
\begin{aligned}
\frac{\rho_2}{\rho_1} &= \frac{u_1}{u_2} = 4 \,, \\
\frac{P_2}{P_1} &= \frac{5}{4}M_s^2 \,, \\
\frac{T_2}{T_1} &= \frac{5}{16}M_s^2 \,.
\end{aligned}
\tag{3.21}
$$

This shows that at high sonic Mach number shocks, the compression factor does not depend on the shock properties (velocity, medium density, temperature, etc.). It has an important consequence for the spectral index of CRs produced at strong shocks (see Sec. 4.1).

Additional physically motivated classification of shocks into subcritical and supercritical ones is defined by the critical value M_c of the sonic Mach number. Thus a shock is subcritical for $M_s \lesssim M_c$ and supercritical for $M_s \gtrsim M_c$. The shock criticality refers to the capability of a shock wave to support its shock character only via resistive (Joule) dissipation. Subcritical shocks are capable of generating sufficient dissipation to account for the required slow down of the flow, thermalization, and entropy increase. The relevant processes are based on wave–particle interactions between the shocked plasma population and the shock-excited turbulent wave fields (Treumann, 2009). However, above the critical Mach number, M_c, these processes are not efficient to sustain the shock and the only efficient way of the dissipation of the excess energy is the reflection of a substantial part of the inflowing plasma back upstream. A fraction of the incoming ions is thus reflected by a potential barrier and the magnetic ramp at the shock front. The critical value of sonic Mach number depends on the plasma temperature (plasma beta) and magnetic field orientation. Nevertheless, for the whole parameter range there is maximum critical value $M_c \approx 2.76$ (Marshall, 1955). Typical Mach number values for supernova remnants are always above this limit, therefore only supercritical shocks are considered here.

Theoretical studies of perpendicular shocks (Leroy et al., 1981, 1982; Leroy, 1983) demonstrate a great importance of the reflected ions in the structure of such shocks. Schematic structure of a perpendicular nonrelativistic high Mach number shock is presented in Figure 3.3. The shock transition consists of an upstream, a foot, a ramp, an overshoot-undershoot structures,
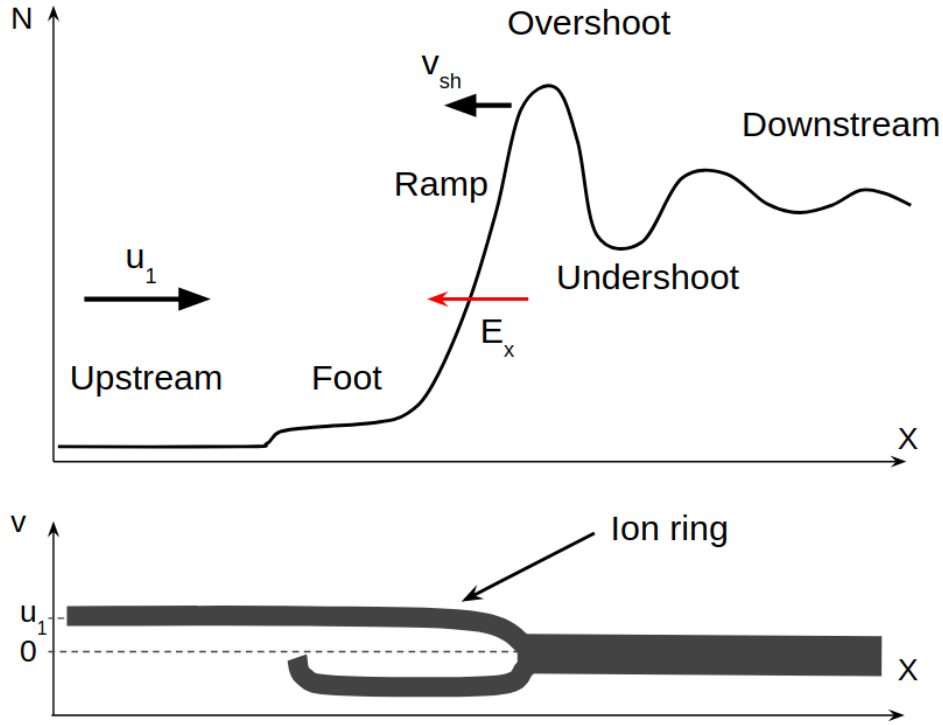
Figure 3.3: Sketch of the perpendicular shock structure in the downstream reference frame. Top panel: particle density profile, bottom panel: phase space distribution of x-component of the ion velocity. E_x is the charge separation electric field in the shock ramp. v_{sh} is the shock velocity. The upstream magnetic field, $\vec{B}_1$ (not designated in the figure), is perpendicular to the shock normal or v_{sh}.

and the downstream region. The upstream and downstream regions contain, respectively, undisturbed and already shocked plasma. The ramp region is characterized by an abrupt jump of electrostatic potential and contains a charge-separation electric field, E_x, as a result of heating and compression of electrons. This field in the supercritical shock is strong enough to reflect ions. However, ion reflection is not specular. The shock has a finite width, and any particle that arrives at the shock from upstream penetrates to a different depth into the shock. Once a particle reaches the shock it can either be reflected from some point within the shock transition or become transmitted downstream. Thus populations of reflected ions and ions transmitted downstream are formed. The presence of the charge-separation electric field, which is perpendicular to the magnetic field, implies that the magnetized electrons experience an electric drift along the shock. Magnetic field of the electron-drift current causes an overshoot in the magnetic field in the shock ramp. Shock-reflected ions in a quasi-perpendicular shock cannot escape far upstream. Their penetration into the upstream plasma is severely restricted by perpendicular component of the magnetic field. Within this distance the ions perform a

gyrational orbit before returning to the shock. Since the reflected ions move with respect to the inflowing plasma with relative velocity of $\vec{v}_{rel}$, they are sensitive to the inductive convection electric field $\vec{E}_y = \vec{v}_{rel} \times \vec{B}$, which is along the shock surface both perpendicular to the flow and to the large-scale magnetic field. The magnetic field of the current carried by the accelerated ions causes the magnetic foot in front of the shock ramp. Reflected ions perform only a single gyration, which corresponds to a ring in the velocity space (Fig. 3.3), and gain enough energy to penetrate the downstream region at later time. The signature of this ion ring may persist downstream of the shock front and be the origin of an overshoot-undershoot pattern just behind the ramp. These structures become more dilute farther downstream.

Reflected ions interact with the incoming plasma and produce a number of instabilities in the shock foot. For our further discussion of electron pre-acceleration at high Mach number shocks two of these instabilities are of greatest importance – the Buneman instability in the shock foot and the Weibel filamentation instability in the shock ramp.

The Buneman instability is electrostatic type of a two-stream or current-driven instability, named after Oscar Buneman, who developed the theoretical basis of this process and predicted the existence of the electron heating caused by current dissipation (O. Buneman, 1958, 1959). The Buneman instability in the shock foot results from the interaction of the shock-reflected ions with the incoming upstream electrons. The properties of electrostatic modes that result from this instability depend on physical parameters such as the shock Mach number and the upstream plasma temperature.

The necessary condition for the instability, known as the unstable condition, is that the thermal velocity of the electrons is smaller than the relative speed between incoming electrons and reflected ions, $\Delta v / v_{th,e} > 1$, where Δv is the stream velocity deference between incoming electrons and reflected ions. The zero net electric current condition in the foot region can be defined as:

$$N_0 v_i + N_r v_r - N_e v_e = 0 , \tag{3.22}$$

where $N_0 = N_{0i} = N_{0e}$ is the upstream number density, N_r is the number density of the reflected ions, N_e is the total number density of electrons, v_i is the velocity of incoming ions with a value of $v_i \simeq u_1$, $v_r \approx -u_1$ is the reflected ion speed, and v_e is the incoming electron speed. Note that the electron density in the shock foot needs to be adjusted to $N_e = N_0 + N_r$ to ensure charge neutrality. Thus v_e is:

$$v_e = \frac{1-\chi}{1+\chi} u_1 \,, \tag{3.23}$$

where $\chi = N_r/N_0$ is the density ratio of the reflected and incoming ions, which is typically of order ~ 0.2 (Leroy, 1983; Papadopoulos, 1988). Using $\Delta v = v_e - v_r$ and Equation 3.13, the unstable condition reads (Matsumoto et al., 2012):

$$M_A \gtrsim \frac{1+\chi}{2} \sqrt{\beta_e} \left(\frac{m_{\mathrm{i}}}{m_{\mathrm{e}}} \right)^{\frac{1}{2}}. \tag{3.24}$$

For the sonic Mach number, this unstable condition can be rewritten as (Wieland et al., 2016):

$$M_s \gtrsim \frac{1+\chi}{2} \sqrt{\frac{m_i}{m_e}} \sqrt{\frac{T_e}{T_i}}, \tag{3.25}$$

The condition of Equation 3.24 (or Eq. 3.25) should be satisfied in order for the electrostatic Buneman instability to be excited in the system. For SNR environments, $T_e \approx T_i$, $\beta_e \sim 0.5$, and conditions 3.24 and 3.25 give $M_A \gtrsim 26$ and $M_s \gtrsim 18$, respectively. The Buneman instability is therefore expected to play a role in young SNRs that hosts high-Mach number shocks.

The linear dispersion relation of electrostatic Buneman waves is given by:

$$1 - \frac{\omega_{pe}^2}{2k^2 v_{th,e}^2} Z'(\zeta_e) - \frac{\omega_{pi}^2}{2k^2 v_{th,i}^2} Z'(\zeta_i) = 0 \tag{3.26}$$

where $Z(\zeta) = \pi^{(-1/2)} \int_{-\infty}^{\infty} \frac{e^{-z^2}}{z-\zeta} dz$ is the plasma dispersion function (Fried & Conte, 1961), $\zeta_e = \omega/(\sqrt{2}kv_{th,e})$ and $\zeta_i = (\omega - \vec{k} \cdot \Delta\vec{v})/(\sqrt{2}kv_{th,i})$. The maximum growth rate for the Buneman instability in the limit $\Delta v \gg v_{th,e} \gg v_{th,i}$ occurs near wave numbers (Tidman & Krall, 1971):

$$\frac{\vec{k} \cdot \Delta\vec{v}}{\omega_{pe}} \simeq 1, \tag{3.27}$$

where $\vec{k}$ is the wave vector of the electrostatic mode. One can see that the wave vector with the maximum growth rate is parallel to the stream velocity difference. Note that Equation 3.27 defines the value of the parallel component. The analysis of the dispersion relation (Eq. 3.26) shows that oblique modes with the parallel component defined by Equation 3.27 and some perpendicular component can grow with a similar rate (Amano & Hoshino, 2009b). For example, in case of $|\Delta v|/v_{th,e} = 10$, the growth rate of the oblique Buneman mode $\vec{k} = (k_{\parallel}, k_{\perp}) = (1,3)\omega_{pe}/\Delta\vec{v}$ is only twice smaller then the growth rate of the pure parallel mode with $k = k_{\parallel}$

(Amano & Hoshino, 2009b).

The second instability driven by the counterstreaming plasma beams is called Weibel-type filamentation instability. In its original formulation, the Weibel instability is excited by the temperature anisotropy (Weibel, 1959), but Fried (1959) has shown that situation of two counterstreaming plasma flows also leads to the Weibel instability growth. The condition relevant for the Weibel instability excitation at SNR shocks is that of two opposite ion streams over a bath of hot electrons (Kato & Takabe, 2008; Shaisultanov, Lyubarsky, & Eichler, 2012). Electrons can be heated by the reflected flow of ions in the ramp region or by the Buneman instability in the shock foot. The wave vector of the Weibel filamentation instability is perpendicular to the stream velocity. The maximum growth rate and the wavenumber can be described by the unmagnetized approximation for the beam-Weibel instability (Kato & Takabe, 2010a, 2010b):

$$\omega^2 - (kc)^2 + \sum_s \omega_{ps}^2[\alpha_s + 2(v_s/v_{th,s})^2(1 + \alpha_s)] = 0, \tag{3.28}$$

where $\alpha_s = \eta_s Z(\eta_s)$, $\eta_s = \frac{\omega}{kv_{th,s}}$, and index s refers to the four particle species: incoming ions and electrons, and reflected ions and electrons. The growth rate for the case of $T_e \gg T_i$ has a broad maximum around $k \sim (0.1-0.5)\omega_{pe}c^{-1}$, and the exact value depends on ion and electron temperatures, flow velocity, ion-to-electron mass ratio, etc. (see, e.g, Tidman & Krall, 1971; Kato & Takabe, 2008, 2010b). The wavelength of the most unstable mode is comparable to the ion skin depth, λ_{si}, and, e.g., for ion-to-electron mass ratio $m_i/m_e \sim 100$ it is $\lambda_{Weibel} \sim (0.4-2)\pi\lambda_{si}$. The wave vectors of the Weibel instability modes are perpendicular to the streaming velocity.

The importance of the electrostatic Buneman and the two-stream Weibel instabilities for particle energization processes is discussed in Section 4.3.

3.4 Shock self-reformation and rippling

As discussed in Section 3.3, supercritical quasi-perpendicular shocks dissipate kinetic particle energy by the ion reflection from the shock. However, it has been demonstrated that ion reflection at supercritical shocks is not stationary. Under certain conditions, the flux of reflected particles changes in a quasi-periodic way and the shock cyclically self-reforms. In this process the shock is not destroyed and shock structures evolve cyclically.

Early 1D hybrid-kinetic simulations (Quest, 1985; B. Lembege & Dawson, 1987; Cargill &

Papadopoulos, 1988) and recent fully kinetic 2D simulations (Umeda et al., 2008, 2009; Umeda et al., 2014; Wieland et al., 2016) have demonstrated the evidence that supercritical low-Mach and high-Mach number perpendicular shocks may undergo cyclic self-reformation. The shock reformation arises because ion reflection from the shock ramp is not a continuous process. However, the physics of ion-reflection's non-stationarity is different for shocks with different Mach numbers. As frequently observed in low-Mach-number shocks, reflected ions bunch in the upstream edge of the shock foot due to either a non-steady reflection rate or steepening of plasma waves excited in this region (Umeda et al., 2008, 2009; Umeda et al., 2014). The cross-shock potential builds at this location and a new shock front develops. However, shock self-reformation can be suppressed by oblique whistler waves in low Mach number shocks with somewhat stronger magnetic field strengths (Hellinger et al., 2007). In high-Mach-number shocks (Wieland et al., 2016), non-stationary ion reflection is also observed. The physics of reflected-ion bunching is governed in this case by the dynamics of current filaments resulting from the Weibel-like instability that mediates the shock transition. Time-dependent flow of reflected ions imposes a significant impact on the structure of the shock ramp and foot, varying the upstream extension of Weibel filaments and the conditions for Buneman-wave growth.

Under some conditions the shock front can also develop a rippled structure. Shock rippling is known from 2D and 3D plasma simulation studies of supercritical quasi-perpendicular shocks with low Mach numbers (Winske & Quest, 1988; Lowe & Burgess, 2003; Burgess & Scholer, 2007; Umeda et al., 2008, 2009; Umeda et al., 2014). In this regime the ion temperature anisotropy arising from ion reflection at the shock can drive the Alfvén ion cyclotron or the mirror instability in the shock ramp, and the resulting unstable modes have wavelengths of a few ion skin depth, $\sim \lambda_i$. The waves propagate along the regular large-scale magnetic field. They can significantly contribute to ion isotropization and thermalization at the shock and downstream. Studies of such wave structures with 2D simulations require an in-plane configuration of the magnetic field. Simulations with out-of-plane field configurations suppress the parallel-propagating waves. However, in this setup another shock-front instability can occur that produces fluctuations on a spatial scale commensurate with the gyroradius of shock-reflected ions (Burgess & Scholer, 2007). These fluctuations propagate along the shock surface with the speed and direction of ions gyrating in the shock foot. The instability requires sufficiently high Mach numbers. Shock simulations in this regime demonstrate the shock rippling phenomenon with modulation length along the shock of $\sim 20\lambda_i$ or one ion gyroradius (Wieland et al., 2016).

As a consequence of the rippled structure, the reflection rate of the ions can be enhanced at some locations along the shock front. These regions then provide stronger Buneman instability which should lead to more efficient localized electron heating and acceleration.

CHAPTER 4
PARTICLE ACCELERATION AT SHOCKS

4.1 Diffusive shock acceleration

In 1949 Enrico Fermi (Fermi, 1949) proposed a new CR acceleration mechanism. A charged particle traveling through the interstellar space interacts stochastically with interstellar magnetic clouds which leads to the energy transfer from the clouds to CRs. When a particle and a cloud have oppositely directed velocities, the particle gains the energy (head-on collision). On the other hand, if a particle and a cloud move in the same direction, the particle looses its energy (tail-on collision). The energy gains/losses linearly depend on the velocity difference between the particle and the cloud. It would thus seem that for a chaotic cloud velocity distribution the average energy increment should be zero. However, Fermi argued that even in such a case particle encounters with approaching clouds dominate over encounters with receding clouds, because the number of collisions in each case is proportional to $c + u$ and $c - u$, respectively, for a relativistic particle moving with velocity approaching the speed of light and for an average cloud velocity u. The energy increment can thus be derived as:

$$\frac{\Delta \varepsilon}{\varepsilon} = \sum_i \left(\frac{u_i}{c} \right)^2 = kA \tag{4.1}$$

where A is the average energy change per collision, k is the number of collisions or magnetic clouds, and u_i is the velocity of a cloud with index "i".

To derive the spectrum of CRs two simplifying assumptions are made. Firstly, CRs have a finite lifetime in the interstellar medium and their number decreases exponentially with time because of the escape from the Galaxy. Secondly, particles are injected continuously with a certain relativistic energy to provide a constant cosmic ray flux. The resulting energy distribution is thus described with the power-law dependence (Kulsrud, 2005):

$$N(\varepsilon) \propto \varepsilon^{-(1 + \tau_{en}/(A\tau_{CR}))}, \tag{4.2}$$

where τ_{en} is the mean time between encounters and τ_{CR} is the mean CR lifetime. Observed CR spectra assume the power-law with spectral index $\alpha \sim 2$. Consequently, the ratio $\tau_{en}/(A\tau_{CR})$ should be of order of unity. For the interstellar clouds the average energy change per collision is very small, $A = 10^{-8}$, and for CR lifetime of $\tau_{CR} \sim 10^8$ years (Fermi, 1949) the required collision rate is $\tau_{en} \sim 1$, which is too small in comparison with the value inferred from
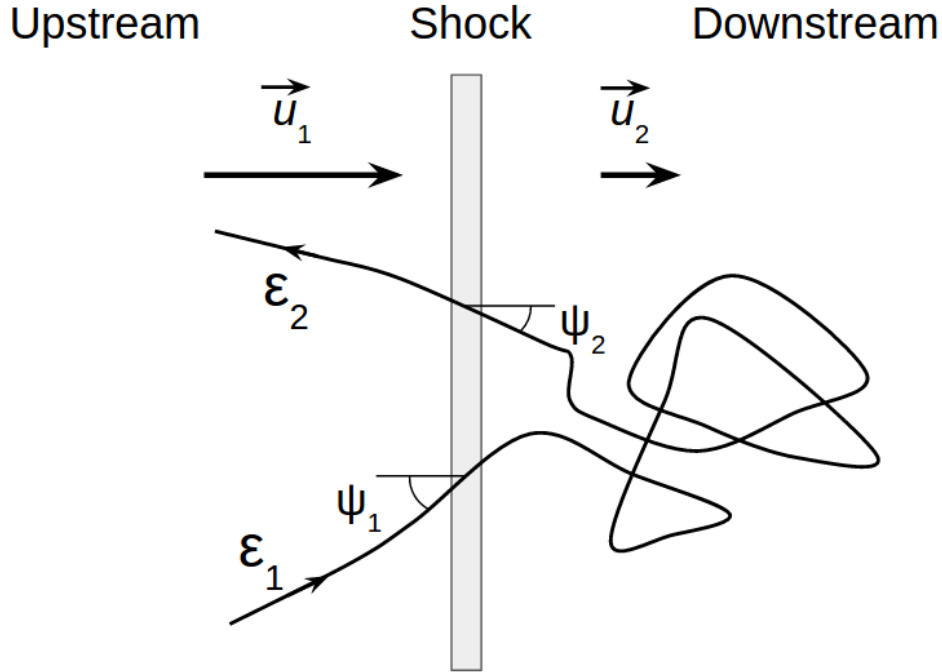
Figure 4.1: Schematic trajectory of a particle accelerated via DSA. The shock reference frame is used.

observations. It means that the Fermi process in its original form (nowadays referred to as the second-order Fermi process) cannot account for observations. Nevertheless Fermi's idea was a step in the right direction.

Next it was proposed that particles can be accelerated by shock waves (e.g., Axford et al., 1977; Krymskii, 1977; Bell, 1978a, 1978b; Blandford & Ostriker, 1978; Drury & Voelk, 1981). As mentioned in Chapter 2, supernova remnants seem to be the only class of sources able to form appropriate shock conditions and produce an enormous amount of energy to support the observed CR flux. The acceleration process at a shock is illustrated schematically in Figure 4.1. The model involves a strong shock propagating through a diffuse medium. A particle with energy ε_1 crosses the shock front at the angle ψ_1 and is unaffected because the process involves relativistic particles that see the shock as an infinitely thin contact discontinuity. Then the particle is scattered in the downstream plasma and may be reflected back towards the shock. Upon crossing the shock from downstream at angle ψ_2, the particle energy changes, $\varepsilon_1 \neq \varepsilon_2$, and at each crossing a particle may gain or loose some fraction of its energy. Particle scattering process has a diffusive nature and results from interactions of cosmic rays with electromagnetic Alfvén waves (Blandford & Eichler, 1987). At nonrelativistic shocks particle scattering provides isotropic velocity distributions in the upstream and downstream regions of

the shock. CR diffusion at the shock also defines particle escape and acceleration rates that determine desired power-law spectrum.

In the reference frame of a strong shock, upstream plasma velocity is $u_1 = v_{sh}$ and downstream velocity equals $u_2 = v_{sh}/4$ (according to the Rankine-Hugoniot conditions for high Mach number shocks, Eq. 3.21). In the reference frame in which the upstream plasma is at rest the downstream plasma moves toward the upstream plasma with a velocity of $u_2 - u_1 = -(3/4)v_{sh}$. Therefore, a particle diffusing in the upstream and crossing the shock experiences a head-on collision with the downstream plasma. An identical argumentation is valid for particle scattered in the downstream. Thus whenever the isotropized particles cross the shock they undergo head-on collisions with plasma and gain energies.

Let us define quantities A' and $\mathscr{P}$ as: $\varepsilon = A'\varepsilon_{in}$ is the average energy of a particle after one collision and $A' = 1 + A$ (see Eq. 4.1), ε_{in} is the initial particle energy, and $\mathscr{P}$ is the probability that this particle remains within the acceleration region after one collision. Then, after k collisions, there are $N = N_{in}\mathscr{P}^k$ particles with energies $\varepsilon = \varepsilon_{in}A'^k$, where N_{in} is the initial number of particles with energy ε_{in}. Removing k from these equations, one has:

$$\frac{\ln(N/N_{in})}{\ln(\varepsilon/\varepsilon_{in})} = \frac{\ln\mathscr{P}}{\ln A'} \ , \tag{4.3}$$

and hence

$$\frac{N}{N_{in}} = \left(\frac{\varepsilon}{\varepsilon_{in}}\right)^{\ln\mathscr{P}/\ln A'} . \tag{4.4}$$

In fact, Equation 4.4 determines $N = N(\geq \varepsilon)$, since it is the number of particles which have reached the energy ε and some fraction of them continue to be accelerated to higher energies. Thus the differential particle spectrum is:

$$N(\varepsilon) \propto \varepsilon^{-1+\ln\mathscr{P}/\ln A'}. \tag{4.5}$$

By simple arguments both A' and $\mathscr{P}$ can be determined quantitatively for a complete acceleration cycle (see, e.g., Longair, 2011). We consider relativistic particle, $v_p \sim c$, which cross the shock from upstream to downstream and its trajectory makes angle ψ with the shock normal. The plasma on the downstream side approaches the particle at a velocity $v' = (3/4)v_{sh}$ and so, performing a Lorentz transformation, the increment of the particle energy can be estimated as:

$$\frac{\Delta\varepsilon}{\varepsilon} = \frac{v'}{c}\cos\psi. \tag{4.6}$$

The probability that particles that cross the shock arrive at the shock within the angles ψ to $\psi + d\psi$ is proportional to $\sin\psi d\psi$, and the rate at which they approach the shock front is proportional to the x-component of their velocities, $v_x = c\cdot\cos\psi$. Combining these facts, using Equation 4.6, and integrating it over all possible values of the angle ψ, the average gain in energy on crossing the shock from upstream to downstream is:

$$\left\langle\frac{\Delta\varepsilon}{\varepsilon}\right\rangle = \frac{2}{3}\frac{v'}{c}. \tag{4.7}$$

The particle's velocity vector is isotropised without energy losses by scattering in the downstream region. It then recrosses the shock and gains another fractional increase in energy $(2/3)(v'/c)$. Therefore, making one loop across the shock and back again, the average energy increment is:

$$\left\langle\frac{\Delta\varepsilon}{\varepsilon}\right\rangle_{loop} = \frac{4}{3}\frac{v'}{c}. \tag{4.8}$$

Consequently,

$$A' = \frac{\varepsilon}{\varepsilon_{in}} = 1 + \frac{4}{3}\frac{v'}{c} = \frac{v_{sh}}{c}, \tag{4.9}$$

for one round trip. Thus, the acceleration is proportional to the first order in the shock velocity and this is the reason why this acceleration process is also referred to as the first-order Fermi mechanism.

To evaluate the escape probability, $\mathscr{P}$, we use the argument by Bell (1978b). According to classical kinetic theory, the number of particles crossing the shock is $(1/4)N_p c$, where N_p is the number density of relativistic particles. This is the average number of particles crossing the shock in either direction. In the downstream, the particles are swept away from the shock because the particles are isotropic in that frame. This can be viewed as so the particles are removed from the region of the shock at a rate $N_p u_2 = (1/4)N_p v_{sh}$. Thus, the fraction of particles lost per unit time is $((1/4)N_p v_{sh})/((1/4)N_p c) = v_{sh}/c$, and so $\mathscr{P} = 1 - v_{sh}/c$.

Taking into account that $v_{sh} \ll c$ we can write: $\ln\mathscr{P} = \ln(1 - v_{sh}/c) \approx -v_{sh}/c$ and $\ln A' = \ln(1 + v_{sh}/c) \approx v_{sh}/c$. Therefore, inserting these values into equation 4.5 the differential energy

spectrum of high-energy particles is:

$$N(\varepsilon) \propto \varepsilon^{-2}. \qquad (4.10)$$

This is the result we have been seeking and which is in good agreement with observational data.

4.2 Particle injection problem

One of the most outstanding and still unresolved issue for the DSA process is the particle injection problem. CRs that undergo acceleration via the first-order Fermi process have relativistic energies and gyroradii much larger then the internal thickness of the shock transition layer. They see the shock as an infinitesimal discontinuity in the plasma flow and consequently cross the shock front without any interaction with its internal structure. On the other hand, a nonrelativistic particle can be either reflected from the shock front or transmitted toward downstream and thermalized. Hence DSA starts to work only for particles with a certain energy ε_{inj} or higher, i.e., particles should be injected to DSA. Such particles can come from external sources or become energized beyond a thermal pool in some internal shock mechanisms.

The particle energy distribution at a shock with efficient particle acceleration mechanism should consist of three particle populations (Giacalone, 2003, see Figure 4.2): heated at the shock a thermal Maxwellian bulk, non-thermal particles accelerated by an injection mechanism (particles with energy less than ε_{inj}), and high-energy particles with energies larger than ε_{inj}, the spectrum of which can have a form of a power-law distribution. There are two ways to determine ε_{inj} and investigate DSA process by numerical simulations: test particle simulations and self-consistent kinetic particle-in-cell simulations. The diffusive processes of particle acceleration are very slow and involve very large spatial scales. Self-consistent multi-dimensional simulations of DSA that include electron scales would require long simulation times and very large simulation boxes. They are therefore unfeasible with currently available computational resources. Test particle simulations treat particle motions in pre-described electromagnetic fields – the shock evolves according to the MHD equations and test particles do not have any influence on its structure. This is a severe constraint, as in many cases a back-reaction of test particles should be taken into account, because they can generate kinetic plasma instabilities in the system (see, e.g., Bell, 2004, 2005; Kobzar et al., 2017). Thus, a caution needs to be exercised when using test particle simulations for the estimation of the injection threshold and efficiency. Also theoretical considerations can be used for these purposes (Amano
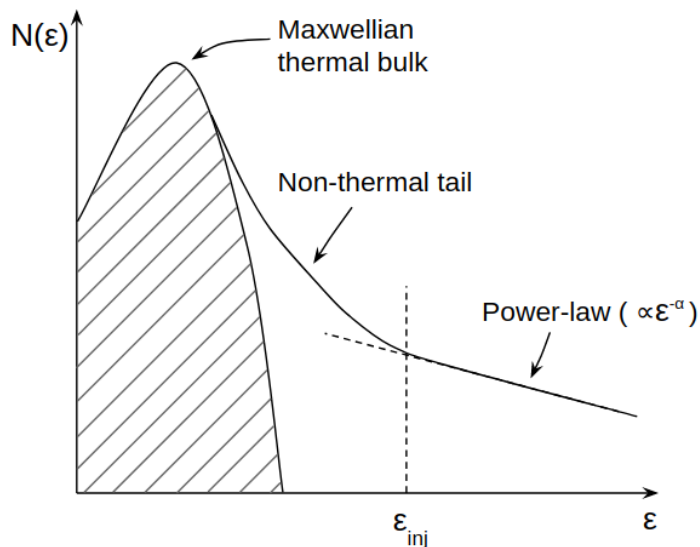
Figure 4.2: Particle energy spectrum at the shock with internal particle injection mechanisms. ε_{inj} is the injection energy.

& Hoshino, 2007, 2010), however, they are still not able to account nonlinear stages of evolution of instabilities occurring in the shock transition and effects of high energy particle backreaction.

Dissipation processes in the shock only heat plasma and do not produce non-thermal particles. Therefore, additional processes that are able to continuously pick-up particles from the thermal bulk and energize them to the injection energy must be identified. In this thesis we discuss particle pre-acceleration, so-called injection, due to microphysical processes occurring in the shock itself. The injection problem is more challenging for electrons then for ions (protons), since the shock width is typically of the order of a few thermal ion's gyroradii. An electron with the same relativistic energy as a proton needs to achieve almost 2000 times higher relativistic Lorentz factor because of its smaller rest mass. Thus acceleration of electrons to the injection energy is more difficult and, in addition to this, less investigated problem.

4.3 Electron injection at nonrelativistic shocks

4.3.1 Injection processes

Recent investigations of nonrelativistic perpendicular shocks demonstrate variety of possible electron injection processes at the shock transition region which depend on the shock parameters. Here some of them, discussed in the context of SNR acceleration, are shorty presented:

- The quasi-standing whistler waves in the foot region are observed at quasi-perpendicular

shocks with relatively low Mach numbers, $M_A \lesssim 15$, and in cold or warm plasmas with plasma beta in the range, $\beta_e = 0.005 - 0.5$ (Riquelme & Spitkovsky, 2011; Umeda et al., 2008). These conditions can occur in older SNRs or old SNRs interacting with giant molecular clouds (Brogan et al., 2006; Bykov et al., 2000; Yamazaki et al., 2006). The whistlers are high-frequency electromagnetic waves excited at the shock foot by returning electrons. If the electron stays in the shock foot long enough it can be scattered and accelerated by the whistler waves.

- Simulations by Matsukiyo et al. (2011) and Guo et al. (2014) show that in the regime of low Mach numbers the shock drift acceleration (SDA) governs the injection of electrons into a Fermi-like acceleration process, that self-consistently persists in the long-term evolution of the shock. SDA can be efficient at oblique shocks (Krauss-Varban & Burgess, 1991; Lever, Quest, & Shapiro, 2001; Wu, 1984). The acceleration occurs while an electron stays in the shock transition region and drifts along the shock surface due to a finite gradient of the magnetic field strength. The electron gains the energy from the motional electric field that is anti-parallel to the drift direction.

- For high-M_A shocks the dominant injection process is the shock surfing acceleration (SSA, Amano & Hoshino, 2009a; Kato & Takabe, 2010b; Matsumoto et al., 2012; Matsumoto, Amano, & Hoshino, 2013; Wieland et al., 2016). In the standard shock surfing mechanism discussed for ions (Sagdeev, 1966; Ucer & Shapiro, 2001), the ions are trapped between the shock front and the upstream by the Lorentz force. During the reflection process, ions travel along the shock front and can be accelerated by the motional/convection electric field. In the case of electrons, these particles can be trapped by electrostatic waves (Buneman waves). While electrons are captured in the electrostatic potential wells, they can be accelerated by the convective electric field. Multiple rapid interactions of electrons with electrostatic waves in the foot region of a shock give rise to efficient SSA. However, the SSA efficiency strongly depends on the plasma beta. In particular, at large plasma temperatures (high plasma beta) the Buneman waves are damped and the acceleration is switched off (Kato & Takabe, 2010b; Matsumoto et al., 2012).

Under certain conditions SSA can also play a role of the injector at low-Mach number shocks (Umeda et al., 2009). The perpendicular shock forms rippled structures by ion-

temperature anisotropy (see Section 6.4). The rippled structures excite a strong electric field component in the shock-normal direction which accelerates reflected ions. The latter excite a rapid growth of the electrostatic Buneman modes, which in turn accelerate electrons via SSA mechanism.

- The Weibel-instability mediated high-Mach number shocks seed appropriate conditions for the formation of current sheets in the shock ramp and a nonlinear decay of the current sheets (Furth et al., 1963) drives magnetic reconnection (Matsumoto et al., 2015) that can provide an additional channel for electron injection.

Two acceleration processes relevant for high Mach number shocks are discussed in the following sections: the SSA by electrostatic Buneman waves at the leading edge of the shock foot and acceleration related to the magnetic reconnection in the Weibel instability region at the shock ramp.

4.3.2 Shock surfing acceleration

The Buneman instability is a type of two-stream or current driven electrostatic instability. As discussed in Section 3.3, this instability can be excited in the foot region of a high Mach number perpendicular shock. Observations of quasi-perpendicular high Mach number shock at the Uranian bow shock (Bagenal & Bridge, 1987) with magnetosonic Mach number $M_{ms} \sim 20$ ($M_{ms} = V_s/V_{ms}$, where $V_{ms} = \sqrt{V_A^2 + c_s^2}$ is the magnetosonic mode velocity) showed strong electron heating. The other observation (Bale et al., 1998) was done by the WIND spacecraft at a quasi-perpendicular region of the Earth's foreshock with $M_{ms} \sim 9.5$ and demonstrated localized electrostatic waves with a bipolar signature, which was interpreted as the Buneman instability. These observational data indicate the presence and nonlinear evolution of the Buneman waves at quasi-perpendicular supercritical shocks. However, modern in-situ observations of planetary shocks and telescope observations of SNR shocks not always can give us a clear understanding of shock structures and particle acceleration processes. On the other hand, numerical simulations is an instrument one can use to explore physical systems with parameters which are difficult to re-create in the laboratory. A number of 1D (Shimada & Hoshino, 2000; Hoshino & Shimada, 2002; Schmitz et al., 2002a, 2002b; Amano & Hoshino, 2007) and 2D (Amano & Hoshino, 2009a; Kato & Takabe, 2010b; Matsumoto et al., 2012, 2013, 2015; Wieland et al., 2016) particle-in-cell (PIC) simulations have been dedicated to the investigation of the electron injection via SSA mechanism, and overview of these studies is

presented in this section.

First 1D PIC simulations of perpendicular shocks with Mach numbers 3.4 and 10.5 were performed by Shimada and Hoshino (2000) for electron plasma beta $\beta_e = 0.15$. They demonstrated that the high Mach number shock ($M_A = 10.5$) exhibited small-scale structures and holes in the electron phase-space in the shock foot caused by electrostatic Buneman waves. Such structures were not observed in the simulation with $M_A = 3.4$. Investigations of shocks (Schmitz et al., 2002b) with $M_A = 10.5$ and higher upstream plasma beta ($\beta_e = 1$) showed suppression of electrostatic waves in the foot region of the shock in the warmer plasma because the thermal velocity spread of upstream electrons was larger then the velocity difference between reflected ions and incoming electrons. This creates conditions not suitable for the Buneman instability (see Section 3.3). Nonthermal electrons were observed in the downstream region only for high Mach number shocks propagating in the cold plasma.

In the next series of studies (Hoshino & Shimada, 2002; Schmitz et al., 2002a), electron trajectories were considered and the role of electrostatic waves in electron acceleration process has been investigated. Figure 4.3 describes the electron SSA mechanism in the 1D case. The top panel shows the trajectory of an electron in the xy-plane. The bottom panel shows the electric field profile, E_x, along the x-axis, and the electrostatic wave associated with the electron hole in phase-space is designated by dashed lines. The electrostatic wave has a bipolar signature with diverging electric field. If an electron transmitted into this electrostatic structure is reflected by the electric field E_x and trapped inside the electrostatic wave structure, it is easily accelerated toward the negative direction of the convective electric field E_y. As the electron's velocity v_y is increased in the E_y field, it can be detrapped and transmitted toward downstream from the electrostatic wave when the Lorentz force becomes larger than the electric force produced by the electrostatic potential. Such quick interactions of multiple electrons with electrostatic waves in a foot region of a shock transition produce nonthermal population of electrons in the downstream spectrum.

Amano and Hoshino (2007) have built the theory of electron injection based on 1D simulation of quasi-perpendicular shocks. Electron acceleration consists of two stages: an initial energization via SSA at the leading edge of the shock foot region and subsequent SDA at the shock front. Electrons finally achieve high energies which potentially is enough to be accelerated further via DSA. However, it should be noted that electron injection in previous studies was explored using 1D simulations only, and at that time it was not clear what to expect
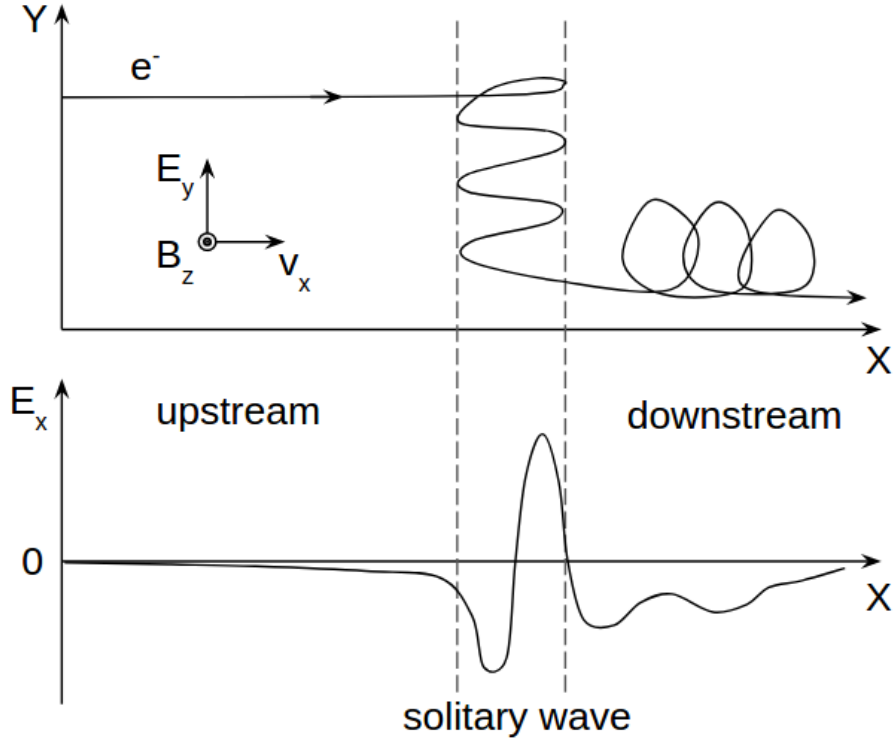
Figure 4.3: Sketch of SSA mechanism in 1D case. Top panel – trajectory of electron in the *xy* plane. Bottom panel – profile of the *x*-component of the electric field. Dashed lines designate an electron hole in the phase-space distribution of electrons.

in multi-dimensional (2D and 3D) cases.

2D PIC simulations have offered a completely new perspective on the electron pre-acceleration. Essentially, all 2D studies performed so far used a so-called 2D3V model. In this model particles are placed in the *xy*-plane, while all three components of their velocities and electromagnetic fields are followed. As discussed in Chapter 3, the magnetic field plays an important role in the shock physics. Here we discuss only perpendicular shocks, with a large-scale magnetic field that is strictly perpendicular to the shock normal. Note however, that in 2D3V simulations the perpendicular magnetic field take different orientations with respect to the simulation plane. In this work, we define the angle, φ, between the large-scale magnetic field and the simulation plane, with the limiting case of $\varphi = 0^o$ for the field contained in the simulation plane, and $\varphi = 90^o$ for the out-of-plane magnetic field configuration (see Section 5.2.2 for details). As discussed in the following, the parameter φ has a profound importance for the particle injection physics observed in the simulations.

Unstable conditions for the Buneman instability have been already discussed in Section 3.3. However, the existence of electrostatic waves only is not enough to produce nonthermal

electrons. The condition of particle trapping was introduced for case of strictly perpendicular shocks in Amano and Hoshino (2009a) and Matsumoto et al. (2012) to estimate physical shock parameters for efficient SSA. Both of these works use 2D3V simulations with out-of-plane configuration with $\varphi = 90^o$. The trapping condition states that electrostatic waves should be strong enough to trap electrons and hold them during acceleration. The maximum energy gain is determined by the balance between the trapping force of the saturated Buneman instability, $F_{BI} = eE_{BI}$, and the Lorentz force, $F_L = evB_0$, for escaping. Here E_{BI} is the electrostatic field generated by the saturated Buneman instability, v is the particle velocity and B_0 is the strength of the large-scale magnetic field. To accelerate a particle up to relativistic speeds, $v \sim c$, the electrostatic force must be greater than the Lorentz force:

$$\frac{F_{BI}}{F_L} = \frac{E_{BI}}{cB_0} \geq 1. \tag{4.11}$$

The maximum intensity of electrostatic waves or the saturation level of the Buneman instability can be estimated as:

$$\frac{\varepsilon_0 E_{BI}^2}{2} = \frac{1}{2}m_e N_0 \Delta v^2 C , \tag{4.12}$$

where C is the conversion rate of the electron drift energy. The conversion rate C has been analyzed by the nonlinear theory of the Buneman instability in 1D case (Ishihara et al., 1980) and shown to depend weakly on the ion-to-electron mass ratio, $C \sim (m_e/m_i)^{1/3}$. In 2D simulations the saturation level is reduced to $\sim 25\%$ of the value estimated above because of the resonant wave-particle interactions (Amano & Hoshino, 2009b). Using $\Delta v = v_e - v_r$, and Equations 3.23, 4.11 and 4.12, the trapping condition can be written as:

$$M_A \geq (1 + \alpha)\left(\frac{m_i}{m_e}\right)^{\frac{2}{3}}. \tag{4.13}$$

For moderate plasma beta shocks ($\beta_e \lesssim 1$) the saturation condition (Eq. 4.13) is always stronger then the unstable condition (Eq. 3.24). The trapping condition depends on ion-to-electron mass ratio, and shows that for larger ion-to-electron mass ratios, higher Mach numbers should be used to satisfy the trapping condition. For the realistic mass ratio of $m_i/m_e = 1836$ the trapping condition gives the value $M_A \approx 180$ which is comparable with Mach numbers of young SNR shocks (see Section 3.3).

Electron acceleration processes in 2D simulations are expected to show some differences

in comparison to the 1D case, due to the system multidimensionality. The particle acceleration process is considered to be a combination of two mechanisms: one is the energization in the shock foot region (1), and the other is the acceleration in the upstream region (2) (see Figure 4.4). If an electron encounters the wave at a certain gyrophase such that the particle velocity in the direction of the wave propagation is approximately equal to the phase velocity, it can travel (or resonate) with the wave during a certain time interval. Since the wave profile propagates with the speed, $\vec{v_w}$, opposite to the incoming electron-ion beam velocity, v_x, the resonant particle can see an inductive electric field in the wave rest frame, $\vec{v_w} \times \vec{B}$, where $\vec{B}$ is the large-scale magnetic field. The mechanism of particle acceleration is similar to SSA in 1D. However, the difference in 2D is that the accelerated particles are not trapped in any waves for long time. Instead they quickly move from one wave to another in a stochastic way, and are accelerated when they are in resonance with the waves. Since the direction of electron acceleration $\vec{a}$ is approximately anti-parallel to the inductive electric field, the accelerated electrons are preferentially transported in the upstream, they move from point (1) in the Buneman zone to the upstream (2). As a result, they undergo further acceleration by the motional electric field (E_y, see Fig. 4.4) in the upstream. The 2D SSA mechanism is thus similar to the ion shock surfing, but in the present case the turbulent electrostatic waves play the role of the particle-reflecting agent. The acceleration of electrons beyond the SSA phase is largely adiabatic. After interaction with Buneman waves the magnetic moment of electrons oscillates around some certain average value defined by the energy boost in the foot region (Matsumoto et al., 2012, 2013).

Description of the SSA mechanism presented above is valid for shocks propagating in moderate-β_e plasmas, $\beta_e = 0.5$, whose Mach number is large enough to satisfy the trapping condition (see, e.g., run C in Matsumoto et al. (2012)). The work of Matsumoto et al. (2012) considers also two additional cases: higher upstream plasma beta, $\beta_e = 4.5$ (run D), and shock Mach number smaller than required by the trapping condition (run B). The analysis of the shock foot structure shows a suppression of the electrostatic Buneman waves in these cases. Consequently, the electron downstream spectra contain significantly smaller numbers of the suprathermal electrons.

The investigation of perpendicular shocks with the angle of $\varphi = 45^o$ was performed by Wieland et al. (2016) with parameters that are close to those for run C in (Matsumoto et al., 2012), where efficient electron acceleration and nonthermal electrons are observed. The trapping condition (Eq. 4.13) is satisfied in simulations by Wieland et al. (2016) and large-
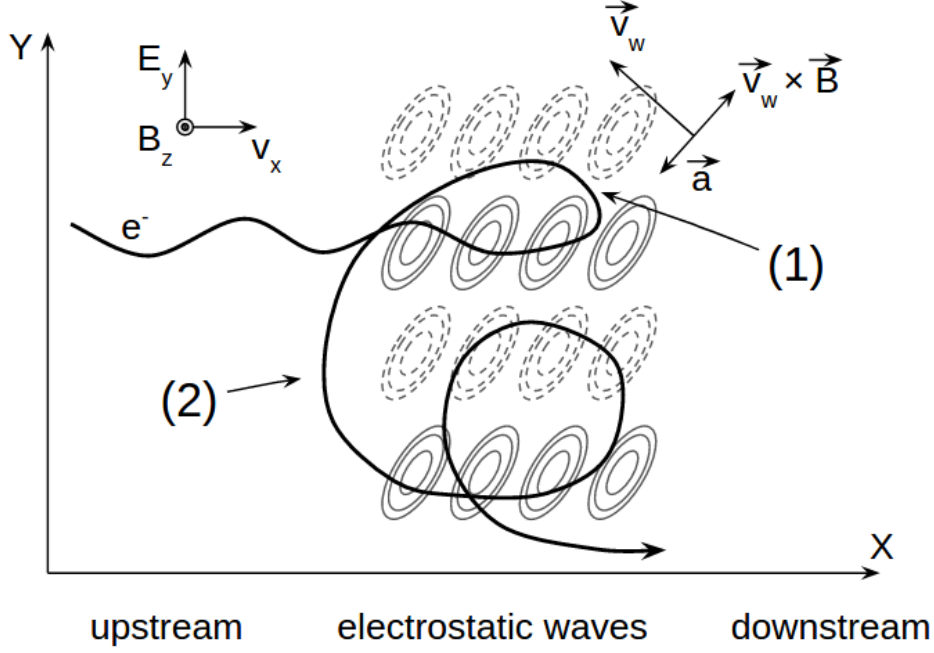
Figure 4.4: Sketch of SSA mechanism in 2D case. The trajectory of accelerated electron is drawn with the solid curved line. (1) – acceleration by $\vec{v}_w \times \vec{B}$ motional electric field in electrostatic Buneman waves region, $\vec{a}$ is the direction of acceleration. (2) – acceleration by motional electric field E_y in the upstream region.

amplitude Buneman waves are observed in the shock foot. However, the downstream electron spectra do not show significant nonthermal tails and are well fitted with relativistic Maxwellians. The authors conclude that Buneman waves' amplitude is not high enough to prevent the escape of relativistic electrons from the waves potential wells. Thus heating of the bulk is observed as opposed to the creation of a spectral tail. There may be additional factors in the microphysics of high-Mach-number shocks mediated by Weibel-filamentation instability that limit the amplitude of Buneman waves or prevent the return of electrons to the foot region. The lack of suprathermal electrons can also be explained by efficient relaxation of electrons via interaction with turbulent structures in the shock transition.

Two studies by Kato and Takabe (2010b) and Matsumoto et al. (2015) are dedicated to the shock investigations with the in-plane magnetic field configuration, $\varphi = 0^o$. Kato and Takabe (2010b) study high Mach number shock $M_A = 100$ propagating in hot plasma with $\beta_e \sim 26$. Despite of the trapping condition being satisfied in the simulation, the kinetic energy distribution of the electrons in the downstream region is fitted very well by relativistic Maxwellian distribution. The authors argue that the high temperature of upstream plasma and reflected ions reduces the Buneman growth rate by about an order of magnitude, thus

nonthermal electrons are not produced. The second study (Matsumoto et al., 2015) investigates electron acceleration in the shock propagating in plasma with $\beta = 0.5$ and which satisfies the trapping condition. However, they report electron acceleration provided rather via magnetic reconnection then the SSA. The large-amplitude Buneman waves are almost not absent in the shock foot, and nonthermal population of electrons is formed mainly via interaction with reconnection sites.

There are few important for the SSA efficiency factors derived from previous studies.

both lower M_A and higher β_e decrease SSA efficiency

Summarizing, the SSA efficiency at perpendicular nonrelativistic high Mach number shocks strongly depends on variety of upstream plasma parameters: plasma beta, Mach number, magnetic field orientation etc. Additional investigations are necessary to resolve this issue.

4.3.3 Magnetic reconnection

Several works using 2D3V PIC shock simulations report the development of the Weibel instability and the formation of Weibel-instability mediated shocks in unmagnetized (Kato & Takabe, 2008; Niemiec et al., 2012) and weakly magnetized (Kato & Takabe, 2010b; Niemiec et al., 2012; Matsumoto et al., 2015; Wieland et al., 2016 plasmas. In such conditions, the Weibel instability is driven by the interaction of ions reflected at the shock overshoot with the incoming plasma beam. The instability generates strong magnetic field in the shock transition region. This field provides an effective dissipation and plasma heating mechanisms at collisionless shocks. The analysis performed by Kato and Takabe (2008) demonstrate that Weibel instability can easily be excited in shocks of young SNRs.

Magnetic reconnection is an ubiquitous plasma process that dissipates the energy stored in the magnetic field by breaking and reconnecting of oppositely directed magnetic field lines. It was reported by Matsumoto et al. (2015) that magnetic reconnection can occur at the Weibel instability region in the case of high Mach number nonrelativistic shocks. The incoming magnetic field lines are strongly deformed through the Weibel instability and spontaneously create thin current sheets (filaments) in the transition region, forming appropriate conditions for magnetic reconnection, namely, a so-called uniform Harris-type current sheets (Harris, 1962). A sheet consists of a thin dense plasma layer confined between two regions of oppositely directed magnetic field lines. Such a configuration is unstable under thermal fluctuations and after a short time period undergoes multiple magnetic reconnection forming X-points and magnetic islands (see Fig. 4.5 and ,e.g., Furth et al., 1963; Oka, Phan, et al., 2010; Dahlin et al.,
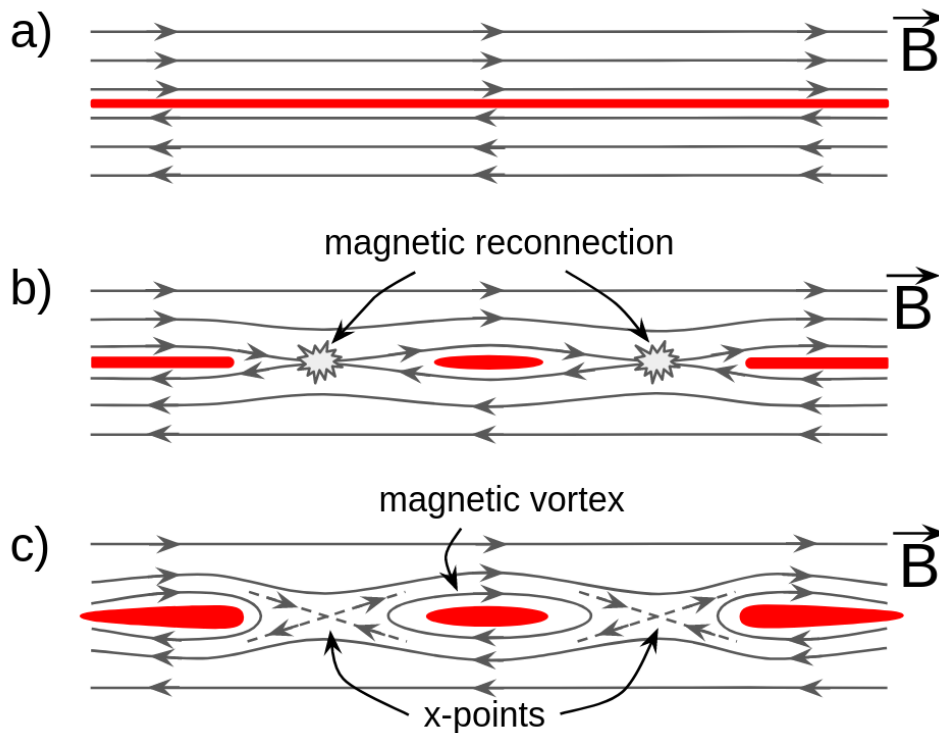
Figure 4.5: Main stages of magnetic reconnection. Panel (a) - initial magnetic field configuration, (b) - magnetic reconnection, (c) - formation of magnetic islands and vortices. Regions with high plasma density are designated with red color.

2014).

During magnetic reconnection the magnetic energy is converted to the kinetic energy of particles. There are variety of acceleration processes occurring during magnetic reconnection which can accelerate electrons up to nonthermal energies:

- Charged particles are effectively accelerated through a Speiser motion in the reconnection region (Speiser, 1965). One of the most efficient trajectory for particle energization among Speiser orbits is the acceleration by the z-component of the electric field when a particle is placed in an X-point (Hoshino et al., 2001; Oka, Phan, et al., 2010);

- During magnetic vortex coalescence a configuration of the magnetic field is formed similar to that at the X-point. Such a configurations is known as the anti-X-line region. Particles can be accelerated by the z-component of the electric field or by bouncing between merging magnetic islands (Oka, Phan, et al., 2010);

- Detailed study of the reconnection region shows that polarization electric field is induced in the boundary between the lobe (part of magnetic vortex close to the X-point) and the plasma sheet (Hoshino et al., 2001; Hoshino, 2005). The acceleration of electron occurs

in the direction perpendicular to both the magnetic field and the polarization electric field and surfing acceleration results (Hoshino, 2005);

- Interactions of particles with curved magnetic field lines with $k \sim 1$, where k is defined as the square root of the ratio of the curvature radius of the magnetic field to the Larmor radius, play an important role in the electron heating and acceleration. This process refers to the curvature-B drift acceleration (Smets, Delcourt, & Fontaine, 1998; Hoshino et al., 2001);

- At the early stage of magnetic reconnection the shape of magnetic islands is preferably elongated (as in Fig. 4.5c). A particle bouncing between ends of the magnetic islands gains energy during contraction of the island via Fermi-like process (Drake, Swisdak, Che, & Shay, 2006)

- Particles can be accelerated, while they are captured by magnetic island, via mechanism which differs from that described in the previous point. "Island surfing" mechanism works during the island development, a particle is accelerated by the z-component of the electric field inside the vortex (Oka, Fujimoto, et al., 2010);

- At the late stage of magnetic reconnection high-energy particles have the tendency to reside outside the magnetic vortices. Merging magnetic islands produce plasma outflows moving from X-points to ambient plasma. Energetic particles will preferably undergo head-on collisions with these outflows, and the process similar to the first-order Fermi acceleration occurs (Hoshino, 2012);

- As the magnetic vortices represent scattering centers, charged particles moving chaotically can randomly interact with magnetic islands undergoing the second-order Fermi-like acceleration.

Investigation of particle trajectories in shock simulation have demonstrated two acceleration processes related to the magnetic reconnection (Matsumoto et al., 2015). During magnetic reconnection plasma flows from an X-point to the center of the magnetic island. Rapid acceleration happens when electron elastically collide with such particle jets ejected from the X-point. Gradual acceleration refers to chaotic interactions with magnetic islands residing in shock region, manifesting the the second-order Fermi acceleration. All other acceleration

processes should be identified in further investigations in order to evaluate the influence of magnetic reconnection on the electron injection efficiency in high Mach number shocks.

CHAPTER 5
PARTICLE-IN-CELL SIMULATIONS

There are two commonly used techniques for studying the complex systems in physics, namely, laboratory experiments that explore real physical systems under controlled conditions, and theoretical investigations, in which analytical or mathematical methods are used to describe the systems according to established physical laws. In spite of the obvious advantage of experimental techniques, there are many physical phenomena difficult or even impossible to recreate in the laboratory. The use of analytical models in application to complex systems with large number of degrees of freedom and/or nonlinearity is also often untractable. In this situation, a rapid growth of supercomputer computational capabilities in recent decades has led to the advancement of a new class of theoretical models, namely, computer modeling, or numerical simulations.

In this section we introduce the particle-in-cell (PIC) numerical method. Our description is based on the THISMPI (**T**wo-and-a-**H**alf-**D**imensional **S**tanford code with **M**essage **P**assing **I**nterface) code, which is used in our investigations. This code is a 2D3V-adapted and modified version of the relativistic electromagnetic PIC code TRISTAN (Three-Dimensional Stanford) (Buneman, 1993) with Massage Passing Interface-based (MPI) parallelization (Niemiec et al., 2008).

5.1 Kinetic description of collisionless plasma

Computer simulations of plasmas comprise three types of approaches based on fluid, hybrid, and kinetic descriptions. The simplest and historically the first approach to be developed is the hydrodynamical or magnetohydrodynamical (MHD) description, in which both electrons and ions are treated as fluids and described by fluid equations. MHD simulations can be applied to large-scale plasma problems. However, this approach is not capable of accurately determining the accelerated population since it explicitly ignores the details of individual particle motion. In hybrid codes electrons are treated as a fluid while ions are treated as individual particles. These codes are used for problems in which ion dynamics and acceleration processes need to be investigated. However, both MHD and hybrid models loose the ability to capture the dissipation and acceleration processes at the electron scales.

Kinetic or full particle simulations are particularly successful in dealing with basic physical problems in which particle distributions deviate significantly from a local Maxwellian

distribution, such as when wave-particle resonances, particle trapping, particle acceleration, or stochastic heating occur. Kinetic codes follow relativistic particle motion in self-consistent electromagnetic fields derived from a solution of the Maxwell's equations. Direct calculation of forces between particles is not feasible even if modern Pflop/s supercomputers are used. This is because about $\sim N^2$ arithmetic operations are required to calculate a force on a particle due to its interaction with all other particles, where N is total particle number. Thus, if we consider a system with, e.g., 10^{10} particles (typical particle number used in modern applications), then the total number of operations will be about 10^{20}. This even on a Pflop/s supercomputer it will take one day to calculate a single simulation time-step. However, this constraint is alleviated in the PIC method.

The PIC techniques have been developed since 1950s (e.g., Harlow, 1955; O. Buneman, 1959; Yee, 1966; Okuda, 1972; Dawson, 1983; Langdon, 1985; Birdsall & Langdon, 1991). The main features of the method and the main differences between real and simulated plasmas are presented below:

- The electric and magnetic field, and the electric charge and current are discretized in space and defined on a computational grid. Particles can have arbitrary positions on the grid. To calculate forces acting on particles the field values are interpolated from the grid points to particle positions. All quantities are discretized in time. This model leads to a linear dependence between the number of arithmetic operations in the simulation and the number of simulated particles, i.e., it requires considerably smaller computational resources then the direct method.

- A large spatial and temporal span exists in plasma processes that are defined by ion and/or electron dynamics. To comply with the limitations in computational resources it is convenient to compress the dynamical ranges by reducing the ion-to-electron mass ratio, m_i/m_e. Reduced ion-to-electron mass ratios, typically in a range from 16 to 400, are frequently used in simulations in order to resolve the characteristic length and time scales of both electrons and ions with available computing resources. Reduced mass ratios in this range should well separate ion and electron scales and thus provide a qualitatively correct picture of the plasma behavior.

- Particle number densities in real plasmas are still out of reach for modern computer simulations. The Debye length is the order of $\lambda_D = 10^5$ m in SNR shock plasmas.

The size of the system we want to simulate should be of the order of the ion skin length $\lambda_{si} \sim (10^4 - 10^5)\lambda_D$. This gives us the number of particles within Debye volume $N_D \sim (10^{13} - 10^{14})$ and the total number of particles in the system $N \sim (10^{17} - 10^{19})$ for particle densities in the range $(10 - 10^2)\text{cm}^{-3}$. To resolve this issue a model of so-called macroparticles is used. In this model, the value $N_D \sim 10$ or even smaller can be used and the collisionless limit will still be met (see,e.g., Birdsall & Langdon, 1991). Each macroparticle represents a large number of real plasma particles. Its charge and mass is numerically much larger then the charge and mass of a real particle. However, the real charge-to-mass ratio is preserved so that a macroparticle behaves according to the same equations of motion as the real one.

The key point of the macroparticle model in PIC simulations is the finite-size particle approach. The fundamental advantage of this approach is that computational particles, being of finite size, interact weaker than point particles. The force acting between two point particles with equal charges is described by a formula $F \propto q^2/r^2$ in the 3D case. The force becomes large
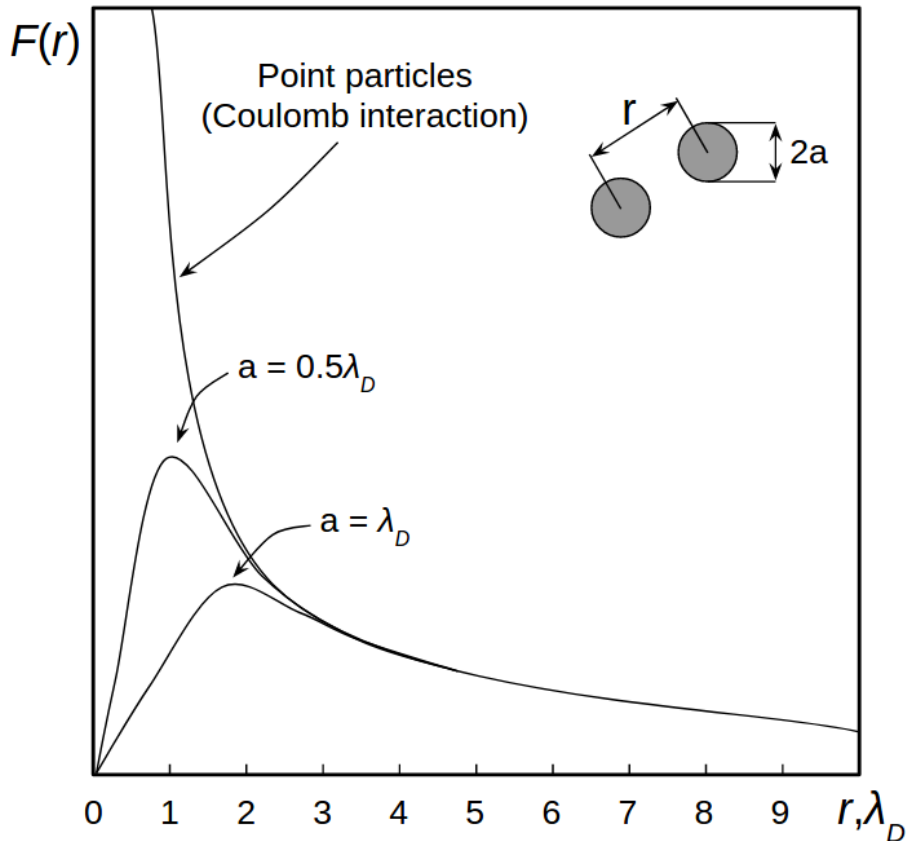

Figure 5.1: The force of an electrostatic interaction between two particles. Cases for point particles and charged clouds with radii of $a = \lambda_D$ and $a = 0.5\lambda_D$ are presented.

at small distances between particles, and when particles pass close to each other they undergo rapidly varying force associated with a collision. The long-distance part of the Coulomb force is responsible for interactions among large number of particles, i.e., for the collective phenomena in plasmas. If we consider an interaction between two circular charge clouds that can freely pass through each other, the interaction force will acquire desirable character provided an appropriate size of the charge cloud is selected. Figure 5.1 illustrates the force of an electrostatic interaction between two point particles and between two charged clouds. One can see that the force goes to zero for particle distances smaller then the particle radius. The reflecting core is suppressed for particle sizes $a \geq \lambda_D$. In this way a low value of the collision rate is achieved in the model and dominant particle interactions are the collective ones. Therefore, the finite-size particle approach represents a valid model of collisionless plasma.

5.1.1 From first principles

The full kinetic description of plasma is based on the Vlasov equation. This equation describes the evolution of particle distribution function $f \equiv f(\vec{x}, \vec{p}, t)$ in a self-consistent electromagnetic field generated by the particles themselves. The Vlasov equation reads:

$$\frac{\partial f_s}{\partial t} + \vec{v}(\vec{p}) \cdot \frac{\partial f_s}{\partial \vec{x}} + q_s(\vec{E} + \vec{v}(\vec{p}_s) \times \vec{B}) \cdot \frac{\partial f_s}{\partial \vec{p}} = 0 , \tag{5.1}$$

where index "s" represents particle species, q is the electric charge of particles and $f(\vec{x}, \vec{p}, t)$ represents the particle density in phase-space at point $(\vec{x}, \vec{p})$ and time t. Electromagnetic fields evolve according to the Maxwell's equations:

$$\begin{aligned} \vec{\nabla} \cdot \vec{E} &= \frac{\rho}{\varepsilon_0} , \\ \vec{\nabla} \cdot \vec{B} &= 0 , \\ \vec{\nabla} \times \vec{E} &= -\frac{\partial \vec{B}}{\partial t} , \\ \vec{\nabla} \times \vec{B} &= \frac{1}{c^2} \frac{\partial \vec{E}}{\partial t} + \mu_0 \vec{j} , \end{aligned} \tag{5.2}$$

where ρ is the electric charge density derived from charge distribution and $\vec{j}$ is the electric current calculated from charge motions. The source terms in Equations 5.2 read:

$$\rho(\vec{x},t) = q \int f(\vec{x},\vec{v},t) \, d\vec{v} \, ,$$

$$\vec{j}(\vec{x},t) = q \int f(\vec{x},\vec{v},t) \, \vec{v} \, d\vec{v} \, . \qquad (5.3)$$

The solution f of the Vlasov equation (Eq. 5.1) satisfies $\frac{d}{dt} f(x(t), v(t), t) = 0$, where $(\vec{x}(t), \vec{v}(t))$ is a solution of the differential system (Filbet, Sonnendrücker, & Bertrand, 2001):

$$\frac{d\vec{p}}{dt} = F(\vec{x}(t), t) \, , \qquad (5.4)$$

$$\frac{d\vec{x}}{dt} = \vec{v}(t) \, . \qquad (5.5)$$

The solutions of this system are called the characteristics of the Vlasov equation. For the plasma particles Equation 5.4 can be written as:

$$\frac{d\gamma m\vec{v}}{dt} = \sum F_{ext} \, , \qquad (5.6)$$

where $\gamma = (1 - v^2/c^2)^{-1/2}$ is the particle relativistic Lorentz factor. The right hand side of Equation 5.6 contains contributions of all forces exerted on the particle. In the plasma, this force is reduced to the Lorentz force induced by the external and self-consistent electromagnetic fields. Thus we have:

$$\frac{d\gamma m\vec{v}}{dt} = \sum_j q(\vec{E}_j + \vec{v} \times \vec{B}_j) \, , \qquad (5.7)$$

where the sum over index "j" contains the electric and magnetic fields generated by all other particles, as well as the external fields. The velocity of a particle v is linked to its position x by Equation 5.5. Thus, if the initial positions and velocities of the particles are known, as well as the external fields, the evolution of a particle ensemble is completely determined by Equations 5.7 and 5.5. The PIC technique thus represents a solution of the Vlasov equation with the method of characteristics.

The main stages of the PIC code computational cycle that solves the system of Equations 5.2, 5.3, 5.7 and 5.5 are presented in Figure 5.2. At each time step the cycle goes through four stages. First stage: the code integrates relativistic equations of motion (Eq. 5.7) for particles moving under Lorentz forces and advances particles to new positions (Eq. 5.5). Second stage: electric charges and/or currents are calculated (weighed to) appropriate grid locations. This corresponds to a discretized form of Equation 5.3. Third stage: Maxwell's equations (Eq. 5.2)
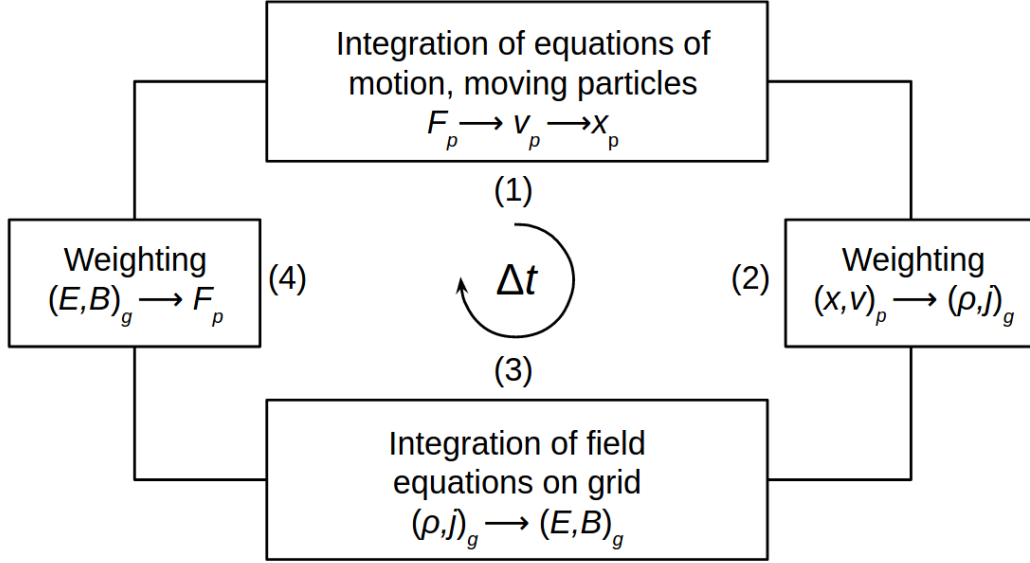
Figure 5.2: A computational cycle in a PIC simulation program. The particles are numbered by index p, the grid index is g.

are integrated on the grid. Fourth stage: new magnetic and electric fields are interpolated to particle positions and new forces are calculated. New computational cycle begins.

In the following sections numerical methods are described that are implemented for each stage in the code that is used for the studies presented in this thesis.

5.1.2 Integration of particle equations of motion

One of the most efficient and commonly used integration scheme for particle equations of motion is a leapfrog method. This method uses the same number of arithmetic operations as the standard Euler integration method, but has a second-order calculation accuracy (see e.g., Birdsall & Langdon, 1991). Figure 5.3 illustrates the leapfrog scheme. Particle positions and forces acting on particle are defined at full-integer time steps, $n\Delta t$. Particle velocities are calculated at half-integer time steps, $(n + \frac{1}{2})\Delta t$. Discretized equations of motion (Eq. 5.7 and 5.5) in the leapfrog scheme, and in the simplest non relativistic limit ($\gamma \to 1$), take a form:

$$m \frac{\vec{v}^{\,n+1/2} - \vec{v}^{\,n-1/2}}{\Delta t} = \vec{F}(\vec{x}^{\,n}) \, , \tag{5.8}$$

$$\frac{\vec{x}^{\,n+1} - \vec{x}^{\,n}}{\Delta t} = \vec{v}^{\,n+1/2} \, . \tag{5.9}$$

The algorithm is thus centered in time. Despite being second-oder accurate, it is also reversible in time. Such an explicit method does not require large RAM memory to store particle
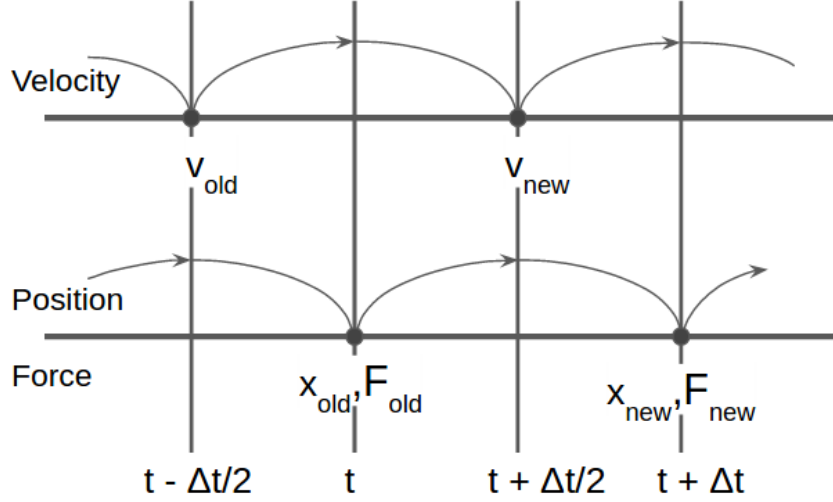
Figure 5.3: Leapfrog scheme for integration of particle equations of motion. Particle positions and forces are defined at full-integer time steps, $n\Delta t$. Particle velocities are calculated at half-integer time steps, $(n+\frac{1}{2})\Delta t$.

data (position and velocity components), as they are needed for one time step only, and are overwritten in the next time step iteration. The leapfrog integration scheme also provides optimum balance between the number of required mathematical operations and the accuracy of calculations. The use of higher-order methods with better computational accuracy (such as the Runge-Kutta method with fourth-order accuracy, see e.g., Birdsall and Langdon (1991)) is not feasible, as the number of arithmetic operations per time step increases, as does the number of preceding time steps for which particle data should be kept in memory to advance particle positions and velocities in time.

The integration of relativistic Newton equations with the Lorentz force is more complicated. A time-centered finite-difference discretization of equation 5.7 is given by the formula:

$$\frac{\gamma^{n+1/2}\vec{v}^{\,n+1/2} - \gamma^{n-1/2}\vec{v}^{\,n-1/2}}{\Delta t} = \frac{q}{m}\left(\vec{E}^n + \vec{v}^{\,n} \times \vec{B}^n\right). \tag{5.10}$$

Here, $\vec{v}^{\,n}$ in the Lorentz force is calculated at full-integer time steps, $n\Delta t$, and thus $\vec{v}^{\,n}$ must be defined between half-integer time steps $(n-1/2)\Delta t$ and $(n+1/2)\Delta t$. The velocity $\vec{v}^{\,n}$ can be defined in a few different ways.

A definition originally used in the TRISTAN code was proposed by Boris (1970) and reads:

$$\vec{v}^{\,n} = \frac{\gamma^{n+1/2}\vec{v}^{\,n+1/2} + \gamma^{n-1/2}\vec{v}^{\,n-1/2}}{2\gamma^n}, \tag{5.11}$$

were γ^n is calculated as:

$$\gamma^n = \sqrt{1 + \gamma^{n-1/2}\vec{v}^{\,n-1/2} + \frac{q\Delta t}{2m}\vec{E}^n}. \tag{5.12}$$

However, this formula leads to spurious forces, because of incorrect computation of $\vec{E} \times \vec{B}$ drift velocity. Let us assume that a particle is placed in constant nonzero electric and magnetic fields in such a way that their mutual contributions cancel, i.e., $\vec{E} + v \times \vec{B} = 0$. If the particle pusher does a correct cancellation of the electric field and magnetic field contributions in the Lorentz force term, there should be no force acting on the particle, and its velocity should stay unchanged. However, if we set $\vec{E} + \vec{v}^{\,n-1/2} \times \vec{B} = \vec{E} + \vec{v}^{\,n+1/2} \times \vec{B} = 0$ and $\gamma^{n-1/2}\vec{v}^{\,n-1/2} = \gamma^{n+1/2}\vec{v}^{\,n+1/2}$ for Equations 5.10, 5.11 and 5.12, the system admits a solution only if $\vec{E}^n = \vec{B}^n = 0$. Consequently, the particle will undergo a spurious force in the general case, where $\vec{E} \neq 0$ and $\vec{B} \neq 0$. To avoid this problem, a new definition of $\vec{v}^{\,n}$ have been proposed by Vay (2008):

$$\vec{v}^{\,n} = \frac{\vec{v}^{\,n+1/2} + \vec{v}^{\,n-1/2}}{2}. \tag{5.13}$$

It leads to an implicit integration scheme, because if we combine Equations 5.10 and 5.13, the velocity at a new time step, $\vec{v}^{\,n+1/2}$, occurs on both sides of the resulting equation. Let us define a new quantity, $\vec{u} = \gamma\vec{v}$. The particle velocity can then be calculated as $\vec{v} = \vec{u}/\sqrt{1 + (\vec{u}/c)^2}$. Thus the value $\vec{u}^{\,n+1/2}$ at half-integer time steps $(n+1/2)\Delta t$ is defined as:

$$\begin{aligned}
\vec{u}^{\,n+1/2} &= s\left(\vec{u'} + \left(\vec{u'} \cdot \frac{\vec{\tau}}{\gamma^{n+1/2}}\right)\frac{\vec{\tau}}{\gamma^{n+1/2}} + \vec{u'} \times \frac{\vec{\tau}}{\gamma^{n+1/2}}\right), \\
\vec{u'} &= \vec{u}^{\,n-1/2} + \frac{q\Delta t}{m}\left(\vec{E}^n + \frac{\vec{v}^{\,n-1/2}}{2} \times \vec{B}^n\right),
\end{aligned} \tag{5.14}$$

and

$$\gamma^{n+1/2} = \sqrt{\frac{\sigma + \sqrt{\sigma^2 + 4(\tau^2 + u^{*2})}}{2}}, \tag{5.15}$$

where $s = 1/(1+t^2)$, $\vec{\tau} = (q\Delta t/2m)\vec{B}^n$, $u^* = \vec{u'} \cdot \vec{\tau}/c$ and $\sigma = (1 + u'^2/c^2) - \tau^2$. The value of $\vec{u}$ at a full-integer time step, which is needed in Equation 5.10 thus reads:

$$\vec{u}^{\,n} = \vec{u}^{\,n-1/2} + \frac{q\Delta t}{2m}\left(\vec{E}^n + \vec{v}^{\,n-1/2} \times \vec{B}^n\right), \tag{5.16}$$

or, equivalently:

$$\vec{u}^{\,n} = \vec{u}^{\,n+1/2} - \frac{q\Delta t}{2m}\left(\vec{E}^n + \vec{v}^{\,n+1/2} \times \vec{B}^n\right). \tag{5.17}$$

The Vay method is used in the THISMPI code.

5.1.3 Yee lattice and integration of Maxwell's equations

The finite-difference time-domain method (FDTD) is today one of the most popular technique for the solution of differential equations. The main reason of the success of the FDTD methods resides in the fact that the method itself is extremely simple, even for programming 3D codes. The FDTD method employs finite differences as approximations to both the spatial and temporal derivatives that appear in Maxwell's equation. The technique was first proposed by Yee (1966).
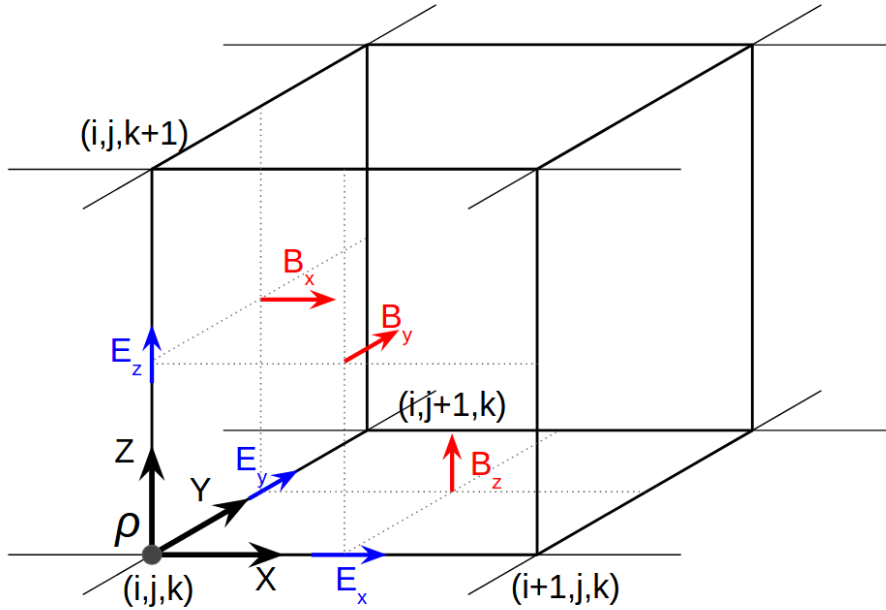

Figure 5.4: The positions of electric and magnetic field components and the electric charge in Yee lattice. Physical quantities presented in the figure correspond to the grid point (i, j, k).

The the Yee lattice in 3D is shown in Figure 5.4 for a single cubic grid voxel with spatial size, $\Delta x = \Delta y = \Delta z = 1$. For the Yee lattice, a convention for fields used here is:

$$E_x(i,j,k) \rightarrow E_x(i+0.5,j,k) \ ,$$

$$E_y(i,j,k) \rightarrow E_y(i,j+0.5,k) \ ,$$

$$E_z(i,j,k) \rightarrow E_z(i,j,k+0.5) \ , \tag{5.18}$$

and

$$B_x(i,j,k) \rightarrow B_x(i,j+0.5,k+0.5) \ ,$$

$$B_y(i,j,k) \rightarrow B_y(i+0.5,j,k+0.5) \ ,$$

$$B_z(i,j,k) \rightarrow B_z(i+0.5,j+0.5,k) \ . \tag{5.19}$$

Thus electric field components are defined at mid-cell edges, and the magnetic field at mid-cell surfaces. For electric currents the same convention as for the electric field is used. The charge density is defined for nodes of the lattice, $\rho(i,j,k) \rightarrow \rho(i,j,k)$. Such definition of quantities with shifts ensures that the change of $\vec{B}$ flux through a cell surface equals the negative circulation of $\vec{E}$ around that surface, and the change of $\vec{E}$ flux through a cell surface equals the circulation of $\vec{B}$ around that surface minus the current through it. Thus, discretized form of Maxwell's equations is simplified considerably.

Let us set $\varepsilon_0 = 1$, $\mu_0 = 1/c^2$ and rewrite the set of Maxwell's equations 5.2 as follows:

$$\vec{\nabla} \cdot \vec{E} = \rho \ , \tag{5.20}$$

$$\vec{\nabla} \cdot \vec{B} = 0 \ , \tag{5.21}$$

$$\frac{\partial \vec{E}}{\partial t} = c\vec{\nabla} \times \vec{B} - \vec{j} \ , \tag{5.22}$$

$$\frac{\partial \vec{B}}{\partial t} = -c\vec{\nabla} \times \vec{E} \ . \tag{5.23}$$

In the THISMPI code to calculate electric and magnetic fields only the last two equations (Eq. 5.22 and 5.23) are used. Time-centered discretizations of Ampere's and Faraday's laws in the Yee lattice are:

$$\frac{\vec{E}^{n+1} - \vec{E}^n}{\Delta t} = \left(\frac{\partial \vec{E}}{\partial t}\right)^{n+1/2} = c(\vec{\nabla} \times \vec{B})^{n+1/2} - \vec{j}^{\,n+1/2} \ , \tag{5.24}$$

$$\frac{\vec{B}^{n+1/2} - \vec{B}^{n-1/2}}{\Delta t} = \left(\frac{\partial \vec{B}}{\partial t}\right)^n = c(\vec{\nabla} \times \vec{E})^n \, . \tag{5.25}$$

Here the leapfrog scheme is used. Electric field, $\vec{E}$, is defined at full-integer time steps, $n\Delta t$. Magnetic field, $\vec{B}$, and electric currents, $\vec{j}$, are calculated at half-integer time steps, $(n + \frac{1}{2})\Delta t$.

For equation 5.21 one can write:

$$\frac{\partial}{\partial t}(\vec{\nabla} \cdot \vec{B}) = \vec{\nabla} \cdot \frac{\partial \vec{B}}{\partial t} = -c\vec{\nabla} \cdot (\vec{\nabla} \times \vec{E}) \equiv 0 \, , \tag{5.26}$$

which means that if initially $\vec{\nabla} \cdot \vec{B} = 0$, then it will always stay equivalent to zero during a simulation. The time derivative of equation 5.20 is:

$$\frac{\partial}{\partial t}(\vec{\nabla} \cdot \vec{E} - \rho) = \vec{\nabla} \cdot \vec{j} - \frac{\partial \rho}{\partial t} \, , \tag{5.27}$$

which in fact is a charge conservation law. Thus, this relation should be supported with a rigorous charge conservation method for current deposition. There are several numerical techniques for solving the continuity equation locally, which allows us to avoid solving Poisson's equation at every time step. In our code the Zigzag scheme is used (Umeda, Omura, Tominaga, & Matsumoto, 2003) which is computationally more efficient than the Villasenor-Buneman technique, originally implemented in the TRISTAN code (Villasenor & Buneman, 1992).

As an example, final formulas for the z component of magnetic field, B_z, and the x component of electric field, E_x, are presented here. In the equations we have removed upper indexes to make formulas more readable, so that E and B variables without upper indexes refer to old time-steps, while variables with index "new" refer to time-step to be calculated. Equation 5.25 for the B_z component can be rewritten as:

$$\begin{aligned}
\frac{\partial}{\partial t}B_z &= (B_z^{new}(i,j,k) + B_z(i,j,k))/\Delta t = \\
&= c[(E_x(i,j+1,k) - E_x(i,j,k))/\Delta y - (E_y(i+1,j,k) - E_y(i,j,k))/\Delta x],
\end{aligned} \tag{5.28}$$

which yields:

$$B_z^{new}(i,j,k) =$$
$$= B_z(i,j,k)) + c[E_x(i,j+1,k) - E_x(i,j,k) - E_y(i+1,j,k) + E_y(i,j,k)],$$

(5.29)

if one applies values $\Delta x = \Delta y = 1$ and $\Delta t = 1$, as used in THISMPI code.

Electric fields can be derived in a similar way. Rewritten equation 5.24 for the E_x component is:

$$\frac{\partial}{\partial t} E_x = (E_x^{new}(i,j,k) + E_x(i,j,k))/\Delta t =$$
$$= c[(B_z(i,j,k) - B_z(i,j-1,k))/\Delta y - (B_y(i,j,k) - B_y(i,j,k-1))/\Delta x] - j_x(i,j,k),$$

(5.30)

which yields:

$$E_x^{new}(i,j,k) = E_x(i,j,k)) +$$
$$+ c[B_y(i,j,k-1) - B_y(i,j,k) - B_z(i,j-1,k) + B_z(i,j,k)] - j_x(i,j,k).$$

(5.31)

One more additional feature for the magnetic field calculation is that we need to know the magnetic field value at an integer time step $\vec{B}^n$ to calculate particle motion using Equations 5.16 and 5.17. One could use a formula $\vec{B}^n = (\vec{B}^{n+1/2} + \vec{B}^{n-1/2})/2$ for this purpose, but in practice the other more accurate treatment for field calculations is used. The method assumes first the field update by half a time-step from $\vec{B}^{n-1/2}$ to $\vec{B}^n$, then the integration of the equations of motion, and in the last step, the field advance for another half time-step, from $\vec{B}^n$ to $\vec{B}^{n+1/2}$.

At the simulation box boundaries some special modifications of integration schemes should be applied implementing desirable boundary conditions. The simplest boundary condition for particles and fields is the periodic one. This condition is easy to implement. In astrophysical applications the most relevant boundary condition for fields is the open boundary, which is able to radiate electromagnetic waves away (absorb the waves). Such radiative open boundary condition was elaborated by Lindman (1975) and it was originally implemented in the TRISTAN code (Buneman, 1993). The open boundary condition can also be implemented for particles. When a charged particle crosses an open boundary, some current should be generated at the boundary in order to account for the influence of already non-existent particle on the particles in the simulation box. In the THISMPI code both periodic and open boundary

conditions are used.

5.1.4 Stability of the integration scheme

Discretization of space and time variables is necessary for numerical simulations. The problem is how large grid spacing and time step one can choose to preserve the numerical stability of the calculations.

Let us consider numerical effects associated with a solution of Maxwell's equation with the leapfrog scheme. For a physical quantity $A(x,t) = A_0 e^{ikx-i\omega t}$ the space-centered discretization reads:

$$\frac{\Delta A(x,t)}{\Delta x} = \frac{A(x_0 + \Delta x/2, t) - A(x_0 - \Delta x/2, t)}{\Delta x} =$$
$$= \frac{e^{ik\Delta x/2} - e^{-ik\Delta x/2}}{\Delta x} A_0(x_0, t) = i\frac{\sin(k\Delta x/2)}{\Delta x/2} A_0(x_0, t) . \qquad (5.32)$$

Thus, $\partial A/\partial x = iKA_0(x_0,t)$, where $K = \frac{\sin(k\Delta x/2)}{\Delta x/2}$. Using time-centered discretization one can derive similar equation for circular frequency $\Omega = \frac{\sin(\omega\Delta t/2)}{\Delta t/2}$. Therefore, dispersion equation for an electromagnetic wave on a grid has the form of $\Omega^2 = c^2 K^2$. Using derived values for Ω and K, one can write:

$$\left(\frac{\sin(\omega\Delta t/2)}{c\Delta t}\right)^2 = \sum_{a=x,y,z} \left(\frac{\sin(k_a\Delta a/2)}{\Delta a}\right)^2 . \qquad (5.33)$$

Obviously, ω is real and the instability growth is not observed, if:

$$1 > (c\Delta t)^2 \sum_{a=x,y,z} \left(\frac{1}{\Delta a^2}\right) . \qquad (5.34)$$

Consequently, in particle simulations with cubic voxel ($\Delta x = \Delta y = \Delta z$) the CFL condition is:

$$c\sqrt{D} < \frac{\Delta x}{\Delta t}, \qquad (5.35)$$

where D represents the number of spatial dimensions of the simulation model. The Equation 5.35 is known as the Courant–Friedrichs–Lewy (CFL) condition (Courant, Friedrichs, & Lewy, 1928). When this condition is violated, the ω roots are complex, and nonphysical growth of waves occurs. If CFL condition is satisfied, no phase or magnitude errors between $\vec{E}$ and $\vec{B}$ are present. Thus in simulations that assume the grid size $\Delta x = \Delta y = \Delta z = 1$ and time

step $\Delta t = 1$, the speed of light should satisfy condition $c < 1/\sqrt{2}$ in 2D and $c < 1/\sqrt{3}$ in 3D. In the THISMPI code the numerical value of $c = 0.5$ is set for the speed of light to satisfy the CFL condition, independent of the simulation dimensionality.

5.1.5 Particle shape

As discussed in Section 5.1 a PIC numerical model for plasma consist of finite-size macroparticles. The macroparticles can take different shapes on the computational grid. The choice the particle shape depends essentially on desirable order of approximation. Particle shapes with corresponding shape functions in the 1D case are presented in Figure 5.5. The shape function defines the charge weights which should be assigned to appropriate grid points.

The most computationally cheap particle shape is the so-called nearest-grid-point (NGP) method or a zero-order approximation (Fig. 5.5 a1, a2). The shape function is defined as:

$$S_1(x) = \begin{cases} 1, & \frac{|x-x_p|}{\Delta x} < \frac{1}{2} \\ \frac{1}{2}, & \frac{|x-x_p|}{\Delta x} = \frac{1}{2} \\ 0, & \frac{|x-x_p|}{\Delta x} > \frac{1}{2} \end{cases}, \tag{5.36}$$

where x is the discretized position coordinate along the grid, and x_p is a particle position (see Fig. 5.5). Thus a particle is assigned to the nearest grid point. However, such particle shapes produce high computational noise and are rarely used in PIC simulations.

The first-order approximation or cloud-in-cell (CIC) model is presented in Figure 5.5 b1, b2 and the shape function reads:

$$S_2(x) = \begin{cases} 1 - \frac{|x-x_p|}{\Delta x}, & \frac{|x-x_p|}{\Delta x} \leq 1 \\ 0, & \frac{|x-x_p|}{\Delta x} > 1 \end{cases}. \tag{5.37}$$

Electric charge of the particle is divided between two adjacent grid points with weights linearly depending on the particle position relative to the grid points. Such a method is more computationally expensive, because each particle contributes its charge into two grid points in 1D case and four grid points in the 2D case.

The particle shape used in our simulations is the triangular-shape-cloud (TSC) or the second-
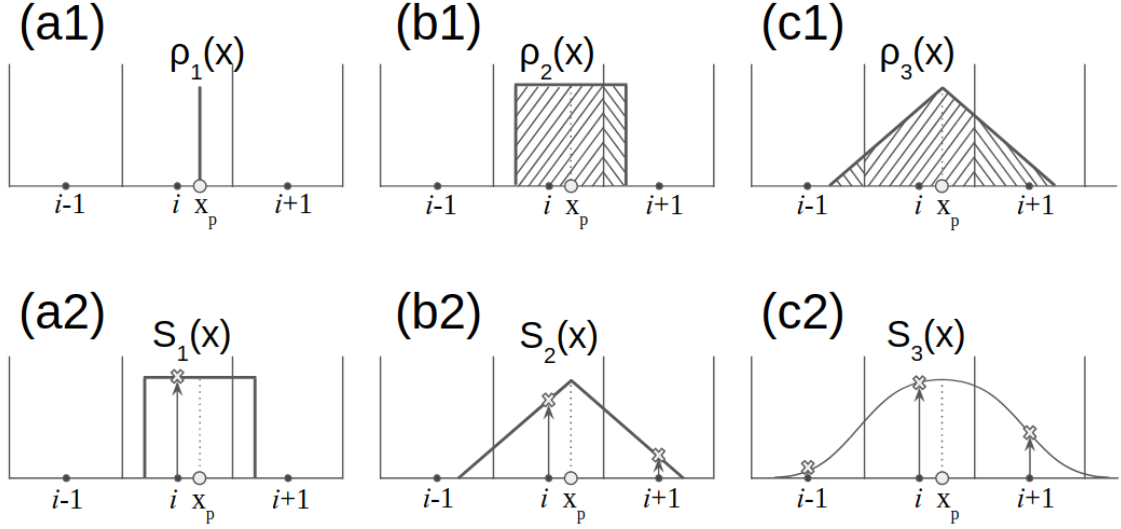
Figure 5.5: Distributions of electric charge for particles (panels *1) and corresponding shape functions (panels *2) for nearest-grid-point (NGP) approximation (panels a*), cloud-in-cell (CIC) approximation (panels b*), and triangular-shape-cloud (TSC) approximation (panels c*).

order approximation (Fig. 5.5 c1, c2) with the shape function:

$$
S_3(x) = \begin{cases} \frac{3}{4} - \left(\frac{x - x_p}{\Delta x}\right)^2, & 0 \leq \frac{|x - x_p|}{\Delta x} \leq \frac{1}{2} \\ \frac{1}{2}\left(\frac{3}{2} - \left(\frac{|x - x_p|}{\Delta x}\right)\right)^2, & \frac{1}{2} \leq \frac{|x - x_p|}{\Delta x} \leq \frac{3}{2} \\ 0, & \frac{|x - x_p|}{\Delta x} > \frac{3}{2} \end{cases}.
\tag{5.38}
$$

A cloud of particle charge has a triangular shape and particle charge is assigned to three grid points in 1D case and nine grid points in 2D case.

Despite the fact that using of high-order particle shape functions is more computationally expensive, application of such a numerical model significantly reduces the numerical noise in the simulations. It works like a low-pass filter cutting the highest frequencies in Fourier decomposition of integrated quantities.

5.1.6 Filters

While using discrete representation of any physical quantity it is important to note that scales smaller then the grid size cannot be reproduced. Consequently, Fourier power spectra of spatial quantities contain so-called aliases, i.e., nonphysical modes. Interactions of physical modes with aliases can disturb physical picture, producing nonphysical instabilities, numerical noise, and spurious forces.

Since it is not possible to distinguish aliases from the physical modes, numerical techniques must be used to decrease the influence of aliases and reduce numerical noise, in order to reach physically correct results in numerical simulations. From programming point of view, the easiest method to damp the numerical noise is to use large number of particles per cell, N_{ppc}. This is because the mean amplitude of small fluctuations decreases as $\sqrt{N_{ppc}^{-1/2}}$. Substantial noise damping can be achieved also by using higher-order computational schemes for integration of field equations, e.g. the fourth-order integration instead of the second order one, and higher-order interpolation methods for calculation of physical quantities (e.g., the shape factor, see Section 5.1.5). In practice, the amount of available computational resources (CPU time, RAM memory) is limited, and quite often the techniques mentioned above are unpractical or too computationally expensive to use. Therefore, in numerical simulations it is also necessary to use additional noise filtering methods. In Fourier-based codes, which operate directly on the Fourier spectra of physical variables, one can simply use low-pass filters to cut high frequencies related to aliases. In the PIC codes in the configuration space, such as the THISMPI code, methods of digital filtering must be used instead.

In a simple binomial 2D filter one substitutes a value of a physical quantity $A(x_{i,j})$ at a grid point (i,j) by the interpolated value $A'(x_{i,j})$ as follows:

$$
A'(x_{i,j}) = A(x_{i,j}) \oplus \begin{pmatrix} a_3 & a_2 & a_3 \\ a_2 & a_1 & a_2 \\ a_3 & a_2 & a_3 \end{pmatrix} ,
$$

where $a_1 = 4$, $a_2 = 2$, $a_3 = 1$, and the sign $\oplus$ designates convolution of matrices. This filter is applied in our code to the source terms in the Maxwell's equations, i.e., the components of currents.

Another method is the Friedman filter (Rambo et al., 1989; Friedman, 1990) which can be used for damping of the so-called numerical Cherenkov emission. Using the dispersion equation for electromagnetic wave on a grid (Eq. 5.33) one can calculate its phase wave velocity at short wavelengths, $k_x \Delta x = k_y \Delta y \simeq \pi$. This velocity equals $v_{phase} \approx 0.9c$. Since relativistic particles may have $v > v_{phase}$ at short wavelengths, they will produce unwanted particle-wave growth due to the numerical Cherenkov effect. The Cherenkov emission imposes a serve problem for PIC simulations and the Friedman filter under certain conditions is an efficient instrument for the solution of this issue. The Friedman filter uses the standard Yee update equation for $\vec{E}$-field and the following update equation for $\vec{B}$-field:

$$\vec{B}^{n+1/2} = \vec{B}^{n-1/2} - \Delta t \vec{\nabla} \times \left[\left(1 + \frac{\theta_F}{2}\right) \vec{E}^n - \theta_F \left(1 - \frac{\theta_F}{2}\right) \vec{E}^{n-1} + \frac{1}{2}(1 - \theta_F)^2 \theta_F \vec{E}'^{n-2} \right],$$
$$(5.39)$$

where $\vec{E}'^{n-2} = \vec{E}^{n-2} + \theta_F \vec{E}^{n-3}$ and $0 \le \theta_F \le 1$. One can see that the standard Yee scheme (Eqs. 5.24 and 5.25) is recovered when $\theta_F = 0$. Detailed investigation of the Friedman filter coefficient (Greenwood, Cartwright, Luginsland, & Baca, 2004) demonstrated that the filter value $\theta_F = 0.05$ efficiently suppresses Cherenkov emission, increasing the phase velocity of high-frequency waves. At the same time, the physics of the phenomena under study is not significantly disturbed. In our simulations the value of $\theta_F = 0.05$ is used as selected by dedicated numerical tests.

5.2 Application – simulations of shock waves

5.2.1 Shock initialization methods

To investigate the shock physics in a numerical simulation, a shock should be formed in some way. There are five commonly used shock initialization techniques (Lembege, 2003):

- The injection method (Burgess et al., 1989; Hoshino & Shimada, 2002; Riquelme & Spitkovsky, 2011;Matsumoto et al., 2012, 2015) uses a plasma beam that is reflected off a conducting wall at one end of the computational box. The reflected plasma interacts with the incoming plasma beam and the shock forms that propagates away from the wall.

- The magnetic piston method (Savoini & Lembege, 1994;Lembege & Simonet, 2001) utilizes an external current pulse which generates strong electromagnetic pulse. The pulse is propagating into the plasma and develops into a shock.

- The plasma release method was used in simulations of Ohsawa (1985) and Lembege and Simonet (2001). This approach assumes initially two different plasmas. It consists of releasing a hot and dense plasma into a relatively colder and less dense ambient plasma. As time evolves, the interaction layer transforms into a collisionless shock, and reaches a regime independent of the initial conditions.

- The initial state in the relaxation method (Leroy et al., 1981, 1982; Umeda et al., 2008, 2009) consists of two uniform regions with different plasma parameters (density,

temperature, pressure, etc.) separated by a thin intermediate layer. Subsequent interaction between two plasmas produces a shock. In general this initialization method is similar to the previous one. The only difference is that in the relaxation method the plasma parameters on both sides of the intermediate layer are defined by Rankine-Hugoniot conditions.

- The flow-flow method is essentially a modification of the injection method. It considers an interaction of two counterstreaming plasma flows. As a result of the two plasma slabs collision two shocks are formed propagating in opposite directions and separated by a contact discontinuity. This setup offers more freedom in the choice of physical parameters because two shocks in plasma environments with different parameters can be investigated at the same time. (e.g., Niemiec et al., 2012; Wieland et al., 2016).

In our simulations we use a modification of the flow-flow method elaborated in Wieland et al. (2016). A detailed description of our simulation setup is presented in the next section.

5.2.2 Simulation setup

In our simulations, two counter-streaming electron-ion plasma beams of equal density collide with each other to form a system of two shocks propagating in opposite directions that are separated by a contact discontinuity (CD; see Fig. 5.2.2). Open boundary conditions for particles and electromagnetic fields are applied in the *x*-direction and periodic boundary conditions are used in the transverse, *y*, direction. The plasma flow is aligned with the *x*-direction, and the streaming velocities of the two slabs are $\vec{v}_L = v_L \hat{x}$ and $\vec{v}_R = v_R \hat{x}$, where the indices L and R refer, respectively, to the *left* and *right* sides of the simulation box, where the beams are injected. The two beams carry a homogeneous magnetic field, $\vec{B}_0$, that is perpendicular to the flow direction and lies in the *yz* plane, forming an angle φ with the *y*-axis. As the magnetic field is assumed to be frozen into the moving plasma, a motional electric field $\vec{E} = -\vec{v} \times \vec{B}_0$ is also initialized in the *left* and *right* beam, with $\vec{v} = \vec{v}_L$ or $\vec{v} = \vec{v}_R$, respectively. The magnetic field strength in both plasmas is equal, $\vec{B}_0 = \vec{B}_L = \vec{B}_R$, and since $\vec{v}_L = -\vec{v}_R$, the motional electric field has opposing signs in the two slabs. To avoid an artificial electromagnetic transient resulting from this strong gradient in the motional electric field when the two plasma beams start to interact, a modified flow-flow method of shock excitation is used Wieland et al. (2016). This method implements a transition zone between the plasma beams, in which the electromagnetic fields are tapered off until they vanish in a small plasma-free area, that initially
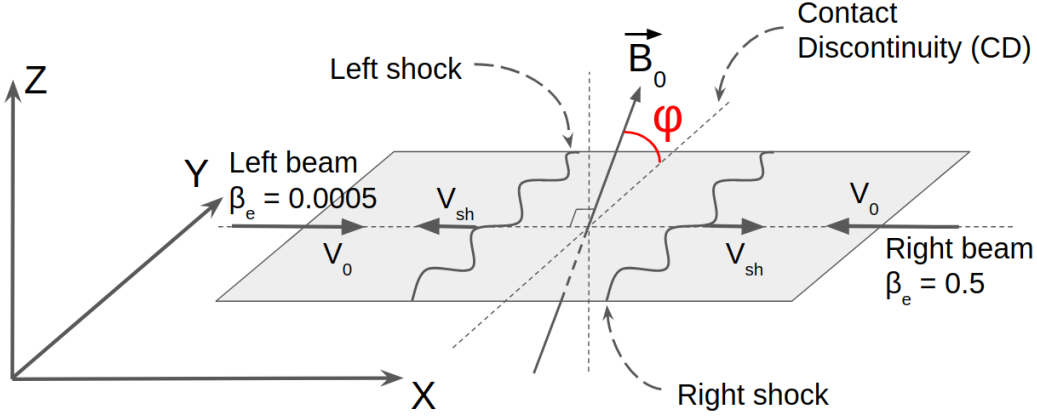
Figure 5.6: Illustration of the simulation setup.

separates the beams. Numerical stability is provided by a current sheet that compensates $\nabla \times \vec{B}_0$ in the transition layer. In addition to providing a clean initialization setup, this method allows one to assume different physical conditions in the colliding beams, e.g., the asymmetry in the density of the slabs, as applied in Wieland et al. (2016).

Here we assume different temperatures for the left and the right plasma beams, that otherwise have the same physical characteristics, including the density. Specifically, we set the plasma beta (see Section 3.2) in the *left* slab to $\beta_{e,L} = 5 \cdot 10^{-4}$ and in the *right* slab to $\beta_{e,R} = 0.5$. The thermal velocities of plasma particles in the two beams thus differ by a factor of $\sqrt{1000} \simeq 32$, and so is the difference in the *sonic* Mach numbers, M_S, of the shocks that form on both sides of the CD. Note, that our choice of plasma beta $\beta_e = 0.5$ for one of the shocks allows for a direct comparison with the results of Matsumoto et al. (2012) and Matsumoto et al. (2013).

The counter-streaming plasma beams move with equal absolute velocities, $v_L = 0.2c = v_R$, so they collide with a relative velocity of $v_{rel} \simeq 0.38c$, where c is the speed of light. Our simulation frame is the center-of-momentum frame of the system. Upon plasma collision, two shocks form and propagate away from the CD in the left and the right plasma. Here we refer to these shocks as to the *left* and the *right* shock, respectively. Because the two unshocked plasmas are cold, the system remains in approximate ram-pressure balance throughout the simulation, and the CD is stationary in the simulation frame. Therefore the simulation frame is coincident with the *downstream* rest frames of the two shocks.

Restricted by available computational resources, we perform our simulations using a 2D3V model, i.e., we keep track of all three components of particle velocities and electromagnetic

fields, and follow particle positions only in the *xy* plane. Since, as was discussed in Section 4.3.2, in such a geometry the physics depends on the orientation of the initially uniform *perpendicular* magnetic field with respect to the simulation plane, we carry out numerical experiments for three values of the angle φ, namely *in-plane* magnetic field $\varphi = 0^o$, $\varphi = 45^o$, and *out-of-plane* magnetic field $\varphi = 90^o$ (see Fig. 5.2.2).

Compression ratio of the downstream plasma, $r = \rho_2/\rho_1$, can be determined by Rankine-Hugoniot conditions in the MHD description (see Sections 3.2 and 3.3). For configurations with $\varphi = 0^o$ and $\varphi = 45^o$, the large-scale field bends particle trajectories out of the simulation plane. Particles thus effectively have three degrees of freedom, hence a non-relativistic adiabatic index $\Gamma_{p,3D} = 5/3$. For the out-of-plane field configuration ($\varphi = 90^o$), particles are tied to the 2D simulation plane, have two degrees of freedom, and $\Gamma_{p,2D} = 2$. Thus, the compression ratio in the limit of high Mach numbers is $r = 4$ and $r = 3$ for $\varphi = 0^o, 45^o$ and $\varphi = 90^o$, respectively. However, in case the shock velocity is a finite fraction of the speed of light (as in our case with $v_{beam} = v_L = v_R = 0.2c$), the Rankine-Hugoniot conditions should be corrected (Blandford & McKee, 1976; Nishikawa et al., 2009). The Lorentz factor of the shock in the *upstream* reference frame is determined by formula:

$$\gamma_{sh} = \frac{(\gamma' + 1)(\Gamma_p(\gamma' - 1) + 1)^2}{\Gamma_p(2 - \Gamma_p)(\gamma' - 1) + 2} \ , \tag{5.40}$$

where $\gamma' = 1/\sqrt{1 - (v_{beam}/c)^2}$ is the Lorentz factor of the shocked gas measured in the frame of the unshocked plasma. Therefore, the shock velocity in the *upstream* frame is:

$$v_{sh} = c\sqrt{1 - \frac{1}{\gamma_{sh}^2}} \ . \tag{5.41}$$

The shock speed in the *simulation* frame can be calculated using a Lorentz transformation:

$$v_{sh,sim} = \frac{v_{sh} + v_{beam}}{1 + (v_{sh}v_{beam})/c^2} \ . \tag{5.42}$$

Note that v_{sh} and v_{beam} are oppositely directed.

The density jump condition at the shock in the *simulation* (*downstream*) frame is:

$$\frac{\rho_2}{\rho_1} = \frac{\Gamma_p\gamma' + 1}{\Gamma_p - 1} \tag{5.43}$$

where ρ_1 and ρ_2 are measured in the *simulation* frame. As the plasma beam moves with the

velocity v_{beam}, density of the unshocked plasma in the *simulation* frame is $\rho_1 \to \rho_1 \gamma'$. Thus, the compression ratio is:

$$r = \gamma' \frac{\Gamma_p \gamma' + 1}{\Gamma_p - 1} \tag{5.44}$$

Therefore, the compression ratio at a high-Mach number shock is $r = 3.97$ and $r = 2.98$ for $\varphi = 0^o, 45^o$ and $\varphi = 90^o$, respectively. The expected shock speeds in the *simulation* frame are $v_{sh,sim} \simeq 0.067c$ for $\varphi = 0^o, 45^o$, and $v_{sh,sim} \simeq 0.1c$ for $\varphi = 90^o$. The shock speeds in the *upstream* frame are $0.263c$ and $0.294c$, respectively.

The two plasma beams are composed of an equal number of ions and electrons, initialized at the same locations to ensure the initial charge-neutrality. Plasma is continuously injected at both sides of the simulation box. The injection layer moves away from the interaction region and is at all times kept at a sufficient distance from it to contain all reflected particles and generated electromagnetic fields in the computational box. At the same time, the distance is close enough so that the beam does not travel too long without any interaction, which suppresses numerical grid-Cherenkov effects and saves computational resources.

5.2.3 Computational model and resources

In THISMPI code parallel computing is implemented using Message Passing Interface (MPI). MPI is a standardized and portable message-passing system widely used in parallel computing. This system allows one to distribute calculations between a large number of CPU-domains. The largest of our simulation contains about $4 \cdot 10^{10}$ particles. Three components of particle velocities and two spatial coordinates are followed. Each quantity is represented by a double-precision floating-point number which occupies 64 bits of memory. Thus, to store particle data for a single time-step about 2TB of RAM memory should be used. The allocation of such a large RAM memory can only be done on large computational clusters in which parallelized codes are used.

In the MPI parallel model the simulation box is divided into rectangular domains of equal size. Each CPU calculates fields, currents, charge density, particle positions and velocities for cells and particles in its own domain. Dedicated MPI procedures are used for communications between domains, i.e., for sending and receiving particles and field values at domain boundaries. The largest number of CPUs used in the production runs performed for this work is 10,080. The simulation time of the longest simulations is about 800 hours. It translates to about 8 million

CPU-hours required for such a simulation.

An important procedure implemented in the THISMPI code is the particle tracing. Each particle in a simulation has an individual (global) ID number. The tracing procedure can thus follow the particle as it moves across CPU-domains. This allows us to store the data of the individual particle (position, velocity and electro-magnetic fields at particle location) for each time step. These data considerably simplifies the analysis and the interpretation of the simulation results.

5.2.4 Numerical tests: Friedman filter and particle shapes

The numerical model used in simulations performed in this study has been extensively tested. In this section we describe the most important tests to demonstrate a validity of the model. In the following we demonstrate an influence of macroparticle shape factor, the Friedman filter, and plasma beta on the stability of the plasma beam with parameters chosen for the main simulation runs (see Section 6.1).

We investigate the stability of a single electron-ion plasma beam moving with the velocity $v_{beam} = 0.2c$ through the grid. To separate the influence of the box boundaries, periodic boundary conditions for particles and electromagnetic fields are applied in both the x and the y-direction. The simulation box size is $L_x = 1500\Delta$ and $L_y = 960\Delta$, where Δ is the size of the grid cell. Ion-to-electron mass ratio equals $m_i/m_e = 100$. The electron skin depth is common in all test simulations and equals $\lambda_{se} = 20\Delta$. For the assumed mass ratio, the ion skin depth is $\lambda_{si} = 200\Delta$. For these tests the number of particles per cell is $N_{ppc} = 20$. The angle between the large-scale magnetic field and the simulation plane is $\varphi = 45^o$. We study two different plasma beta conditions, $\beta_e = 5 \cdot 10^{-4}$ and $\beta_e = 0.5$. The ratio of the electron plasma frequency to the electron gyrofrequency is fixed to $\omega_{pe}/\Omega_e = 12$, thus weakly magnetized plasma is considered.

Table 5.1: Parameters of the test simulations.

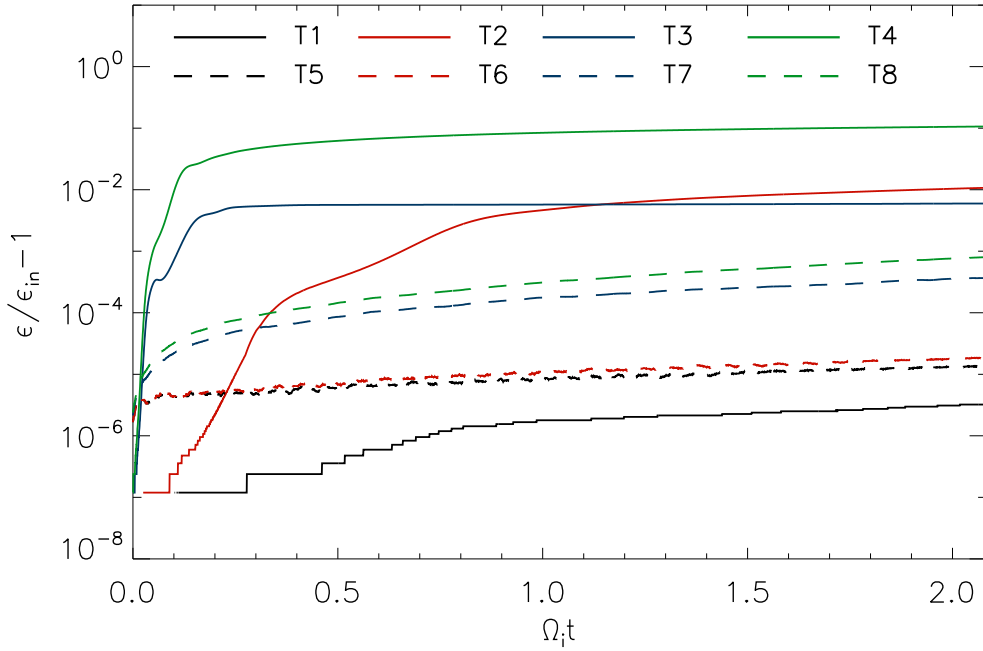| Run	Particle shape	Friedman filter, θ_F	Plasma beta, β_e
T1	TSC	0.05	$5 \cdot 10^{-4}$
T2	TSC	0	$5 \cdot 10^{-4}$
T3	CIC	0.05	$5 \cdot 10^{-4}$
T4	CIC	0	$5 \cdot 10^{-4}$
T5	TSC	0.05	0.5
T6	TSC	0	0.5
T7	CIC	0.05	0.5
T8	CIC	0	0.5

Figure 5.7: The total energy evolution for test runs T1-T8 listed in Table 5.1. Solid and dashed lines are used to show results for the cold ($\beta_e = 5 \cdot 10^{-4}$) and the warm ($\beta_e = 0.5$) beam, respectively. The runs that apply the same numerical model (particle shape and θ_F) but differ in β_e, are color coded. ε_{in} is the initial value of the total plasma energy.

We follow the system evolution for $2\Omega_i$. Table 5.1 lists the test simulation runs performed.

Here we compare the effects of the CIC (runs T3, T4, T7, T8) and TSC (runs T1, T2, T5, T6) particle shapes, which represent the first-order and the second-order approximations, respectively. We also demonstrate the importance of the Friedman filter, by comparing the runs with $\theta_F = 0$ (runs T2, T4, T6, T8) and $\theta_F = 0.05$ (runs T1, T3, T5, T7).

Figure 5.7 shows the total energy evolution for the test simulations. Results for the cold beam are shown with solid lines (T1-T4). One can note, that in all these runs, except for run T1, a rapid energy growth occurs that is stabilized in time only at levels far exceeding the initial energy level ε_{in}. This is mainly due to the numerical grid-Cherenkov effects. Their role is demonstrated in Figure 5.8b that shows the distribution of the electron number density at time $0.32\Omega_i^{-1}$ for run T4. The initial smooth density distribution, N_{e0}, is strongly disturbed in this case by the emission of the numerical grid-Cherenkov short-wave radiation. Particle density deviations are about $\Delta N_e/N_{e0} \sim 1.7$. The final high ratio of $\varepsilon/\varepsilon_{in}$ is caused by the growth of the large-amplitude grid-Cherenkov waves and associated strong plasma heating, that violates initial setup of the cold plasma. The cold beam cannot be stabilized by using a higher-order shape factor (TSC) or the Friedman filter alone ($\theta_F = 0.05$) (runs T2 and T3), respectively.
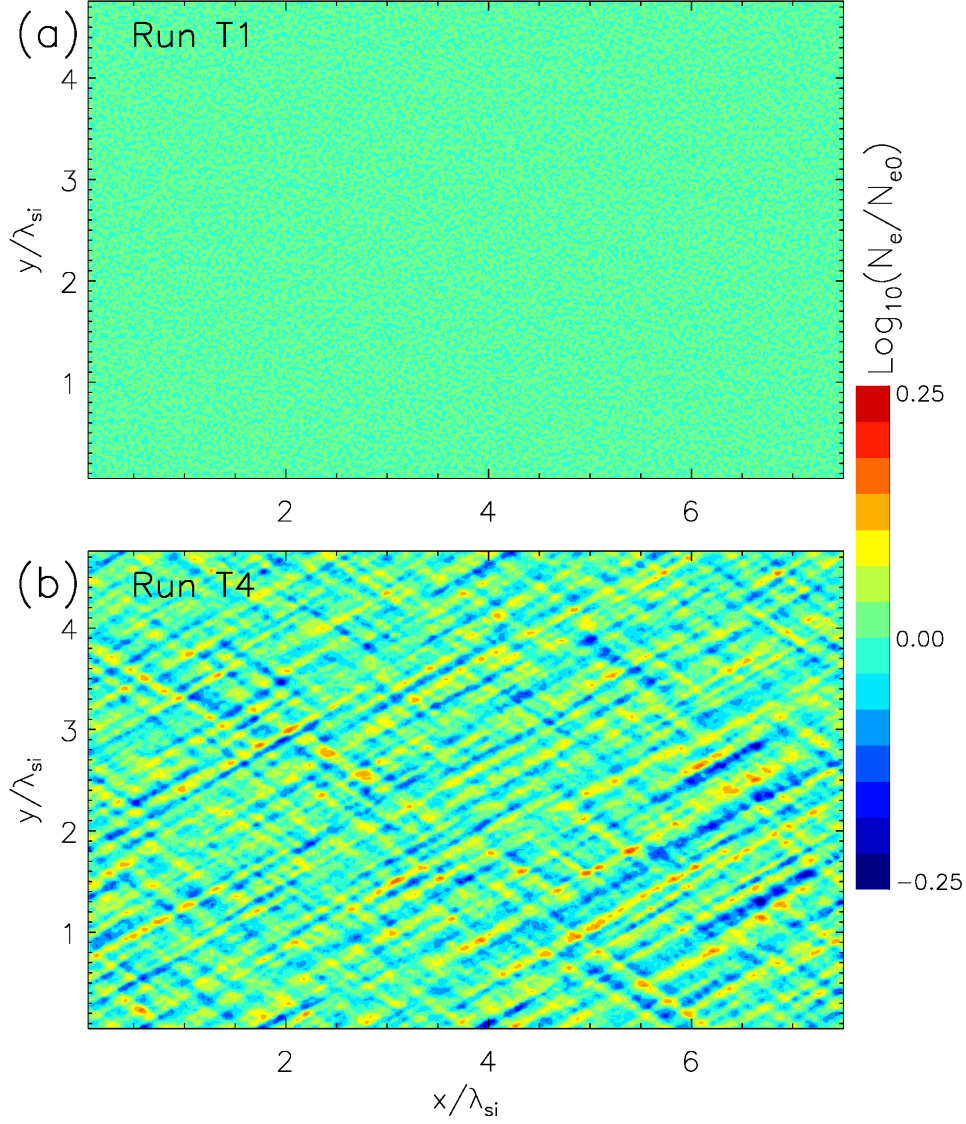
Figure 5.8: Distributions of the normalized electron number density for test runs T1 (panel a) and T4 (panel b). The snapshots were taken at time $T = 0.32\Omega_i^{-1}$.

Only application of these two models at the same time provides the required beam stability (run T1, see Fig. 5.8a). Note that although in run T1 the saturated total energy level is still more then the order of magnitude larger than the required initial one, in a shock simulation the time the beam is allowed to travel without interaction is very small ($< 0.5\Omega_i^{-1}$, see Section 5.2.2). Therefore, injected cold plasma beams maintain their low temperature until they become heated by physical shock interactions and not numerical effects.

The warm beam with $\beta_e = 0.5$ is more stable (runs T5-T8, dashed lines in Fig. 5.7), because thermal particle motions can suppress instabilities caused by the Cherenkov emission. However, particle shape is still important. The use of the TSC model leads to a decrease in

the total energy level by a factor of $50 - 100$ (compare runs T5, T6 with T7 and T8). The Friedman filter becomes less important for the warm plasma beam, because the effect of the Cherenkov emission is already suppressed by temperature. However, the energy growth can still be decreased by a factor of $2 - 3$ with the filter strength $\theta_F = 0.05$.

As the numerical model, including the Friedman filter parameter, should be the same in both plasma beams with different temperatures, in our production runs we take the TSC model for the particle shape and the value of $\theta_F = 0.05$ for the Friedman filter. Note that the results of the test simulations do not significantly depend on the ion-to-electron mass ratio, as long as sufficient resolution in terms of the electron skin depth is assumed. All production runs have $\lambda_{se} = 20\Delta$, as in tests described here.

5.2.5 Numerical tests: number of particles per cell

As discussed in Section 5.1.6, large number of particles per cell, N_{ppc}, helps damping the numerical noise. However, the number of arithmetic operations needed to perform a simulation grows linearly with N_{ppc}. Taking into account limited computational resources we need to find an appropriate value of N_{ppc} that allows us to maintain desirable accuracy of calculations.

Typical values of N_{ppc} commonly assumed for shock simulations are in the range $10 - 50$ (e.g., Amano & Hoshino, 2009a; Kato & Takabe, 2010b; Matsumoto et al., 2012, 2013; Wieland et al., 2016). Here we present a comparison of two shock simulations with a setup described in Section 5.2.2 with $N_{ppc} = 10$ (run N10) and $N_{ppc} = 40$ (run N40). Out-of-plane magnetic field configuration, $\varphi = 90^o$, is used. Ion-to-electron mass ratio $m_i/m_e = 50$. The electron skin depth is again $\lambda_{se} = 20\Delta$, so for the selected mass ratio the ion skin depth is $\lambda_{si} \approx 141\Delta$. All other parameters are as in tests T1 and T5. The Alfvén Mach number of the shocks that are formed $M_A = 22.6$. The sonic Mach number equals $M_s = 1118$ and $M_s = 38$ for shocks propagating in the cold and the warm plasma, respectively. The simulation time is the same for both runs and equals $T = 6.5\Omega_i^{-1}$. Final simulation box sizes are $L_x = 20000\Delta$ and $L_y = 864\Delta$.

Figure 5.9 compares the energy spectra of electrons in the downstream region at time $T = 6.5\Omega_i^{-1}$ for runs N10 and N40. Electrons are collected from regions behind the overshoot with the size of $L \approx 28\lambda_{si}$. Spectra are almost identical. Downstream temperatures of electrons are $k_B T_{e,N10} = 0.022$ and $k_B T_{e,N40} = 0.02$. Nonthermal tails (high-energy part of the spectra above the Maxwellian fit) contain similar number of electrons, i.e., $\sim 5\%$. Note that the observed shock structures are virtually identical, though run N40 is less noisy, as expected.

We conclude that the number of particles per cell, N_{ppc}, does not impose a significant
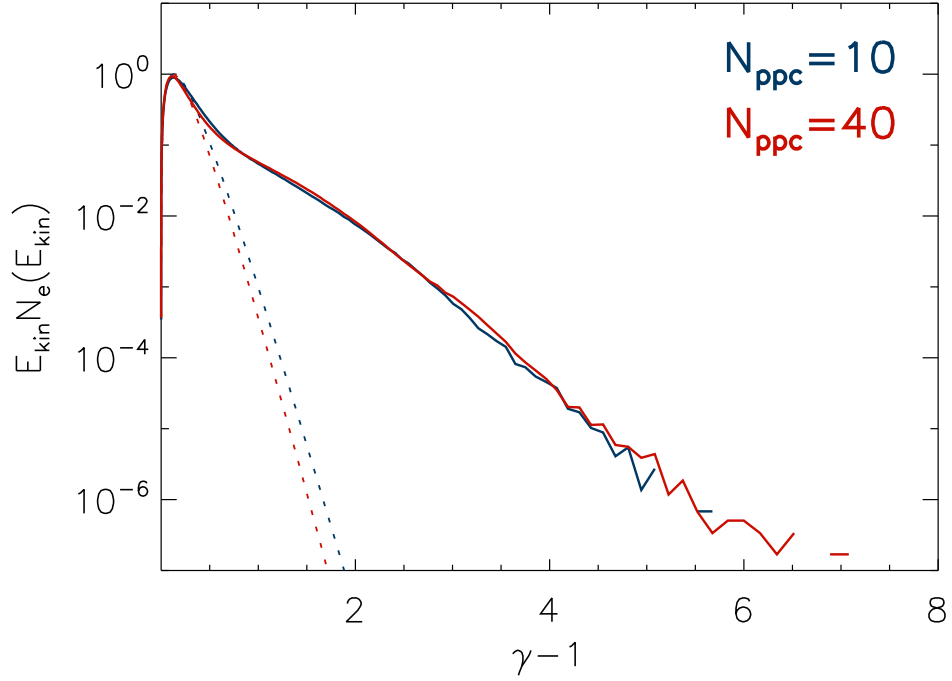
Figure 5.9: Electron spectra in the downstream region of the moderate-β_e shocks for runs N10 (blue line) and N40 (red line). The dashed lines represent fits of a relativistic Maxwellian to low-energy part of the spectra.

influence on the electron acceleration processes at shocks under study. For our main simulations we thus use $N_{ppc} = 20$ as a compromise between the desired calculation accuracy and the allocated computational resources.

CHAPTER 6
PIC SIMULATIONS OF PERPENDICULAR SHOCKS

Cosmic rays represent essential and important part of radiation coming from space. Identification of acceleration mechanisms responsible for energization of galactic population of cosmic rays up to energies 10^{15}eV is important for understanding many plasma phenomena in astrophysical environments. Supernova paradigm of cosmic ray acceleration assumes that galactic cosmic rays are accelerated via diffusive shock acceleration (DSA) mechanism at supernova remnants. This mechanism requires additional pre-acceleration process to pick up particles from the thermal bulk for further energization via DSA.

The aim of this study is to investigate injection of electrons at perpendicular high Mach number shocks for the parameters which are applicable for SNR shocks. Two relevant injection processes are scrutinized here, namely, the shock surfing acceleration (SSA) by electrostatic Buneman waves at the leading edge of the foot region and the acceleration associated with magnetic reconnection in the Weibel two-stream instability region in the shock ramp. As discussed in Section 4.3.2, the role in the SSA efficiency of the large-scale magnetic field configuration in 2D simulations is still not resolved. We address this problem by performing simulations with all identical parameters except for the magnetic field orientation. Such simulations also provide indications on the efficiency of the acceleration processes at high Mach number shocks under fully three-dimensional geometry. It is already known from previous studies that the Buneman instability is strongly suppressed at shocks propagating in plasmas with high electron plasma beta β_e due to high thermal velocities of incoming electrons. Our simulations cover a range of low electron plasma beta. There are variety of electron acceleration processes associated with magnetic reconnection (see Section 4.3.3). A study by Matsumoto et al. (2015) reports only two of them. We investigate another possible acceleration mechanisms and the influence of magnetic reconnection on the downstream electron spectra and non-thermal electron population. The efficiency of electron acceleration via magnetic reconnection for simulation with different ion-to-electron mass ratios is scrutinized.

6.1 Simulation parameters

The simulations presented in this thesis are conducted in 2D3V configuration, i.e., we follow two spatial coordinates of particle positions and all three components of particle velocities and electromagnetic fields. The choice of this model is enforced by available computational

resources. Since, as we discussed in Section 4.3.2, in 2D3V geometry the physics depends on the orientation of the initially uniform *perpendicular* magnetic field with respect to the simulation plane we perform seven numerical experiments with three different values of the angle φ, namely in-plane magnetic field, $\varphi = 0^o$ (runs A, B, C, and D), $\varphi = 45^o$ magnetic field configuration (runs E and F), and out-of-plane field configuration $\varphi = 90^o$ (runs G). The simulation setup (see Section 5.2.2) assumes two shocks propagating in plasmas with different plasma beta, which we set to $\beta_{e,L} = 5 \cdot 10^{-4}$ in the *left* slab and $\beta_{e,R} = 0.5$ in the *right* slab. So for a single run the only different parameter of the two shocks is the temperature, while all the other parameters, e.g., M_A, remain the same. Run-specific parameters are listed in Table 6.1. Note that the digits in the run designations refer to the *left* ($\beta_{e,L} = 5 \cdot 10^{-4}$, runs *1) and *right* ($\beta_{e,R} = 0.5$, runs *2) shock, respectively. If a designation without a digit is used, e.g., run A, it means that a discussion concerns both shocks.

As noted, the magnetic field in both plasma beams is initially equal, $\vec{B} = \vec{B}_0$. We consider weakly magnetized plasmas, and the ratio of the electron plasma frequency (Eq. 3.2) to the electron gyrofrequency (Eq. 3.16) is in range $\omega_{pe}/\Omega_e = 12 - 13$. These values of plasma magnetization have been chosen in order to satisfy the unstable (Eq. 3.24 and 3.25) and trapping (Eq. 4.13) conditions in the Buneman waves excited in the shock foot. The sonic and Alfvénic Mach numbers of the two shocks depend on the orientation angle of the uniform magnetic field with respect to the simulation plane, φ. The sound speeds differ by a factor of $c_s(0^o, 45^o)/c_s(90^o) = \Gamma_{p,3D}/\Gamma_{p,2D} = \sqrt{5/6}$ for the same electron plasma beta, β_e. For a moderate plasma beta ($\beta_e = 0.5$), the sound speeds are a factor of $\sqrt{1000}$ larger then for cold plasma beta ($\beta_e = 5 \cdot 10^{-4}$).

The compression ratio at shocks that form in simulations runs A-F ($\varphi = 0^o, 45^o$) is $r = 3.97$. The shock speeds in the *upstream* and the *simulation* rest frames are $v_{sh} = 0.263c$ and $v_{sh,sim} \simeq 0.067c$, respectively. In simulation runs G the respective values are $r = 2.98$, $v_{sh} = 0.294c$, and $v_{sh,sim} \simeq 0.1c$ (see Section 5.2.2).

We calculate the sonic and Alfvénic Mach numbers of the shocks in the upstream reference frame, and their values are provided in Table 6.1. Thus, here we study perpendicular shocks in a regime of high Mach numbers, $M_A \gtrsim 20$ and $M_s \gtrsim 35$, and in all cases we should expect efficient electron acceleration (see Section 4.3.2).

We assume the ion-to-electron mass ratio of $m_i/m_e = 50 - 400$ and use 20 particles per cell per particle species for both plasma slabs. The electron skin depth in the upstream plasma is

common in all simulations runs and equals $\lambda_{se} = 20\Delta$. For the chosen mass ratio, the ion skin depth is $\lambda_{si} = \sqrt{m_i/m_e}\lambda_{se}$. Here we use λ_{si} as the unit of length. The time scale and all temporal dependencies are given in terms of the upstream ion Larmor frequency, Ω_i^{-1}. The simulation time, $t \approx (5-8)\Omega_i^{-1}$, is chosen to cover at least few shock reformation cycles. The time-step we use is fixed and equals $\delta t = \frac{1}{40}\omega_{pe}^{-1} = \frac{1}{40}\lambda_{se}/c$.

The transverse size of the simulation box is in the range $L_y = (6-24)\lambda_{si}$. The transverse box sizes are significantly larger than those used in earlier studies (e.g. Matsumoto et al., 2012, 2015; Wieland et al., 2016). This is because in runs A-F we expect to observe turbulent magnetic reconnection within the shock structure (Matsumoto et al., 2015), a proper investigation of which requires appropriate statistics for magnetic filaments formed in the shock ramp (see Section 4.3.3).

The simulation parameters are also chosen to enable direct comparison of our results with other simulations of high Mach number perpendicular shocks by Kato and Takabe (2010b); Matsumoto et al. (2012, 2013, 2015) and Wieland et al. (2016). These works investigate shocks in two dimensions with the assumed configuration of the large-scale magnetic field, the angle φ of either $\varphi = 0^o$, 45°, or 90°. The ion-to-electron mass ratios assumed are $m_i/m_e = 30 - 225$, the electron plasma beta are in the range $\beta_e = 0.0015 - 26$, and Alfvén Mach numbers satisfy the trapping condition (Eq. 4.13). In this work three different perpendicular magnetic field configurations are systematically studied using the same numerical model. In addition, our parameter choice extends the parameter range covered in earlier works to lower values of the electron plasma beta and higher ion-to-electron mass ratios.

Results of this thesis are presented in two parts. The first part investigates the influence of the magnetic field orientation with respect to the simulation plane on the shock physics. Discussion is based on simulation runs B, F and G and presented in Sections 6.2-6.5. These three types of simulations differ in the orientation of the upstream magnetic field: in-plane ($\varphi = 0^o$, runs B1 and B2), $\varphi = 45^o$ (runs F1 and F2) and out-of-plane ($\varphi = 90^o$, runs G1 and G2). The runs assume the ion-to-electron mass ratio of $m_i/m_e = 100$. The choice of such mass ratio enables a direct comparison with simulation run C of Matsumoto et al. (2012) performed for $\varphi = 90^o$. We discuss the overall shock structure (Section 6.2), shock self-reformation and rippling (Section 6.3), differences in the evolution of the Buneman modes (Section 6.4), the influence of these modes on electron pre-acceleration (Section 6.5.1), the main features of electron acceleration for the three magnetic-field configurations (Section 6.5.2 and 6.5.3), the

Table 6.1: Parameters of the Simulations and Derived Shock Properties.
Note. – Parameters of the simulation runs described in this thesis. Listed are: the orientation of the uniform large-scale perpendicular magnetic field with respect to the 2D simulation plane, φ, ion-to electron mass ratio, the simulation time in terms of the upstream ion Larmor frequency, Ω_i^{-1}, the transverse size of the computational box in units of the ion skin depth, λ_{si}, Alfvén and sonic Mach numbers of the shocks, M_A and M_s, and the electron plasma beta, β_e, of the upstream plasmas.

Run	φ	m_i/m_e	$T[\Omega_i^{-1}]$	$L_y[\lambda_{si}]$	M_A	M_s	β_e
A1	0°	50	8.3	6.3	22.6	1096	$5 \cdot 10^{-4}$
A2	0°	50	8.3	6.3	22.6	35	0.5
B1	0°	100	8.1	24	31.7	1550	$5 \cdot 10^{-4}$
B2	0°	100	8.1	24	31.7	49	0.5
C1	0°	200	6.3	11.9	44.9	2192	$5 \cdot 10^{-4}$
C2	0°	200	6.3	11.9	44.9	69	0.5
D1	0°	400	5	8.2	68.7	3363	$5 \cdot 10^{-4}$
D2	0°	400	5	8.2	68.7	106	0.5
E1	45°	50	8.3	6.3	22.6	1096	$5 \cdot 10^{-4}$
E2	45°	50	8.3	6.3	22.6	35	0.5
F1	45°	100	8.1	24	31.7	1550	$5 \cdot 10^{-4}$
F2	45°	100	8.1	24	31.7	49	0.5
G1	90°	100	8.1	12	35.5	1581	$5 \cdot 10^{-4}$
G2	90°	100	8.1	12	35.5	55	0.5

influence of shock self-reformation on acceleration processes (Section 6.5.4), and the resulting electron spectra downstream of the shock (Section 6.5.5).

The second part of the thesis is based on simulation runs with the in-plane ($\varphi = 0^o$, runs A-D) and $\varphi = 45^o$ (runs E and F) magnetic field configurations (Section 6.6). In this part we discuss the effect of magnetic reconnection which occurs in the shock ramp. The influence of ion-to-electron mass ratio on the acceleration efficiency via magnetic reconnection is explored. We discuss properties of magnetic reconnection events, magnetic vortex (island) generation rate (Section 6.6.1), acceleration processes in the magnetic reconnection region (Section 6.6.2), and the electron spectra downstream of the shock (Section 6.6.3).

6.2 Global shock structure

This section gives an overview of shock structures observed for the three magnetic field configurations. Figure 6.1 shows electron density maps in the shock region in panels (a1), (a2), (b1), (b2), and (c1), (c2), respectively, for runs B1, B2, F1, F2, and G1, G2. The ion phase-space distribution plots for runs B1, F1, and G1 are presented in Figure 6.2. These figures
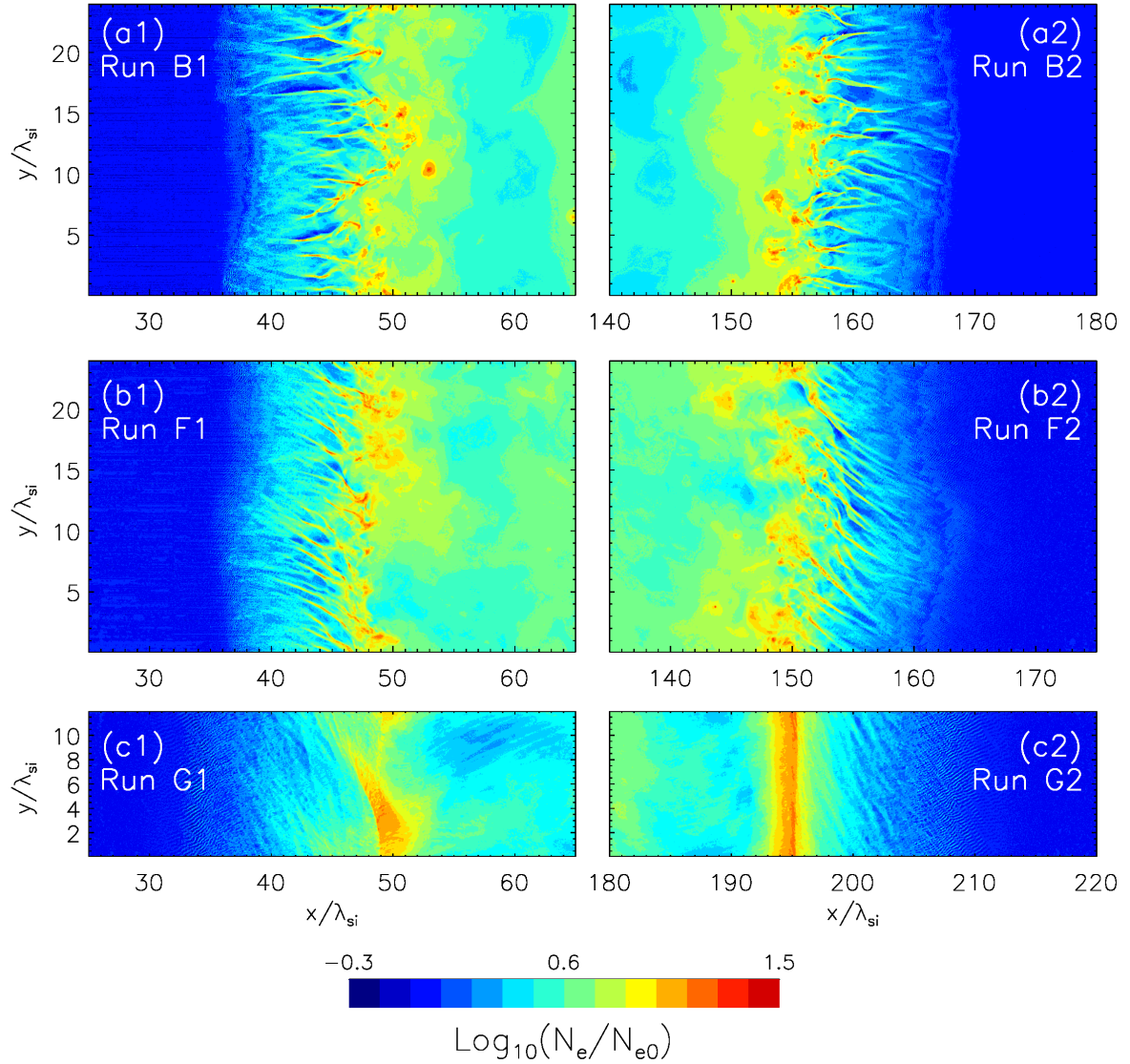
Figure 6.1: Distributions of the normalized electron number density at shocks propagating in cold and warm plasmas. Panel (a1): run B1 at $t\Omega_i = 7.625$, panel (a2): run B2 at $t\Omega_i = 8.125$, panel (b1): run F1 at $t\Omega_i = 7.5$, panel (b2): run F2 at $t\Omega_i = 7.25$, panel (c1): run G1 at $t\Omega_i = 7.75$, panel (c2): run G2 at $t\Omega_i = 7.375$. A logarithmic scaling is used.

present the system at times close to the end of the simulation runs and specifically at a phase of shock reformation in which the largest number of shock-reflected ions appear, and consequently the Buneman waves in the shock foot reach maximum amplitudes. These times differ slightly between runs and are $t\Omega_i = 7.625$ for run B1, $t\Omega_i = 8.125$ for run B2, $t\Omega_i = 7.5$ for run F1, $t\Omega_i = 7.25$ for run F2, $t\Omega_i = 7.75$ for run G1, and $t\Omega_i = 7.375$ for run G2. Note that the system already contains fully-formed self-sustained shocks. The phase of the shock reformation in runs *2 may not coincide with the same phase in the left shocks, as shocks in both plasma slabs evolve independently at times $t\Omega_i \gg 2$.
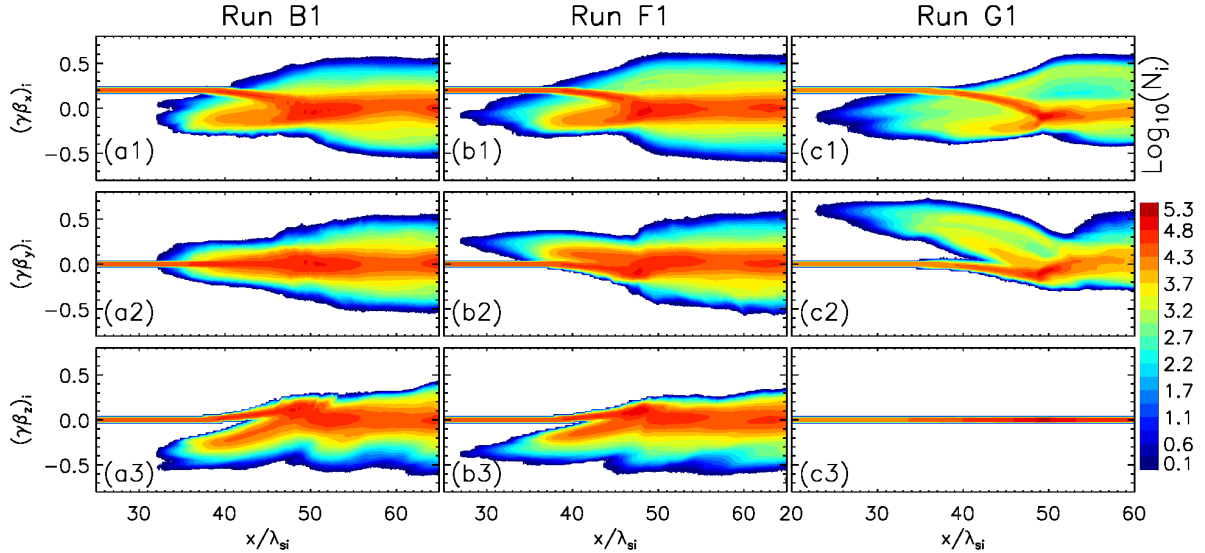
Figure 6.2: Phase-space distributions of ions for the *left* shock regions shown in Fig. 6.1, averaged over the spatial coordinate y. From top to bottom, shown are the x, y, and z-components of particle momenta, $\gamma\beta$, from left to right, for run B1, F1, and G1. A logarithmic scaling is used.

The shock structures in runs with moderate plasma beta case ($\beta_e = 0.5$) are almost identical to those in moderate plasma beta (Fig. 6.1). As mentioned in Section 3.3, the structure of supercritical shocks is determined by the fraction of upstream plasma ions that are reflected from the shock front. Reflected ions gyrate around the magnetic-field lines in the upstream region, exciting various plasma instabilities. For shocks with high Alfvén Mach number, the most relevant instabilities are the Weibel-type filamentation instability in the shock ramp and the Buneman instability in the shock foot. Ion reflection also leads to the so-called overshoot, i.e., plasma compression at the shock front that exceeds the compression expected from the Rankine-Hugoniot conditions in the MHD description (see Sections 3.2 and 3.3). The overshoot in runs G1 and G2 with the out-of-plane uniform magnetic field can be approximately identified in Figures 6.1c1, c2 with a largely-coherent compression structure at $x/\lambda_{si} \approx 50$ ($N_e/N_{e0} \approx 13$) and at $x/\lambda_{si} \approx 195$ ($N_e/N_{e0} \approx 9$), respectively. In cases B1, B2 and F1, F2 the shock transition does not produce a coherent structure, but in the density profiles averaged over the y-direction (not shown) the overshoot is located at $x/\lambda_{si} \approx 50$ ($N_e/N_{e0} \approx 6.5$), $x/\lambda_{si} \approx 155$ ($N_e/N_{e0} \approx 7$) and $x/\lambda_{si} \approx 48$ ($N_e/N_{e0} \approx 7$), $x/\lambda_{si} \approx 149$ ($N_e/N_{e0} \approx 6$), respectively, for runs B1, B2 and F1, F2. Downstream of the overshoot the plasma density oscillates around average values that are commensurate with that calculated in Section 5.2.2.

The Weibel-type filamentation instability is the result of interaction between shock-reflected and incoming plasma ions. It leads to the formation of magnetic filaments whose separation

scale is of the order of the ion skin depth, λ_{si} (see Section 3.3). The filaments can be identified in the density distributions (Fig. 6.1) in the shock-ramp region between the overshoot and the shock foot, i.e., for $x/\lambda_{si} \approx (38-50), (38-48)$, and $(36-50)$, for runs B1, F1, and G1, and for $x/\lambda_{si} \approx (155-165), (149-159)$, and $(195-206)$, for runs B2, F2, and G2. The structure and geometry of filaments depend on the configuration of the uniform magnetic field, because it defines the gyration direction of the reflected ions. Figure 6.2 demonstrates that in the case of an in-plane magnetic field ($\varphi = 0^o$, Fig. 6.2a) ions are reflected primarily in the xz plane, which leads to the formation of density filaments along the plasma flow direction that we see in Figure 6.1a1. Analogous conditions occur in the right plasma slab, and similar filamentation structures results (Fig. 6.1a2). For configurations with $\varphi = 45^o$ (Fig. 6.2b1, b2), in addition to negative v_x and v_z components of the reflected ion velocity, there is also v_y velocity component, which is positive in run F1 and negative in run F2, and causes the density filaments to become oblique with the orientation defined by v_y of the reflected ions. Finally, for the out-of-plane configuration ($\varphi = 90^o$, Fig. 6.2c1, c2) the reflected ions are confined to the simulation plane, and again density filaments result that are blurred on account of their large obliquity. Filaments in runs G1 and G2 have opposite inclination, due again to the sign of the v_y velocity component.

As mentioned in Section 4.3.3, for the *in-plane* magnetic field configuration, merging magnetic filaments in the shock ramp can trigger spontaneous turbulent magnetic reconnection, providing an additional channel for electron acceleration. We observe magnetic reconnection for both the in-plane (runs B) and $\varphi = 45^o$ (runs F) magnetic field configurations. The role of magnetic-reconnection-specific acceleration processes are discussed in detail in Section 6.6.

The waves visible in the density distributions in Figure 6.1 upstream of the shock ramp, in the *shock foot* regions ($x/\lambda_{si} \approx (34-38)$ for runs B1 and F1, $x/\lambda_{si} \approx (30-36)$ for run G1, $x/\lambda_{si} \approx (164-169)$ for run B2, $x/\lambda_{si} \approx (158-165)$ for run F2, $x/\lambda_{si} \approx (206-212)$ for run G2), have a different nature and result from the electrostatic Buneman instability caused by the interaction between the shock-reflected ions and inflowing upstream electrons. Their wavelength is much smaller than the ion inertia length, and the wave vector is approximately orthogonal to that of the magnetic filaments (see Section 3.3). The Buneman waves are discussed in detail in Section 6.4.

6.3 Shock self-reformation and rippling

In Section 6.4 shock self-reformation process have been discussed for low, as well as, the high Mach number shocks. The process is caused by non-stationary ion reflection off the shock ramp that at high Mach numbers was shown to be governed by the dynamics of magnetic filaments formed by the Weibel-type instability (Wieland et al., 2016). During reformation the shock velocity and plasma density at the shock are quasi-cyclically modulated around their average values, and the extension of the filamentary region in the shock ramp varies. A bunch of shock-reflected ions streaming against incoming plasma leads to the formation of current
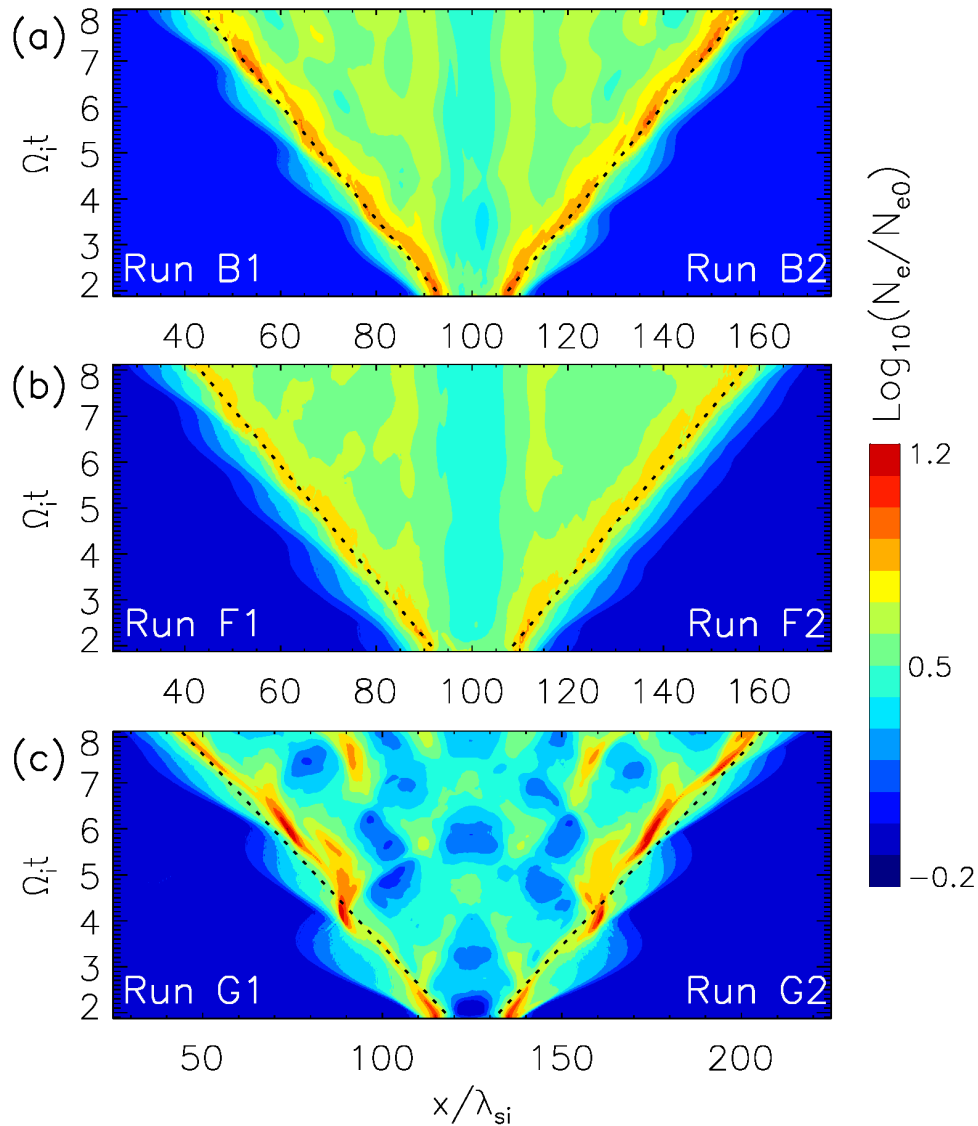

Figure 6.3: Time development of the electron number density averaged over the y-direction for run B (a), run F (b) and run G (c). Color contours present normalized electron density in logarithmic scale. The dashed lines indicate the theoretical shock speed in the simulation frame.

filaments that project along the plasma flow direction and are accompanied in the shock foot by electrostatic Buneman modes. Later in the cycle, once the current filaments start to merge ahead of the shock ramp and become aligned closer to the shock surface on account of bunched ion gyration, the turbulent shock precursor shrinks, and the Buneman modes disappear. This has profound consequences for particle acceleration, as will be discussed in Section 6.5.4.

Figure 6.3 shows for all simulation runs the time evolution of the electron density averaged over the y-direction. The left and right shocks' motion with an average speed $v_{sh,L}$ or $v_{sh,R}$ are marked with dashed lines. Y-axis in Figure 6.3 starts at time $t\Omega_i \approx 2$ when the first reformation cycle begins, and after the shocks have been fully formed. The reformation processes are observed for all magnetic-field orientations and plasma temperatures studied and are most pronounced for out-of-plane (run G) and in-plane (run B) field configurations. The period of self-reformation varies around the average value $1.55\Omega_i^{-1}$ and is consistent with earlier finding of approximately $1.5\Omega_i^{-1}$ obtained for the $\varphi = 45^o$ configuration in Wieland et al. (2016).

The velocities of the *left* and the *right* shock (calculated as an overshoot speed) in the simulation (or downstream) reference frame vary between $0.03c$ and $0.15c$ on account of the shock reformation. The average shock speed equals $0.066c$ for runs B1, B2, $0.067c$ for runs F1, F2 and $0.094c$ for runs G1, G2, very close to the expected speeds of $0.066c$ and $0.1c$,
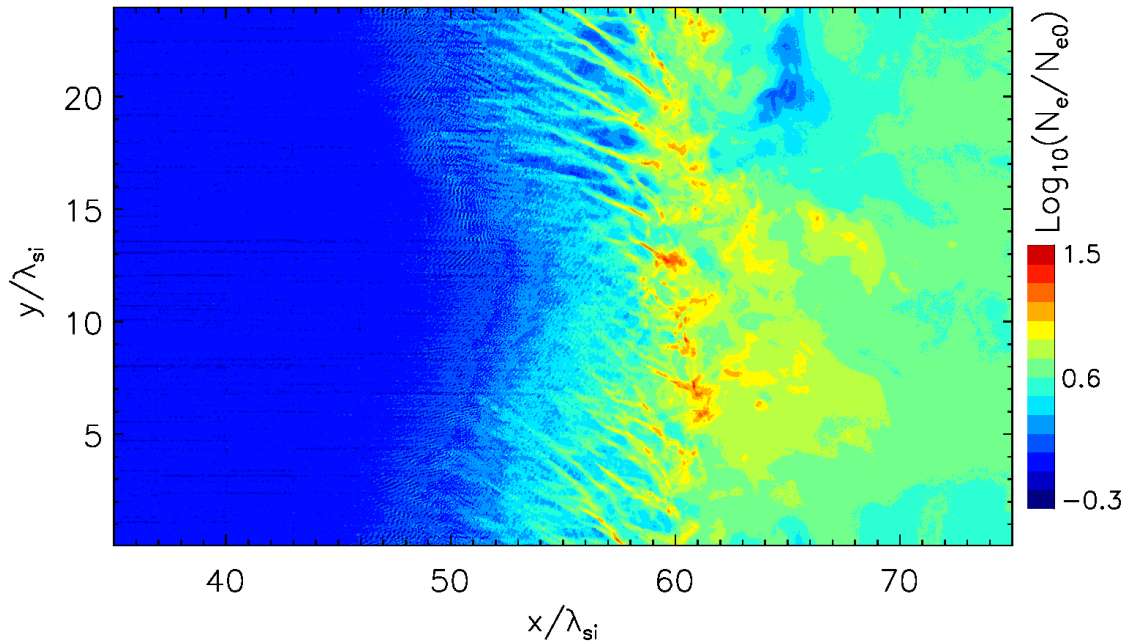

Figure 6.4: Distribution of the normalized electron number density at a shock with visible shock rippling mode for run F1 at time $t\Omega_i = 5.8$.

respectively (see Section 5.2.2).

The shock rippling, caused by spatial modulation of ion reflection, is observed for runs with the in-plane and $\varphi = 45^o$ magnetic field configurations (runs B1, B2, F1 and F2). However, the rippling modes are not fully captured in our simulations due to numerical constraints. Figure 6.4 shows the shock at a stage in which a rippling mode is visible for simulation run F1 at time $t\Omega = 5.8$. The shock front is strongly deformed. The extension of Weibel filaments near the box edges is clearly larger then in the middle of the simulation box around $y \approx 12\lambda_{si}$ where filamentary structures are almost absent. The wavelength of the ripples is about the transverse box size, $\sim 24\lambda_{si}$, which is equal to the upstream ion gyroradius, $\lambda_{gi} = 0.2c/\Omega_i = 4800\Delta = 24\lambda_{si}$. Much larger transverse size of the simulation box would be needed to study shock rippling in detail. Moreover, rippling modes in our simulations are visible only during short time periods, probably because simulation time $t_{runF1} \approx 8\Omega_i^{-1}$ is too small to have these modes fully developed. The simulation by Wieland et al. (2016) traces the shock evolution for long time period of $20\Omega_i^{-1}$ and the rippling mode is observed only for the reverse shock starting from $t\Omega_i > 12$. The transverse box size in their case is sufficient to contain the mode. Thus, in our runs the simulation time and the transverse box size are too small to capture fully-developed rippling modes.

6.4 Structure of the Buneman instability

As discussed above, the Buneman instability results from the interaction of shock-reflected ions with the upstream electrons. It has been shown that this instability can be excited in the foot of high-Mach-number nonrelativistic perpendicular shocks (see Section 3.3). The properties of these electrostatic modes depend on physical parameters such as the shock Mach number, M_A, and the electron plasma beta, β_e. In addition, the instability characteristics may be different in numerical studies with restricted dimensionality. In particular, in 2D simulations the orientation of the large-scale magnetic field with respect to the simulation plane may play a role, as suggested from a comparison of different studies applying the out-of-plane magnetic field (Matsumoto et al., 2012, 2013), the $\varphi = 45^o$ configuration (Wieland et al., 2016), and the in-plane field (Kato & Takabe, 2010b; Matsumoto et al., 2015). However, all these works investigate shocks propagating in plasmas with different specific physical parameters. In contrast, our present study is focused on a direct comparison of the Buneman instability properties in simulation runs in which the main variable parameter is the magnetic field orientation.
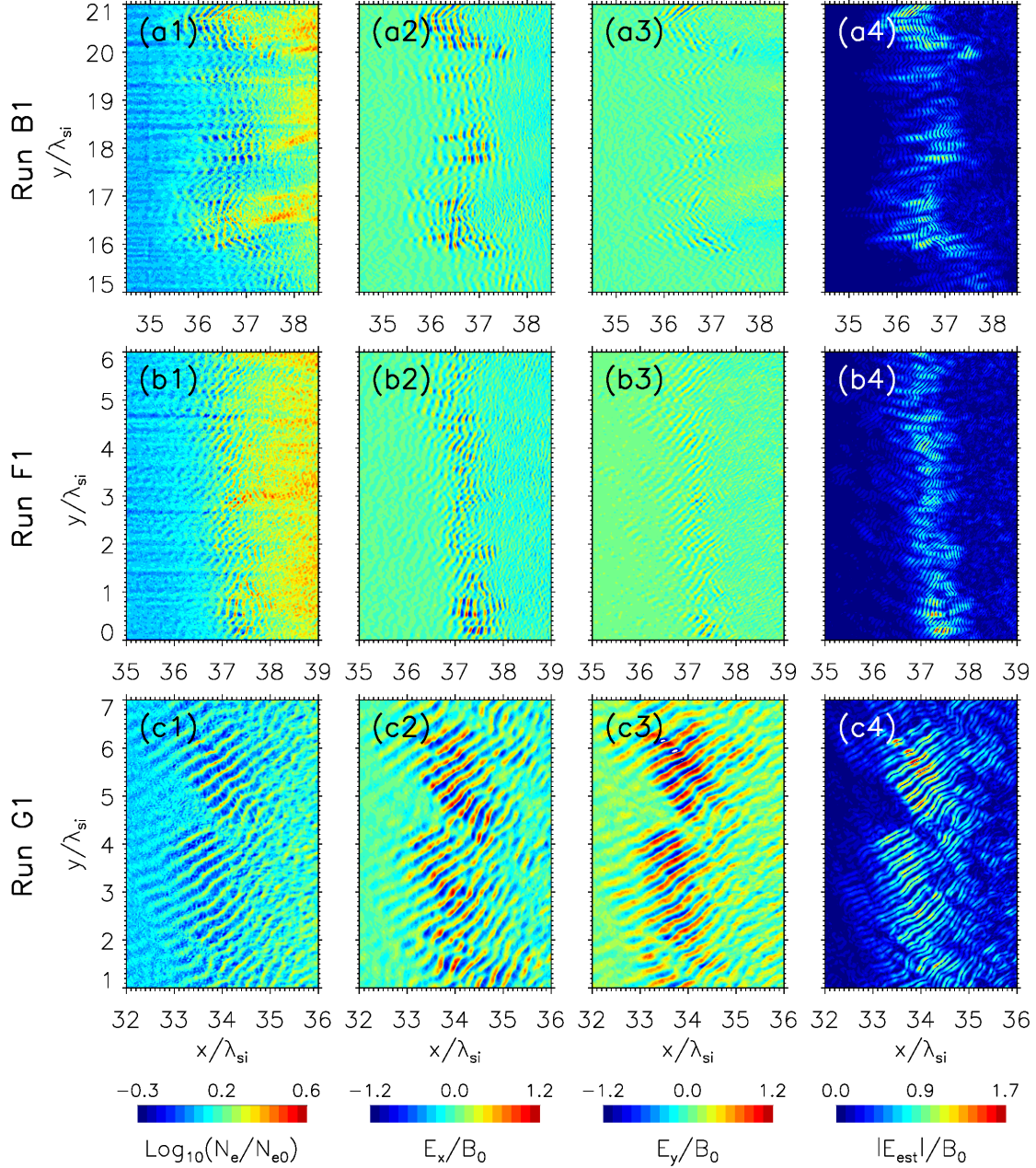
Figure 6.5: Electron density maps (a1,b1,c1), x component of electric field (a2,b2,c2), y component of electric field (a3,b3,c3) and electrostatic field strength (a4,b4,c4) in zoomed-up regions taken from Figures 6.1a1, a2, a3 with the most intense Buneman mode for runs B1 (a* panels), F1 (b*) and G1 (c*). Density is presented in logarithmic scale and normalized to the upstream density. Electric field and electrostatic field strengths are normalized to the upstream magnetic field.

Our discussion in this section is based on results obtained for the *left* shocks. Figure 6.5 presents a blow-up of a portion of the *left* shock foot shown in Figures 6.1a1, a2 and a3. From left to right, displayed are the electron density, the E_x component of the electric field, the E_y component of the electric field, and the electrostatic field amplitude, from top to bottom

78

for runs B1, F1, and G1. The electrostatic field amplitude is calculated as $|E_{est}| = |-\nabla\phi|$, where ϕ is the electric potential derived directly from the charge distribution. The modes in the electrostatic field maps in Figures 6.5a4-6.5c4 appear to have half their true wavelength, because the absolute values of $\nabla\phi$ are plotted, and one cannot distinguish between positive and negative field strengths. The wave structures visible in the plot occur at scales much smaller than the ion inertia scale. The form of the waves depends on the magnetic-field configuration. For the out-of-plane field orientation (run G1, Fig. 6.5c) coherent wave trains are formed over an extended region of the shock foot with the width $\sim 2.5\lambda_{si}$ (see, e.g., Matsumoto et al., 2012). The electrostatic field reaches amplitudes of $|E_{est}|/B_0 \sim 2$, and therefore the trapping condition (Eq. 4.13) is easily satisfied. Wave coherence is broken for the in-plane configuration (run B1, Fig. 6.5a), and the modes are distributed in patchy structures formed in narrow regions ahead of the magnetic filaments from the Weibel instability region. In the $\varphi = 45^o$ case, the electrostatic waves have a structure which is intermediate between these forms – the wave structure is largely coherent but over a narrow region with thickness $\sim \lambda_{si}$. For both B1 and F1, the amplitude of the electrostatic field reachs $|E_{est}|/B_0 \sim 1.7$ at peak locations, but the average field strength is $|E_{est}|/B_0 \sim 1$ or even less.

The main difference in the structure of the Buneman wave region observed for runs B/F and G comes from the level of the homogeneity of reflected ion beam, which in turn depends on the structure of the overshoot. Ion reflection in the out-of-plane case is mostly uniform along the shock surface because the shock overshoot has a largely coherent structure. The overshoot region in the in-plane and $\varphi = 45^o$ cases shows clumped structures (see Fig. 6.1) producing an incoherent flow of reflected ions.

As noted in Section 6.3, the intensity of the electrostatic waves varies considerably during a shock reformation cycle due to the changing number of shock-reflected ions. The average value of the electrostatic field amplitude varies in the range $|E_{est}|/B_0 \sim 0.1 - 1.1$ for run B1, $0.3 - 1.1$ for run F1, and $0.3 - 1.5$ for run G1. Note also that for the right shocks in moderate-temperature plasma, $\beta_e = 0.5$, the maximum intensity of the Buneman waves is $20\% - 50\%$ smaller than in the cold plasma. However, the area of the region occupied by electrostatic waves is $20\% - 30\%$ larger in the case of the warm plasma. We do not expect a thermal reduction in the Buneman instability growth rate that would explain the lower wave intensity for $\beta_e = 0.5$, and we cannot exclude that the saturation level is lower on account of strong nonlinear Landau damping (Breizman & Riutov, 1974) or the modulation instability (Galeev, Sagdeev, Shapiro,
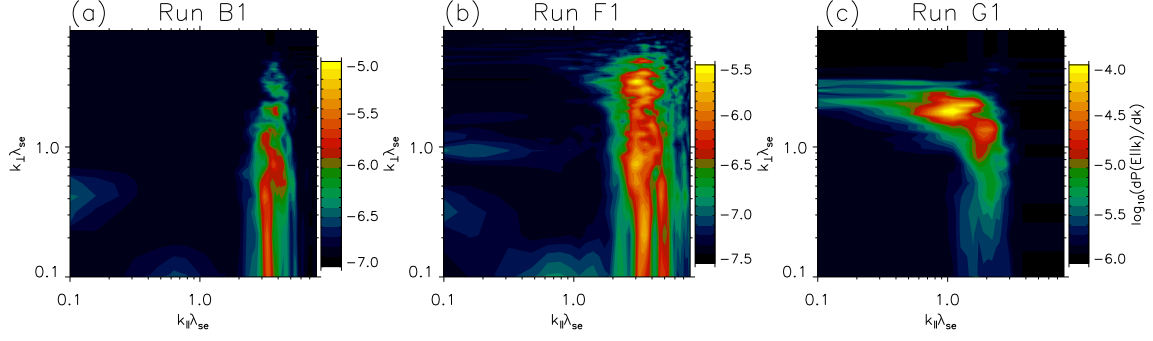
Figure 6.6: Fourier power spectrum of the electric field parallel to the wave vector, $\vec{e}_k \cdot \vec{E}$, for the regions presented in the panels a1 (a), b1 (b) and c1 (c) of Fig. 6.5.

& Shevchenko, 1977). The efficiency of electron acceleration is determined by the number of trapped electrons and the volume fraction occupied by intense Buneman modes with the convective electric field that provides the acceleration. A conjunction of these factors, though different in each case analyzed here, permit efficient electron acceleration at both the low- and moderate-β_e shocks as will be shown later.

As discussed in Section 3.3, the Buneman waves are excited in the shock foot when Equations 3.24 and 3.25 are satisfied. The observed electric field modes have a wave vector

$$k = \frac{c}{\Delta v} \frac{1}{\lambda_{se}} \ . \tag{6.1}$$

The beam of reflected ions is warm, and we expect the electrostatic instability to operate in the kinetic regime and the wave vector of the peak intensity to be aligned with the streaming velocity (Tidman & Krall, 1971). Figure 6.6 displays Fourier power spectra of the electric field parallel to the wave vector, $\vec{e}_k \cdot \vec{E}$, calculated in the regions shown in Figure 6.5. The mean field values and linear gradients were removed from the E_x and E_y maps for this analysis because wave vectors with low-k values are not important for the consideration of the Buneman modes. Corresponding ion and electron phase-space distributions in $v_x - v_y$ are shown in Figure 6.7. For run B1 we see a narrow signal at $k_{\parallel}\lambda_{se} \simeq 3.3$ in the range $k_{\perp}\lambda_{se} \lesssim 0.7$ (Fig. 6.6a), that corresponds to $k \simeq 3.3\lambda_{se}^{-1}$ and $\Delta v \simeq 0.3c$. Noting that the plasma motion in this case (B1) is primarily along the x-direction and calculating averaged velocity components we obtain $v_{xi} \simeq -0.15c$ and $v_{xe} \simeq 0.17c$ for reflected ions and incoming electrons, respectively (compare Fig. 6.7a). The relative velocity is thus $\Delta v \simeq 0.31c$, which is in good agreement with the value calculated from the Fourier spectrum (Fig. 6.6a). Therefore, the electrostatic modes in the shock foot can be identified with the Buneman waves.
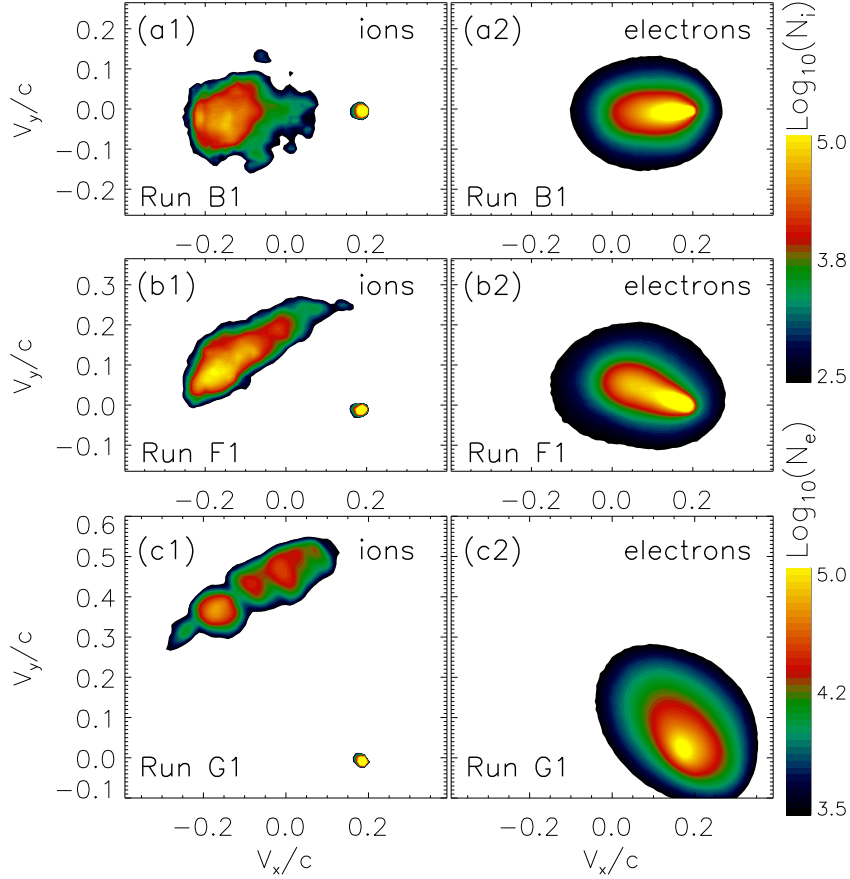
Figure 6.7: Phase-space distribution in $v_x - v_y$ of ions (first column) and electrons (second column) in the regions presented in Fig. 6.5 for runs B1 (a1, a2), F1 (b1, b2) and G1 (c1, c2). The scale is logarithmic.

For the simulation with $\varphi = 45^o$ (run F1) we see the mode out to $k_\perp \lambda_{se} \simeq 4$. The phase-space plot (Fig. 6.7b) suggests that the parallel mode should be observed between $\vec{k}\lambda_{se} \simeq (3;0)$ and $\vec{k}\lambda_{se} \simeq (2.5;3)$, which is again in approximate agreement with the range of wave vector for which the Fourier analysis indicates a high intensity of $\vec{e}_k \cdot \vec{E}$ waves modes.

For the out-of-plane magnetic field configuration (run G1) the velocity range of reflected ions inserted in Equation 6.1 implies a strong growth between $\vec{k}\lambda_{se} \simeq (1.4;1.4)$ and $\vec{k}\lambda_{se} \simeq (0.75;2)$, exactly where we observe it in the Fourier spectra. The Fourier power spectra also indicate wave intensity at wave vectors not aligned with the streaming velocity of reflected ions. Figure 6.5c2 suggests that at least part of that arises from localized reorientation of the wave fronts in E_x, probably caused by modulation through large-scale modes.

The high electrostatic field amplitudes in run G1 are somewhat surprising, because there are fewer reflected ions in this run compared to the simulations with $\varphi = 0^o$ and $\varphi = 45^o$. The reflected ion fraction is $\chi = 0.29$ for run B1, $\chi = 0.41$ for run F1, and $\chi = 0.19$ for run G1. Amano and Hoshino (2009b) modified an estimate by Ishihara et al. (1980) for the transferrable

energy density,

$$\varepsilon_0 \frac{E^2}{2} \simeq \frac{3 N_e m_e \Delta v^2}{8} \left(\frac{m_e}{m_i}\right)^{1/3}, \tag{6.2}$$

and we find fairly good agreement with the energy density seen in our simulation ($\sim 70\%$), provided that we use the component of Δv that lies in the simulation plane (and is indicated in Fig. 6.7). Only for run G1 (or $\varphi = 90^o$) we find the trajectories of reflected ions fully contained in the simulation plane, and so part of the streaming motion in runs B1 and F1 cannot excite the Buneman instability, because $\vec{k}$ must lie in the simulation plane and $\vec{k} \parallel \Delta \vec{v}$. We conclude that the out-of-plane configuration is best suited to fully capture the development of the Buneman waves in a 2D3V simulation, although the adiabatic index is modified in that case with respect to Γ_p in the 3D system. Equation 4.13 applies in that case, and the velocity difference between the electrons and the reflected ions is $\Delta \vec{v} \simeq 2^{-0.5} \Delta v (1,1,0)$. If the large-scale magnetic field is not strictly out-of-plane, but stands at an angle $\varphi < 90^o$ to the simulation plane, then the relative motion is partially rotated out of the simulation plane, and

$$\Delta \vec{v} \simeq 2^{-0.5} \Delta v (1, \sin \varphi, \cos \varphi). \tag{6.3}$$

The z-component of the ion motion cannot drive Buneman waves, and so we need a larger shock speed to drive the electrostatic waves with the strong enough intensity for electron trapping during a sufficiently long time to accelerate electrons up to nonthermal energies by convective electric field. We therefore suggest that formula 4.13 for the trapping condition be modified to

$$M_A \geq \sqrt{\frac{2}{1 + \sin^2 \varphi} (1 + \chi)} \left(\frac{m_i}{m_e}\right)^{\frac{2}{3}}. \tag{6.4}$$

Inserting numbers, including the reflection rates measured in regions presented in Figure 6.5, we find that in run B1 we would need $M_A \simeq 39$, and $M_A \simeq 36$ in run F1, for efficient trapping. Both simulations are set up with $M_A = 31.7$, and so the energy of streaming in the simulation plane seems to be insufficient to drive very strong Buneman modes and thus efficient SSA. Likewise, the trapping condition (Eq. 6.4) would be strongly violated in the $\varphi = 0^o$ simulations presented by Matsumoto et al. (2015), and indeed no significant SSA was reported.

Applying a similar modification to the driving condition (Eq. 3.25) leads to the expression

$$M_s \gtrsim \frac{1 + \chi}{\sqrt{2(1 + \sin^2 \varphi)}} \sqrt{\frac{m_i}{m_e}} \sqrt{\frac{T_e}{T_i}}. \tag{6.5}$$

We also note that the restriction of Buneman waves with k_z component to the *x-y* plane changes the orientation of the potential wells in which electrons can be trapped. SSA arises from motional electric field that accelerates electrons along the electrostatic equipotential surface of the waves, and a geometrical restriction of $\vec{k}$ will also modify the relevant component of the motional electric field, $\vec{E} \perp \vec{k}$. However, we conclude that the dominant effects in our simulations appear to be the reduction in the saturation amplitude and the area occupied by the Buneman waves.

The properties of the Buneman instability region in the foot of the *right* shocks propagating into the warm plasma, $\beta_e = 0.5$, are similar to those described above for the low-β_e *left* shocks, $\beta_e = 5 \cdot 10^{-4}$. In both cases, the shock reformation imposes cyclic changes to the appearance of the electrostatic-field variations in the shock foot. Here we summarize general features and differences of Buneman wave fields in the foot regions of the *left* and *right* shocks. In all runs the Buneman modes evolve kinetically and are largely, but not perfectly, parallel to the streaming velocity of reflected ions. The Buneman *k*-modes depend on the streaming direction of reflected ions, which is defined by the orientation of the large-scale magnetic field in 2D simulations. The Buneman modes are approximately parallel to the shock normal for the in-plane magnetic field (runs B). They turn oblique for $\varphi = 45^o$ (runs F), and are highly oblique for the out-of-plane magnetic-field configuration (runs G). In all six runs the wavelengths of Buneman waves are commensurate with the streaming speed difference between reflected ions and upstream electrons, and hence they are smaller for runs B/F in comparison with runs G. The region with high-intensity coherent waves is larger and considerably less patchy for the out-of-plane configuration (runs G) than it is for an inclined or in-plane magnetic field (runs B and F), irrespective of the plasma β_e. In moderate-temperature plasma (runs *2) the peak strength of the electrostatic Buneman waves is less than that in the cold plasma (runs *1), but the surface area of the unstable region is larger in that case.

6.5 Electron acceleration

The parameters in our simulations should provide suitable conditions for electron acceleration up to nonthermal energies. As known from earlier studies of high-Mach-number shocks, the electron injection at such shocks is at least a two-stage process that starts with the SSA in the shock foot and then is followed by additional particle energization processes in the shock ramp and around the overshoot (see Section 4.3). In this section we describe the electron pre-

acceleration at a perpendicular shock. Our two-dimensional numerical experiments with various configurations of the large-scale magnetic field with respect to the simulation plane allow us to observe the injection processes from different perspectives. This in turn enables us to draw conclusions on the nature of electron pre-acceleration and its true efficiency in a fully three-dimensional system.

We start our discussion in Section 6.5.1 with a description of the SSA process in the shock foot containing the electrostatic Buneman waves. The analysis is based on results of the *left* shocks propagating in cold plasmas with low $\beta_e = 5 \cdot 10^{-4}$ (runs B1, F1, G1). As noted in Section 6.1 and discussed in Section 6.4, these shocks provide conditions for strongly nonlinear Buneman modes in the shock foot. Subsequent processes of further electron energization at the shock front are described for shocks in plasmas with a moderate plasma beta (runs B2, F2, G2), at which the injection is more efficient than in the cold plasmas, as we show. The analysis here is presented only for cases of the out-of-plane (run G2, Sec. 6.5.2) and the in-plane (run B2, Sec. 6.5.3) magnetic-field configurations, since electron acceleration processes observed in runs B ($\varphi = 0^o$) are essentially the same as in the $\varphi = 45^o$ case (runs F).

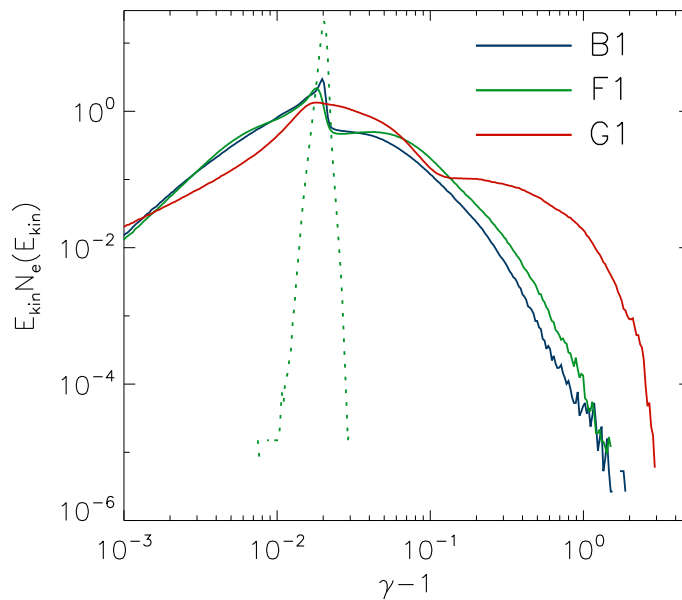### 6.5.1 Shock surfing acceleration

Figure 6.8: Kinetic-energy spectra of electrons in the region harboring Buneman waves as presented in Figure 6.5 for run B1 (blue), run F1 (green) and run G1 (red). The dotted green line indicates the spectrum of upstream cold plasma electrons (extracted from run F1).

Figure 6.8 shows kinetic-energy spectra of electrons residing in the Buneman instability

regions in the shock-foot locations depicted in Figure 6.5. For all magnetic-field configurations supra-thermal spectral tails are produced by SSA. However, the high-energy portion of the electron spectrum for run G1 contains a significantly larger number of particles than is found for runs B1 and F1. Specifically, there are about 2200, 7600 and 3.4×10^6 electrons with $\gamma > 1.5$ for runs B1, F1, and G1, respectively. These spectral differences can be explained by the amplitude and filling factor of the Buneman waves in the shock foot, as discussed in Section 6.4. In runs B1 and F1, the wave zone is narrow, and their amplitude can barely trap relativistic electrons. On the other hand, in run G1, the area occupied by the Buneman waves is almost three times larger than in runs B1 and F1, and in addition electrostatic waves are more intense and coherent. We find that many electrons in run G1 approaching the foot from the far upstream have interacted with electrostatic waves twice or even three times before being advected toward the shock. This multiple SSA processes enable the particles to achieve energies up to $\gamma \sim 4$ (Matsumoto et al., 2012) before further energization in the shock ramp.

The number of computational cells occupied by high-intensity Buneman waves strongly vary because of the shock self-reformation. We found a clear correlation between the number of pre-accelerated electrons and the occurrence of intense electrostatic field. Figure 6.9 displays for run B1 the temporal development of the number of electrons with Lorentz factor $\gamma > 1.5$ and the number of computational cells with electrostatic field strength commensurate with or stronger than the initial homogeneous magnetic field. A Spearman rank test (see, e.g., Kendall, 1970) yields correlation coefficients in the range $0.7 - 0.9$ for all six simulation runs with very small p-values, indicating a good correlation.
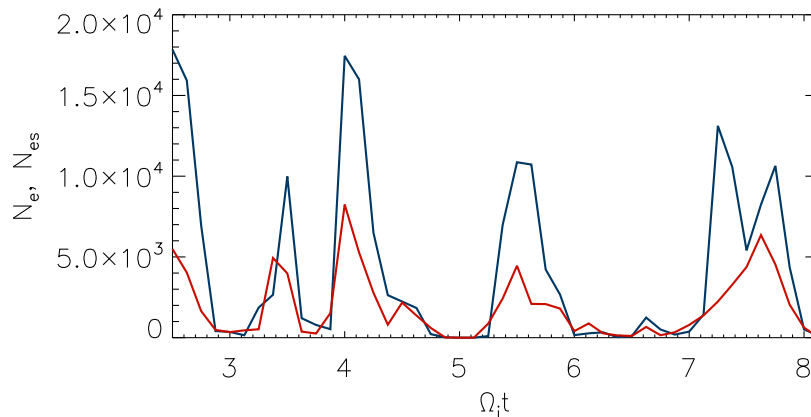

Figure 6.9: Temporal profiles of the number of energetic electrons, $N_e(\gamma > 1.5)$ (blue line), in comparison to the abundance of strong electrostatic field, $N_{es}(E_{es} > 0.5 B_0)$ (red line). The Spearman rank correlation coefficient is 0.9 with a p-value of $4 \cdot 10^{-17}$. The figure applies to the region harboring Buneman waves in run B1.
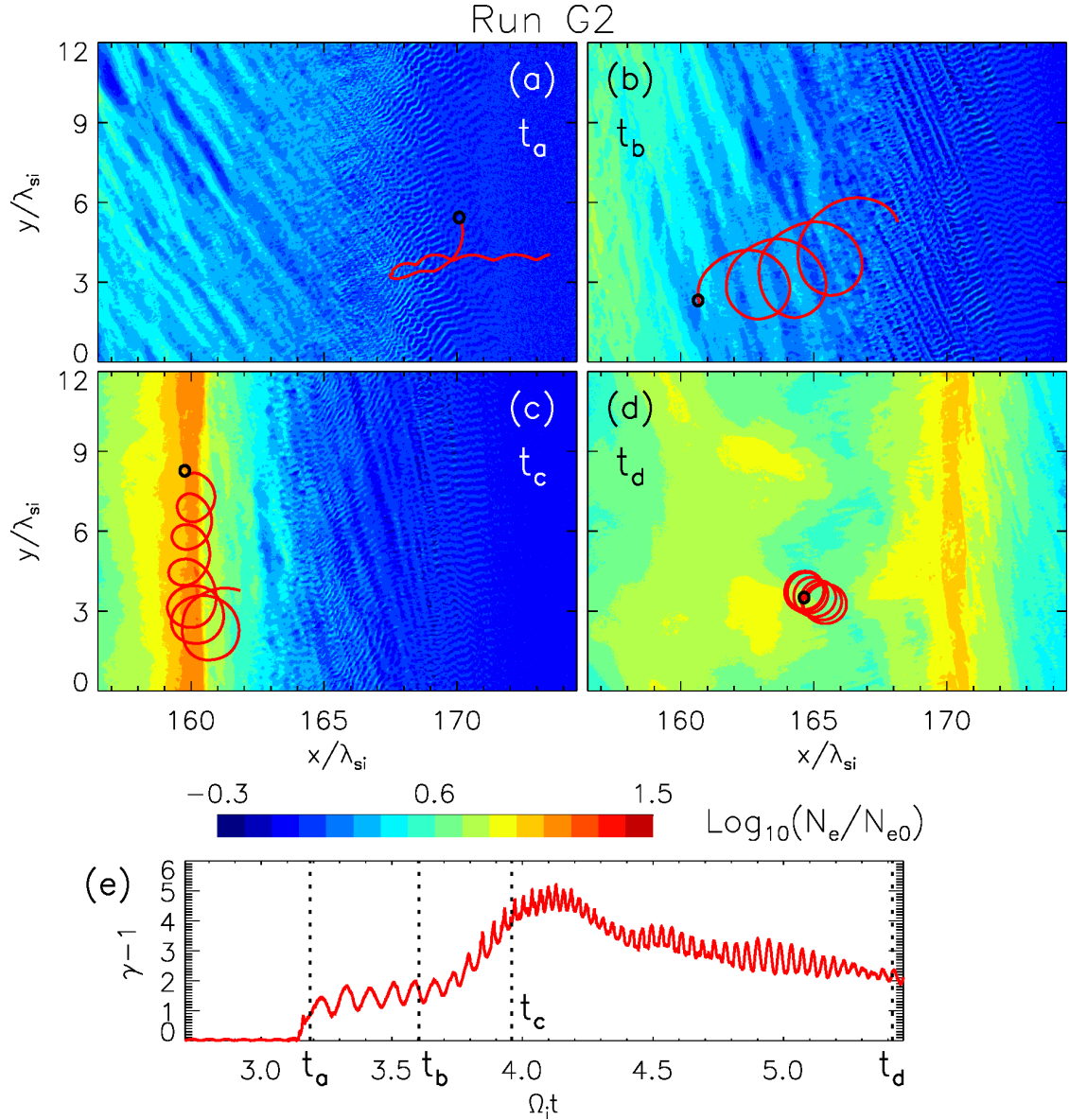
Figure 6.10: Trajectory segments of a high-energy electron from run G2 superposed on the electron density map at four time intervals. The panels (a), (b), (c), and (d) display the state of the system at the times t_a (a), t_b (b), t_c (c) and t_d (d) that are marked in panel (e), and the black circles indicate the position of the electron at these moments. The red lines give their trajectory history for the time span $0.3\Omega_i^{-1}$. In panel (e) we present the temporal development of the kinetic energy of the electron.

6.5.2 Electron acceleration, 90° configuration

The main stages of electron acceleration for the out-of-plane magnetic-field configuration (run G2) are shown in Figure 6.10, in which we trace the trajectory and the energy evolution of a typical particle that becomes energized at the shock. At time t_a the electron resides in the Buneman-wave region and is accelerated via SSA process, through which its energy reaches $\gamma \simeq 2.5$ (Fig. 6.10). In this example, the electron does not experience another SSA cycle but

86

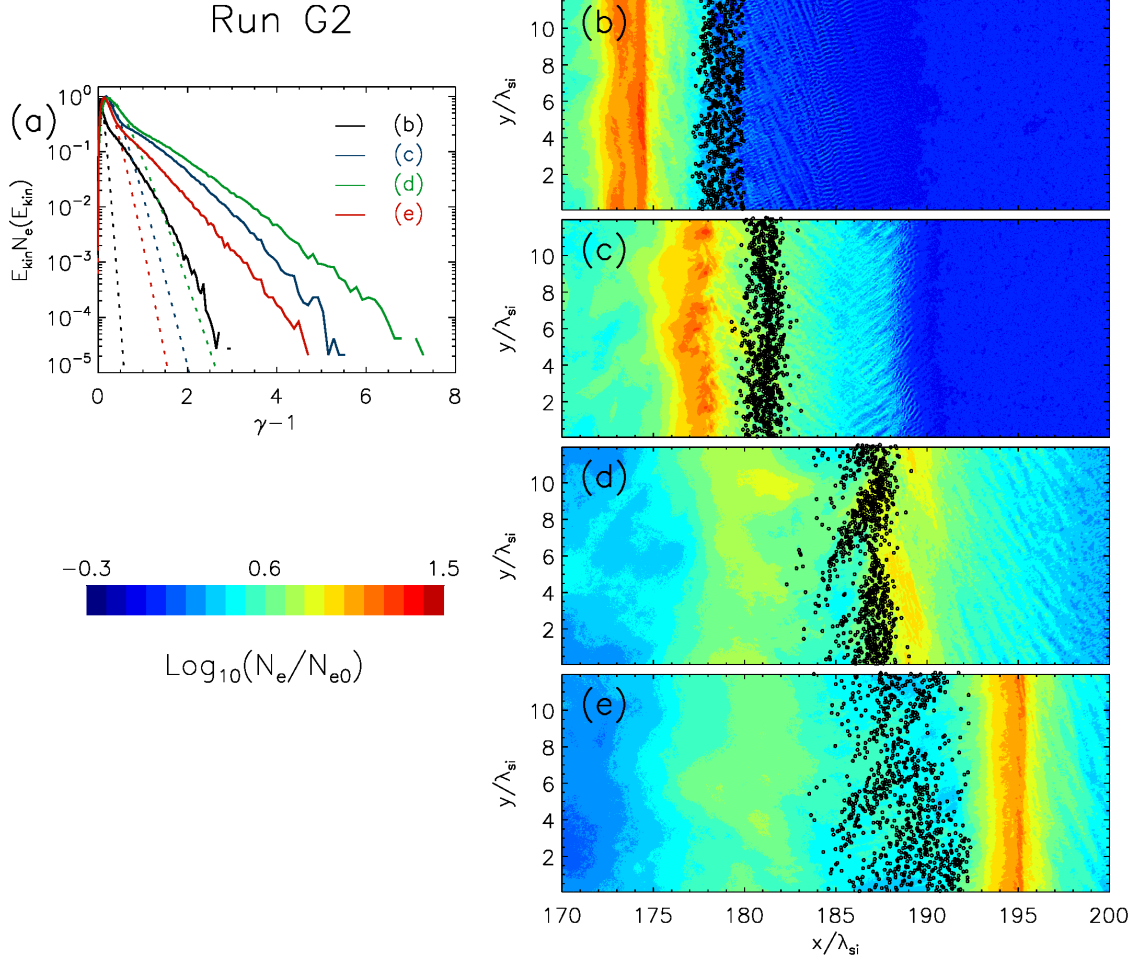Figure 6.11: Panel (a): Spectral evolution of electrons extracted from the downstream region for run G2 compared to fits of a relativistic Maxwellian plotted as dotted lines. Panels (b), (c), (d) and (e) present density maps of the shock region together with the positions of electrons selected in the upstream region. The panels display the status at time $t = 5.625\Omega^{-1}$, $6.25\Omega^{-1}$, $7\Omega^{-1}$, $7.375\Omega^{-1}$, respectively.

starts to gyrate around the mean magnetic field and passes through the shock ramp towards the overshoot. The projection of its gyromotion on the convective electric field in the shock ramp, that is in the y-direction, imposes quasi-sinusoidal variations in the electron kinetic energy. A significant energy increase arises only beyond time t_b when the electron approaches the overshoot region. The highest energy of $\gamma \simeq 6$ is reached around the time of highest compression in the overshoot, shortly after t_c. Then the electron enters the downstream region, in which the plasma compression is much smaller than in the overshoot ($N_{down} \sim 3N_0$ in the downstream and $N_{over} \sim 10N_0$ in the overshoot), the energy of the electron slowly decreases. The acceleration beyond the SSA phase is thus largely adiabatic. In fact, after time $t = t_a$, the average value of the magnetic moment of the electron remains constant (compare Matsumoto et al., 2012, 2013).

To examine the dynamics of the acceleration processes, we follow the temporal evolution of the spectrum for a selected portion of upstream electrons traveling through the shock transition. Figure 6.11a displays electron spectra at four points in time, and the panels b-e indicate the location of the particles for each of the four instances. Each spectrum is fitted with a relativistic Maxwellian (dashed lines in Fig. 6.11a). The relativistic Maxwell distribution is defined by the formula (Jüttner, 1911):

$$f(E_{kin}) \propto (E_{kin} + m_e c^2) \sqrt{E_{kin}(E_{kin} + 2 * m_e c^2)} \exp\left(-E_{kin}/k_B T\right) . \qquad (6.6)$$

The relativistic Maxwellian defines the thermal population of electrons in the calculated spectra. We define the non-thermal electron fraction (NTEF) by subtracting the thermal population from the spectrum of high-energy electrons. A supra-thermal tail is evident in the spectra already after passage though the Buneman wave field at the shock foot (Fig. 6.11b). During their further transport through the shock the electrons are accelerated to very high energies, and at the same time their bulk temperature increases. The nonthermal electron fraction is about $4.8 \pm 0.2\%$, carrying $\sim 26\%$ of the total electron energy. It remains roughly constant once the particles pass through the overshoot and propagate toward the downstream region, where the bulk temperature decreases and the spectral tails become less prominent than those at the overshoot. This behavior provides general support for the expectation that the acceleration beyond the SSA phase is adiabatic, that we have demonstrated for a single particle above. Particle heating is thus achieved through bulk plasma compression in the shock that is strongest at the overshoot.

6.5.3 Electron acceleration, 0° and 45° configurations

Electron acceleration for the case with the in-plane magnetic-field configuration (run B2) has been analysed in a similar way as that for the out-of-plane field (Sec. 6.5.2). Figure 6.12 follows the trajectory and the kinetic-energy history of a typical particle acquiring high energy in interactions within the shock structures, and Figure 6.13 displays spectra of a selected electron population traversing the shock. To be noted from the figures is that for the in-plane magnetic field the SSA process in the shock foot results in moderate particle energization. The Lorentz factor of the electron increases only to $\gamma \simeq 1.5$ while it resides in the Buneman zone at the shock foot (time t_a in Fig. 6.12a), and the supra-thermal tail in the spectrum in Figure 6.13a does not reach $\gamma = 2$. Subsequent acceleration (Figs. 6.12b-d) in the shock structure strongly differs from
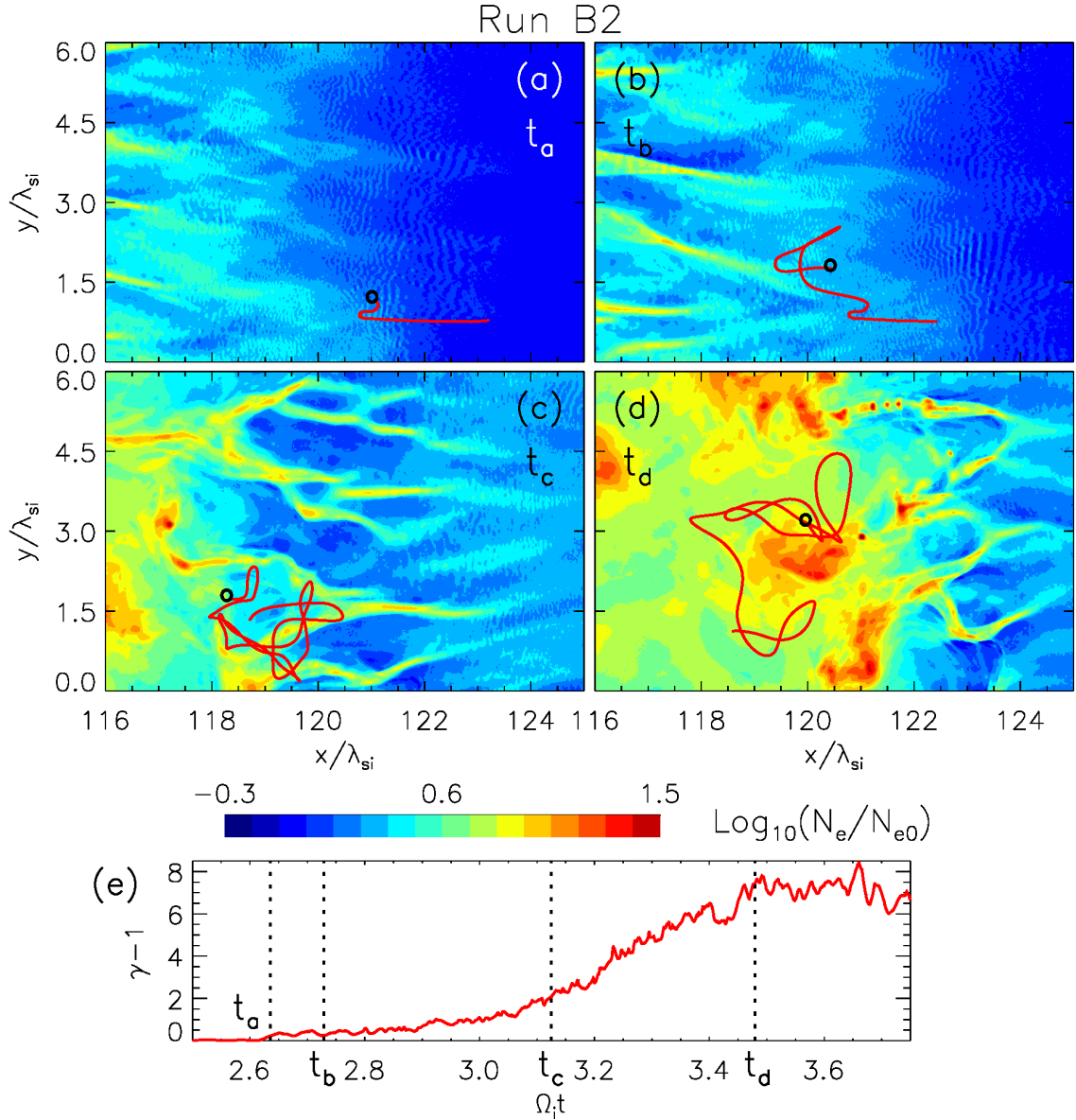
Figure 6.12: Trajectory segments of a high-energy electron from run B2 superposed on an electron-density map at four time intervals. In panel (e) we present the temporal development of the kinetic energy of the electron and mark four points in time. The panels (a), (b), (c), and (d) display the state of the system at these times (t_a (a), t_b (b), t_c (c) and t_d (d)), and the black circles indicate the position of the electron at these moments. The red lines give their trajectory history for the time span $0.2\Omega_i^{-1}$.

that observed in the case with the out-of-plane magnetic field: the particle randomly interacts with moving magnetic structures, essentially undergoing a stochastic (the second-order Fermi) acceleration processes. Its energy increases steadily, and the rate of the energy gain is larger in the shock overshoot region (between times t_c and t_d in Fig. 6.12e) than in the shock ramp (time range approximately from t_b to t_c in Fig. 6.12e), due to stronger turbulent magnetic field at the overshoot. In the end, the sample electron reaches a maximum energy of about $\gamma \simeq 9$
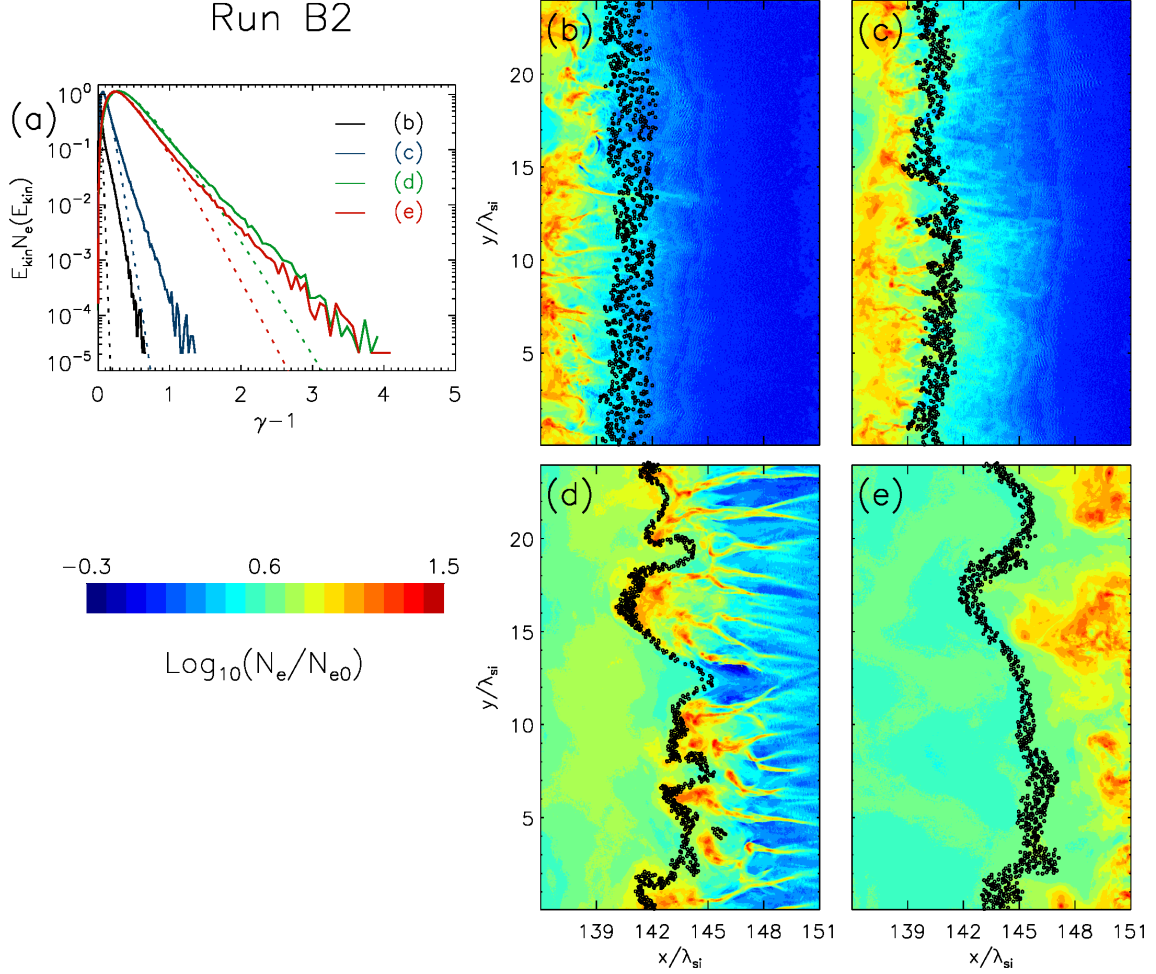
Figure 6.13: The top panel (a) displays the spectral evolution of electrons selected in the downstream region for run B2. The dotted lines indicate adaptions of a relativistic Maxwellian. Panels (b), (c), (d) and (e) present density maps of the shock region and the positions of the selected electrons at the time $t = 5.75\Omega^{-1}, 5.875\Omega^{-1}, 6.625\Omega^{-1}, 7.375\Omega^{-1}$.

and retains that energy while it is advected into the downstream region of the shock. Electron injection for the in-plane ($\varphi = 0^o$) and the $\varphi = 45^o$ magnetic field configurations thus mainly involve irreversible non-adiabatic acceleration processes.

The observation of non-adiabatic acceleration is supported with an analysis of the electron spectra in Figure 6.13 that remain largely unchanged once particles reach their maximum energies and are transmitted downstream (Figs. 6.13d-e). Small differences in these spectra may result in part from the plasma decompression behind the overshoot, but most probably they reflect the shock reformation. Note, that scattering of energetic particles is accompanied with significant bulk particle heating. As a result, the fraction of nonthermal electrons in the downstream spectrum is about an order of magnitude less than that obtained in the $\varphi = 90^o$ case. The spectra also decay at smaller energies, compared with the case of run G2.

There is some uncertainty in the fraction of nonthermal electrons, because during the shock transition the particles disperse, and so electrons initially confined in a narrow range of x coordinates are distributed over an x-range of 10 λ_{si} once they are in the downstream region, in particular for run G2 ($\varphi = 90^o$). The nonthermal fractions are calculated using the Maxwellian fits to the low-energy spectra that are presented in Figures 6.11a and 6.13a. We find 8.6%, 6.4%, 5.9%, 4.8% for the snapshots (b), (c), (d), (e) in Figure 6.11a, i.e., the out-of-plane configuration, whereas for run B and an in-plane magnetic field we obtain 0.67%, 0.21%, 0.31%, 0.41% (for snapshots (b), (c), (d), (e) in Figure 6.13a). The increase in NTEF between the shock ramp, the overshoot, and the downstream region of the simulation with the in-plane configuration (run B) reflects the non-adiabatic acceleration processes that appear to operate near the overshoot. In contrast, very efficient acceleration by SSA is observed in the shock foot for out-of-plane magnetic field, and in the shock ramp and at the overshoot we loose nonthermal energy by randomization and heating.

The shocks in the F runs (for $\varphi = 45^o$) essentially behave like those in the simulations with the in-plane magnetic field (B runs), and so discussion of this subsection also applies to the shocks in runs F.

6.5.4 Influence of shock reformation processes

In Sections 6.3, 6.4 and 6.5.1 we discussed the significant influence of the cyclic self-reformation on the structure and speed of the shock, the intensity of Buneman waves, and subsequently on particle acceleration. Another consequence is that the downstream particle distributions are not uniform, and the choice of downstream region from which we extract particle spectra.

In the downstream, even small regions of size $0.5\lambda_{si} \times 0.5\lambda_{si}$ contain a large number of computational particles (on average 2×10^5 for runs B2/F2 and 1.5×10^5 for run G2). Hence, *local* electron spectra can be calculated with reasonable precision. The *local* temperature can be evaluated by fitting a relativistic Maxwellian so that NTEF can be determined. Figure 6.14 shows maps of the electron density and nonthermal electron fraction in the downstream region of the shocks in runs B1 and B2. To be noted from the figure is the inhomogeneous structures of the downstream regions that results from shock reformation. Regions of higher density are signatures of the reformation phases at which the shock overshoot had the highest density. The nonthermal electron fraction is also nonuniform (Fig. 6.14b). The simulation is too short to permit homogenization of the downstream region, implying that it will be achieved only very
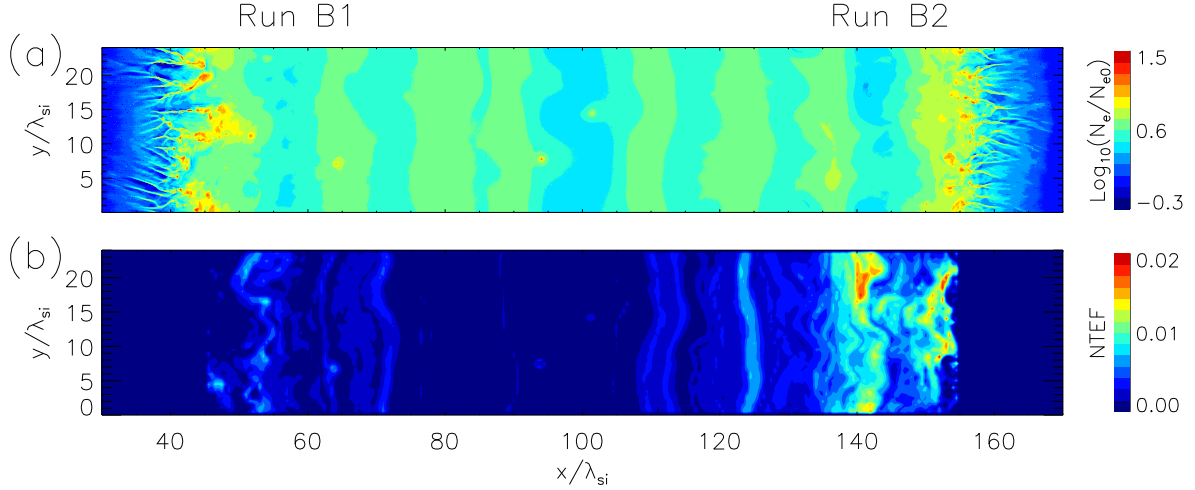
Figure 6.14: Normalized electron density in logarithmic scale (a) and NTEF (b) for runs B, time step $8.125\Omega_i^{-1}$.

far downstream.

Figure 6.15 displays profiles of the nonthermal electron fraction for all simulation runs at two time steps: $8.125\Omega_i^{-1}$ (red line) and $5.625\Omega_i^{-1}$ (blue line). Large variations of NTEF downstream of the shocks are evident. They reflect variations in both the bulk temperature and the number of high-energy electron. Figure 6.15a presents profiles (averaged over *y*-direction) of the nonthermal electron fraction in runs B1 and B2. For the red line, one can see three maxima in the left part of the panel (run B1, region $x/\lambda_{si} = 45 - 100$) around $x/\lambda_{si} \simeq 53$, 71, and 88, and four maxima in the right part of the panel (run B2, region $x/\lambda_{si} = 100 - 155$) around $x/\lambda_{si} \simeq 112$, 124, 141, and 152. These maxima trace back to passage through the most intense electrostatic-wave field in the shock foot. The blue line displays the nonthermal fraction at an earlier time ($t = 5.625\Omega_i$). We note that the nonthermal fraction at a fixed location was higher at earlier times, indicating a decrease with time of the abundance of pre-accelerated electrons in the downstream region. We observe the same trend for runs F, which may explain the marginal nonthermal population found in the far-downstream region in the simulation of Wieland et al. (2016). It is remarkable that we do not observe a similar loss of nonthermal electrons in the simulation with the out-of-plane magnetic field (Fig. 6.14c). In this case the amplitude of variations in electron density is also larger and somewhat correlated, which suggests that homogenization is not as efficient as for runs B and F.

Both Figures 6.14 and 6.15 clearly show that NTEF is on average twice larger downstream of the shocks propagating in the warm plasma. Thus the electron acceleration efficiency for shocks in plasmas with $\beta_e = 0.5$ is higher than for shocks in cold plasma.
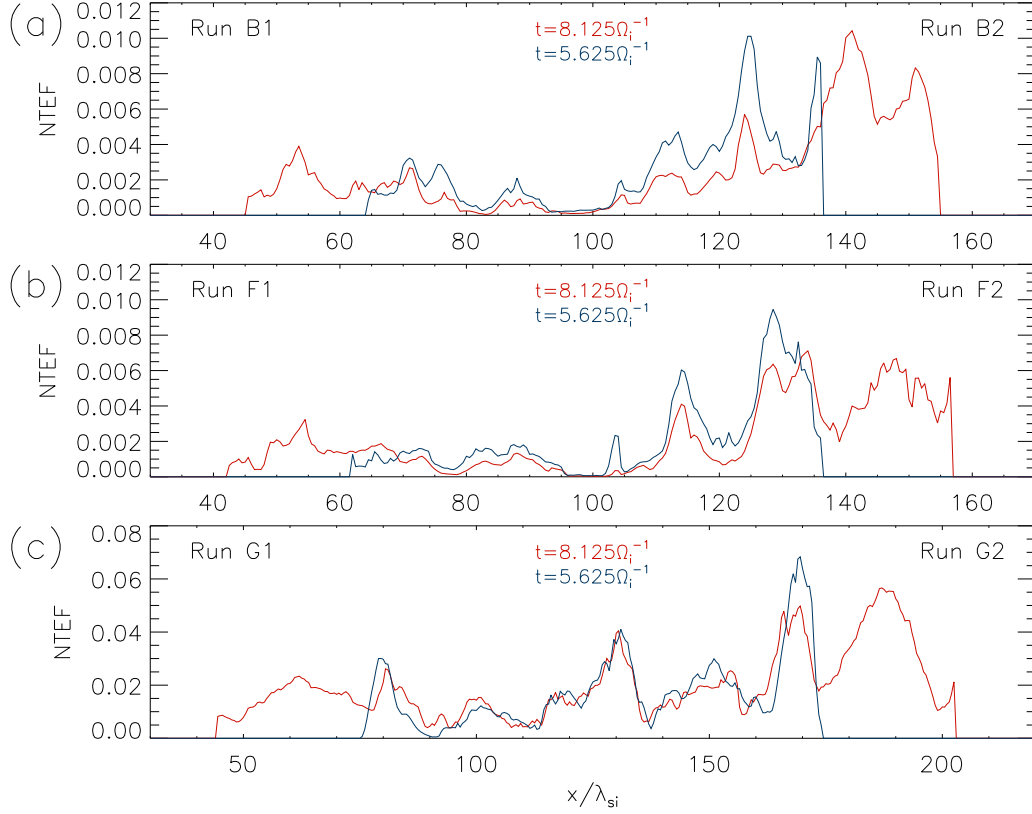
Figure 6.15: Profiles of nonthermal electron fraction for time steps $8.125\Omega_i^{-1}$ (red) and $5.625\Omega_i^{-1}$ (blue) for runs B (a), runs F (b) and runs G (c).

6.5.5 Downstream spectra for different magnetic field configurations

We conclude the presentation of this part of our results with the energy spectra of electrons in the downstream region. For that purpose we chose a region behind the overshoot that contains particles processed over two cycles of the shock reformation. The extent of this region is $2 \times 1.55\Omega_i^{-1} \times v_{sh} \simeq 25\lambda_{si}$ for runs B/F and $37.5\lambda_{si}$ for run G (recall that the shock speed is higher in run G).

Electron spectra for the in-plane ($\varphi = 0^o$), $\varphi = 45^o$, and the out-of-plane ($\varphi = 90^o$) configurations of the magnetic field and $\beta_e = 0.5$ are presented in Figure 6.16a. In all simulations we observe electrons with Lorentz factors up to $\gamma \approx 9$. The main difference between the spectra is at low energies, at which we can fit relativistic Maxwellians to represent the bulk of electrons, shown here with dashed lines. To be noted is the variation in the plasma temperature that results from the choice of the magnetic-field configuration. In the lower panel (b) of Figure 6.16 we display spectra in energy scaled to the plasma temperature. Whereas for $\varphi = 0^o$ and 45° we find almost indistinguishable spectra in rescaled energy, the spectrum for run G with the out-of-plane field features a much more pronounced spectral tail.

93

Table 6.2 summarizes our findings: the downstream temperature, the nonthermal electron fraction, and the number of energetic electrons are presented for all runs. Note, that besides the fit uncertainty in the temperature there is a spatial variation of the plasma temperature in the downstream region, and so we consider the plasma temperature for low and moderate β_e the same within the uncertainties. As was shown in Sections 6.5.1, 6.5.2 and 6.5.3, the number of pre-accelerated electrons and the final abundance of NTEF depend on the efficiency of the acceleration by the Buneman waves. The electron temperatures are higher by a factor of $2-4$ than those predicted by the Rankine-Hugoniot jump conditions, indicating that significant bulk heating has occurred (compare Matsumoto et al., 2012).

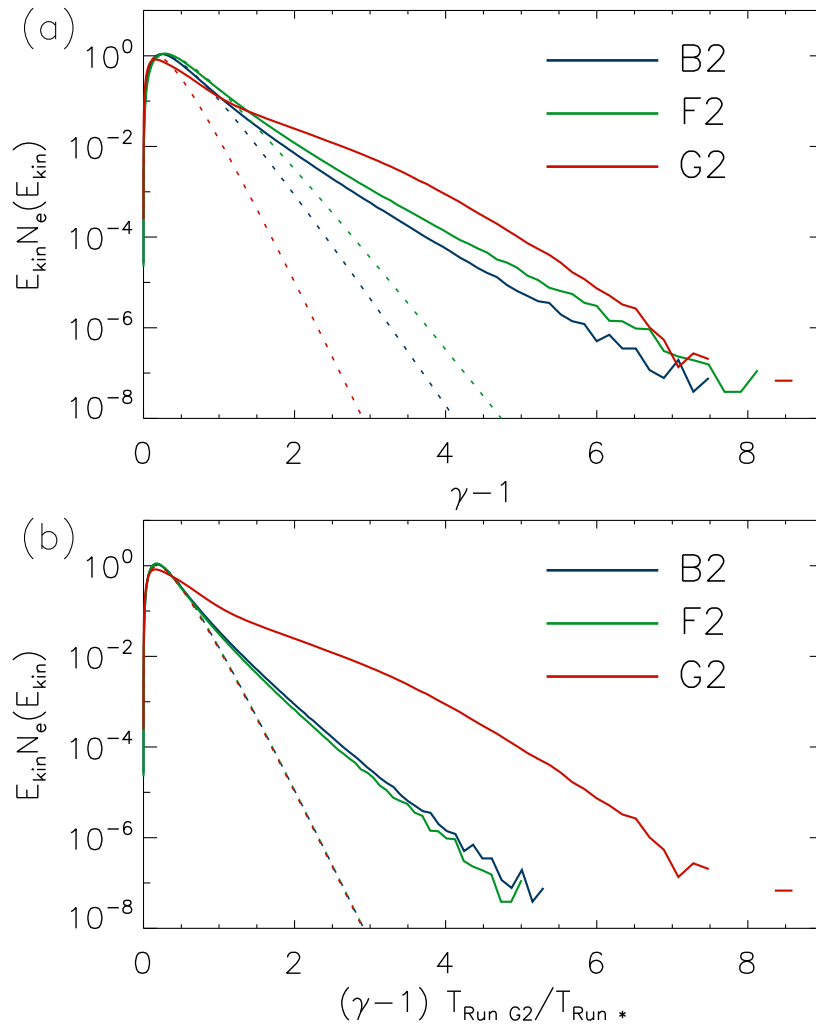Figure 6.16: In the top panel (a) we show electron spectra in the downstream region of the moderate-β_e shocks (a). The dashed lines represent fits of a relativistic Maxwellian to the low-energy spectra. The bottom panel (b) displays the distribution in rescaled energy in units of the downstream temperature. Blue lines correspond to run B2, green curves to run F2, and red curves to run G2.

Table 6.2: Downstream spectra parameters.
Note. – Comparison of the characteristics of the energy distribution of electrons in the downstream region of all six simulated shocks. $N_e(\gamma > 3)$ is the fraction of electrons in downstream electron spectra with energies $\gamma > 3$. NTEF denotes the nonthermal electron fraction.

Run	φ	NTEF (%)	$N_e(\gamma > 3)$ (%)	$k_B T/mc^2$
B1	0°	0.2 ± 0.1	0.1	0.053
B2	0°	0.7 ± 0.1	0.06	0.043
F1	45°	0.2 ± 0.1	0.11	0.054
F2	45°	0.5 ± 0.1	0.1	0.049
G1	90°	4 ± 1	0.12	0.032
G2	90°	7 ± 1	0.3	0.03

While the uncertainties in the determination of NTEF are sizable, we find a higher NTEF for moderate-β_e shocks, whatever the orientation of the large-scale magnetic field.

Efficient electron acceleration during passage through the shock ramp and overshoot will weaken the relation between the nonthermal fraction of electrons and the efficiency of SSA. In the $\varphi = 90^o$ case with the out-of-plane magnetic field the electron transport beyond the Buneman zone is adiabatic. Consequently, the distribution of electrons in magnetic moment (instead of their energy) is constant in time, and thus the numerical relation between thermal and nonthermal electrons is preserved. Then the number of nonthermal electrons should be a direct tracer of the SSA efficiency. In $\varphi = 0^o$ and $\varphi = 45^o$ configurations second-order Fermi-like processes operating in the shock ramp can change the number ratio of the thermal bulk and the nonthermal population. One of these processes is magnetic reconnection and the next section is dedicated to discuss these effects.

We do observe a correlation between the abundance of strong electrostatic field and the presence of a high-energy tail in the final downstream spectrum, expressed as either the maximum energy or the number of high-energy electrons with $\gamma > 3$. For the number of high-energy electrons one can find the same trend in all simulations: if the number of grid points with high-amplitude electrostatic field, $N_{es}(E_{es} > 0.5 B_0)$, is high, then the number of high-energy electrons, $N_e(\gamma > 3)$, is also high. Comparing shocks propagating in the cold and the warm plasma (low and moderate β_e, respectively), we find for runs B $N_{es,cold}(E_{es} > 0.5 B_0) > N_{es,warm}(E_{es} > 0.5 B_0)$, and indeed we observe a higher abundance of high-energy electrons for the low-β_e shock. For runs F, both the abundance of intense electrostatic field and the spectral

tails are similar for low and moderate β_e. For runs G, the correlation holds, but now we find strong electric field more rarely at shocks propagating into the cold plasma, and there are fewer energetic particles there than at the moderate-β_e shock. We can conclude that the population size of high-energy electrons (but not necessarily NTEF) is determined by energization in the Buneman zone.

6.6 Spontaneous magnetic reconnection

As mentioned in Section 6.2, magnetic reconnection that has been demonstrated by Matsumoto et al. (2015) to occur within the turbulent shock ramp was observed in four of our runs discussed in the preceding sections, namely runs B for $\varphi = 0^o$ and runs F for $\varphi = 45^o$. In this section we discuss the effects of magnetic recnnection and the role of this process in electron pre-acceleration. The discussion is based on results of runs B and F, and also on the results of additional simulations A, C, and D with the in-plane magnetic field ($\varphi = 0^o$) and runs E with $\varphi = 45^o$ configuration. For a given angle φ, these simulations differ in the assumed ion-to-electron mass ratio. It is in the range $m_i/m_e = 50 - 400$ for $\varphi = 0^o$, and $m_i/m_e = 50 - 100$ for $\varphi = 45^o$ (see Table 6.1). In all cases the Alfvén Mach numbers are set to satisfy the trapping condition of Equation 4.13. However, the shock Mach numbers do not satisfy our modified trapping condition of Equation 6.4 (see Section 6.4). Therefore we still expect SSA efficiencies to be smaller then in runs G for the out-of-plane field configuration. As the runs define essentially the same physical conditions in term of the trapping condition (Eq. 4.13), we expect similar SSA efficiencies for runs with the same magnetic field configurations but different ion-to-electron mass ratios. On the other hand, any departure from this expectation indicates the presence of new effects that are not accounted for in derivation of Equation 4.13. One of such effects can be magnetic reconnection, and our series of simulation runs is well suited to study in detail the influence of this effect on electron acceleration.

6.6.1 Properties and statistics of magnetic reconnection sites

In this section we discuss a detailed structure of the shock ramp or the Weibel instability region. The Weibel-type filamentation instability arises from the interaction between shock reflected ions and upstream plasma ions. These filaments are associated with current filaments and filamentary magnetic fields (Kato & Takabe, 2010b; Matsumoto et al., 2015; Wieland et al., 2016).

As shown in Matsumoto et al. (2015) for the in-plane magnetic-field configuration, magnetic
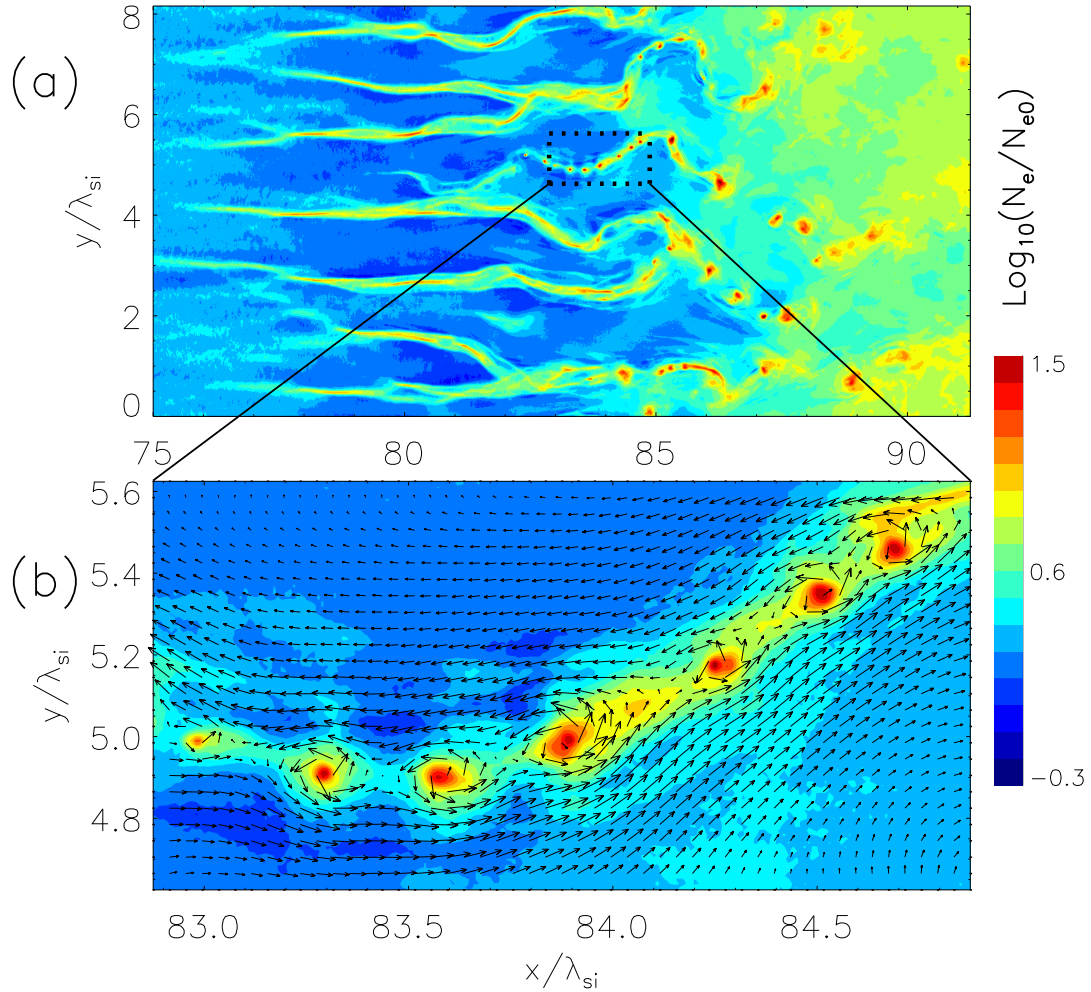
Figure 6.17: The shock ramp region in run D1 ($\varphi = 0^o$, panel (a)) at time $t = 2.7\Omega^{-1}$. The region marked with dotted lines in panel (a) is shown enlarged in panel (b). It harbors a chain of magnetic islands. The density is presented in a logarithmic scale and normalized to the upstream density. Arrows show the in-plane xy-component of the magnetic field.

filaments can trigger spontaneous turbulent magnetic reconnection in the shock ramp. We observe magnetic reconnection events not only for the in-plane (Fig. 6.17), but also for the $\varphi = 45^o$ configuration (Fig. 6.18). In both these cases dense filaments represent uniform Harris-type current layer (Harris, 1962), which consists of a thin dense plasma layer confined between two regions of oppositely directed magnetic field lines. Such a configuration is unstable and undergoes multiple magnetic reconnection forming X-points and magnetic islands. It is natural that magnetic reconnection is observed in simulations with $\varphi = 45^o$ configuration because the only difference in the structure of the shock ramp with in-plane and $\varphi = 45^o$ configuration is the inclination of Weibel filaments, which depends on direction of gyration of reflected ions in the ramp region, that, in turn, is defined by the orientation of the large-scale magnetic field. Magnetic reconnection is not observed in runs G with out-of-plane magnetic field configuration
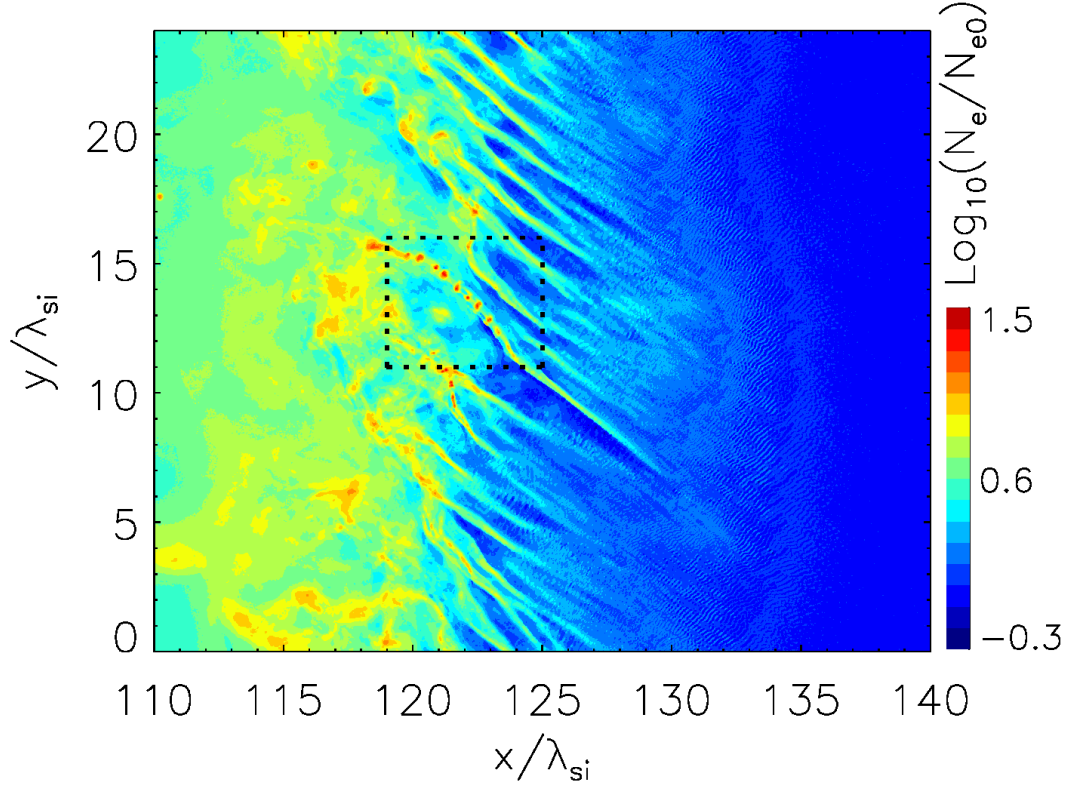
Figure 6.18: The electron density distribution of the shock region in run F2 ($\varphi = 45^o$) at time $t = 3.3\Omega^{-1}$. The magnetic reconnection region is marked with dotted lines.

because in these simulations particles are confined in the simulation plane, and one of the transverse field components, B_z, generated by the Weibel instability is not captured by the xy computational grid.

Figure 6.17a displays the shock ramp region for run D1 at time $t = 2.7\Omega^{-1}$. In this simulation, the foot region with electrostatic Buneman waves is located at $x/\lambda_{si} \approx (68 - 72)$ and the overshoot is at $x/\lambda_{si} \approx 93$ (both regions are not shown in Fig. 6.17a). The existence of magnetic islands resulting from magnetic reconnection is demonstrated in the enlarged view in Figure 6.17b. The density peaks are encircled by magnetic-field lines, which is a characteristic configuration for magnetic reconnection in a Harris current sheet. The magnetic-reconnection events can be identified as chains of magnetic islands separated by X-points, which result from nonlinear decay of the current sheets (Furth et al., 1963).

The shock ramp region contains variety of different structures that can be identified in the snapshot of Figure 6.17. Freshly formed dense filaments are at $x/\lambda_{si} \approx (75 - 83)$. Their separation scale is of the order of the ion inertia scale λ_{si}. Deeper into the ramp the filaments merge and undergo magnetic reconnection at $x/\lambda_{si} \approx (83 - 87)$. In the region at
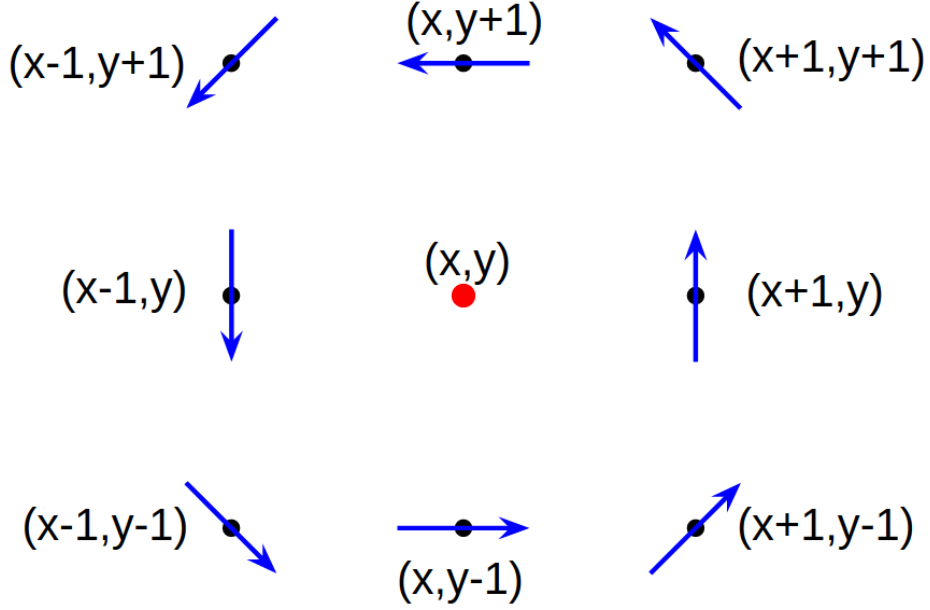
Figure 6.19: Magnetic field configuration near the magnetic vortex (island). The center of the magnetic vortex is at point (x, y). The in-plane magnetic field is designated by blue arrows.

$x/\lambda_{si} \approx (87 - 91)$ dense single magnetic islands remain after magnetic-island coalescence at $x/\lambda_{si} \approx (87 - 91)$. Note that shock self-reformation can strongly change the shock ramp structure. The ramp extension thus varies in a range of $L_{ramp} = (3 - 15)\lambda_{si}$ during one cycle of reformation, and conditions for magnetic reconnection exist only in the shock reformation phases with large filament extension.

To quantify the effect of magnetic reconnection and compare different simulation runs we introduce a notion of magnetic vortices, their generation rate and the electron density inside the magnetic vortex. The magnetic vortex is defined as the point with the configuration of the nearby in-plane magnetic field as in Figure 6.19. The magnetic field from the opposite sides of the point (x, y) should be oppositely directed. The magnetic field at all surrounding points rotates clockwise or anticlockwise. The electron density inside the magnetic vortex is the density at point (x, y).

The vortex generation rate (VGR) is defined as the number of magnetic vortices (or islands) observed at a given time step at the shock region normalized by the transverse size of the simulation box. The average values of VGR for all runs are listed in Table 6.3. The number of reconnection sites grows linearly with ion-to-electron mass ratio (compare runs A, B, C and D). Note that in the simulation runs with low mass ratios not all magnetic filaments undergo

Table 6.3: Vortex parameters.
Note. – VGR designates the vortex generation rate, AD is the average electron density inside magnetic vortices in simulation runs.

Run	φ	m_i/m_e	VGR	$Log_{10}(AD)$
A1	0°	50	0.2	1.13
A2	0°	50	0.2	1.01
B1	0°	100	0.7	0.99
B2	0°	100	0.9	1.01
C1	0°	200	1.9	1.03
C2	0°	200	2.3	1.04
D1	0°	400	4.4	1.01
D2	0°	400	5.8	1.04
E1	45°	50	0.3	0.82
E2	45°	50	0.3	0.80
F1	45°	100	1.4	0.81
F2	45°	100	1.5	0.83

decay via magnetic reconnection. One can see in Figure 6.18, that presents the shock region for run F2 with $m_i/m_e = 100$, that only one filament undergoes magnetic reconnection, whereas in the run with $m_i/m_e = 400$ (run D1, see Fig. 6.17) all filaments finally display the magnetic reconnection. The VGR is almost twice larger for runs with $\varphi = 45^o$ than with the in-plane magnetic field (compare VGR for runs A, B with that for runs E, F). The vortex statistics of runs B, C and D indicates that for moderate plasma beta (runs B2, C2 and D2) VGR is higher than for cold plasma (runs B1, C1 and D1). On the other hand, no such trend is observed for $\varphi = 45^o$ configuration.

The time evolution of VGR for run B1 is shown in Figure 6.20. This behavior is representative of all simulation runs. VGR varies in the range $0.2 - 1.4$ with an average value of 0.7. The period and the phase of these variations coincide with the period and the phase of the shock self-reformation. At a phase with a low flux of reflected ions magnetic filaments are almost absent in the ramp. Magnetic vortices can be formed only by turbulent plasma motions in the shock. Thus even in the absence of magnetic filaments VGR is never zero. The maximum value of VGR is observed when filaments have the largest extension and efficiently undergo magnetic reconnection. Variations in VGR are observed in all simulation runs. Their amplitude depends on the coherency of the shock self-reformation along the shock. Also the shock rippling can make these variations smaller on average and produce localized modulations of VGR along the shock surface.
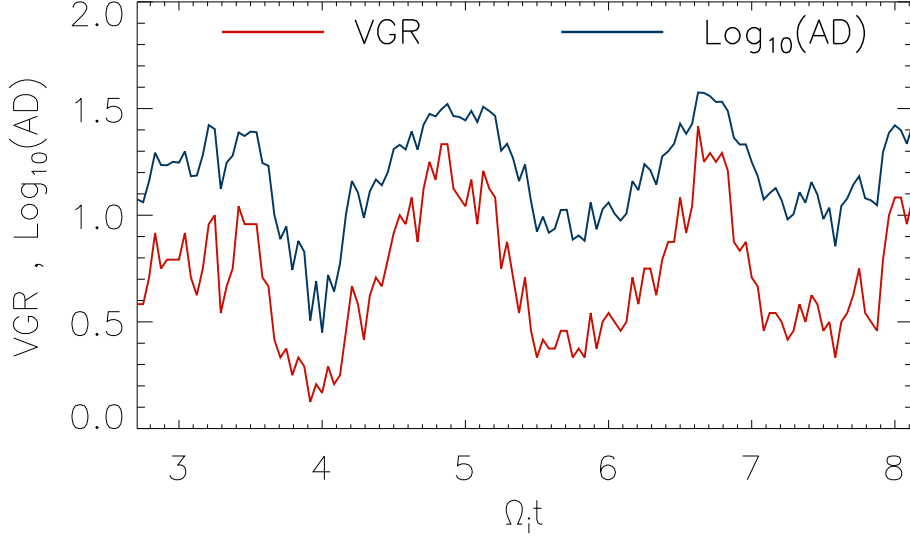
Figure 6.20: Time evolution of the vortex generation rate (VGR, red line) and the logarithm of the average electron density inside magnetic vortices (AD, blue line) in run B1.

Another quantity we have analyzed is the distribution and the average value of the electron density inside magnetic vortices found in the shock transition. Values of the logarithm of the average density (AD) of electrons inside magnetic islands in simulation runs are listed in Table 6.3. Simulations with in-plane magnetic field (runs A, B, C and D) provide similar AD values. Slightly higher value of AD for run A1 is probably a statistical fluctuation due to a small vortex statistics (just a few tens of vortices are identified for runs with $m_i/m_e = 50$). Simulations with $\varphi = 45^o$ magnetic field configuration (runs E and F) demonstrate smaller AD values. The time evolution of AD in run B1 (blue line in Fig. 6.20) shows that at time steps with minimum VGR, when vortices are generated by plasma turbulence, AD is smaller. This indicates that magnetic vortices generated via filaments decay are denser then vortices generated by plasma turbulence.

The probability density function (PDF) of the electron density in magnetic vortices is presented in Figure 6.21 for runs B1, C1, D1 and F1, for which good vortex statistics can be obtained. The PDF for run F1 strongly differs from other runs with the in-plane magnetic field. Filament decay in run F1 generates vortices with smaller density, and in addition many magnetic vortices arise not from the decay of magnetic filaments but are generated by magnetic turbulence in the ramp region. A small bump in a distribution for run D1 is observed for normalized density around 0.8 (green line in Fig. 6.21). It can be explained by the highest resolution among all simulation runs. For all simulations λ_{se} is fixed, ion skin depth is proportional to the square
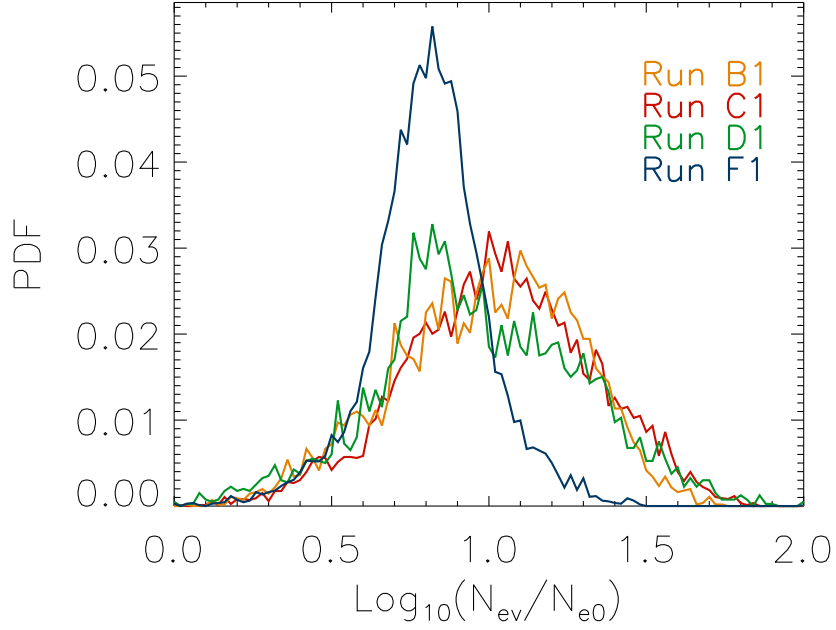
Figure 6.21: Probability density functions of the logarithm of the electron density (N_{ev}) inside magnetic vortices for runs B1 (yellow), C1 (red), D1 (green) and F1 (blue).

root of mass ratio, $\lambda_{si} = \lambda_{se} \cdot \sqrt{m_i/m_e}$, thus in run B1 $\lambda_{si} = 200\Delta$ while in run D1 $\lambda_{si} = 400\Delta$. Consequently, one can identify more turbulent magnetic islands in the magnetic field of run D1. On the other hand magnetic islands generated via filaments decay can be easily identified in all runs, because its sizes are of the order of λ_{si}.

We conclude that the properties of the vortices do not much depend on the ion-to-electron mass ratio, while the number of reconnection sites grows with m_i/m_e. Likewise, the probability density does not depend on the plasma beta.

6.6.2 Acceleration processes due to magnetic reconnection

It is well known that magnetic reconnection is a process that converts magnetic energy into thermal and kinetic particle energy. A number of acceleration processes are found in studies dedicated to the magnetic reconnection (see Section 4.3.3). Here we describe acceleration processes identified in our simulation runs.

To perform the analysis of the acceleration processes we subdivide the particle energy into two parts, namely, the energy gained during acceleration in the direction parallel and perpendicular to the local magnetic field lines. Note that many works (e.g., Dahlin et al., 2014, 2015) use a so-called guiding center limit (Northrop, 1963) for an identification of acceleration processes in magnetic reconnection simulations. However, our analysis of electron trajectories shows that this approach cannot be applied in our simulations, because the reconnection
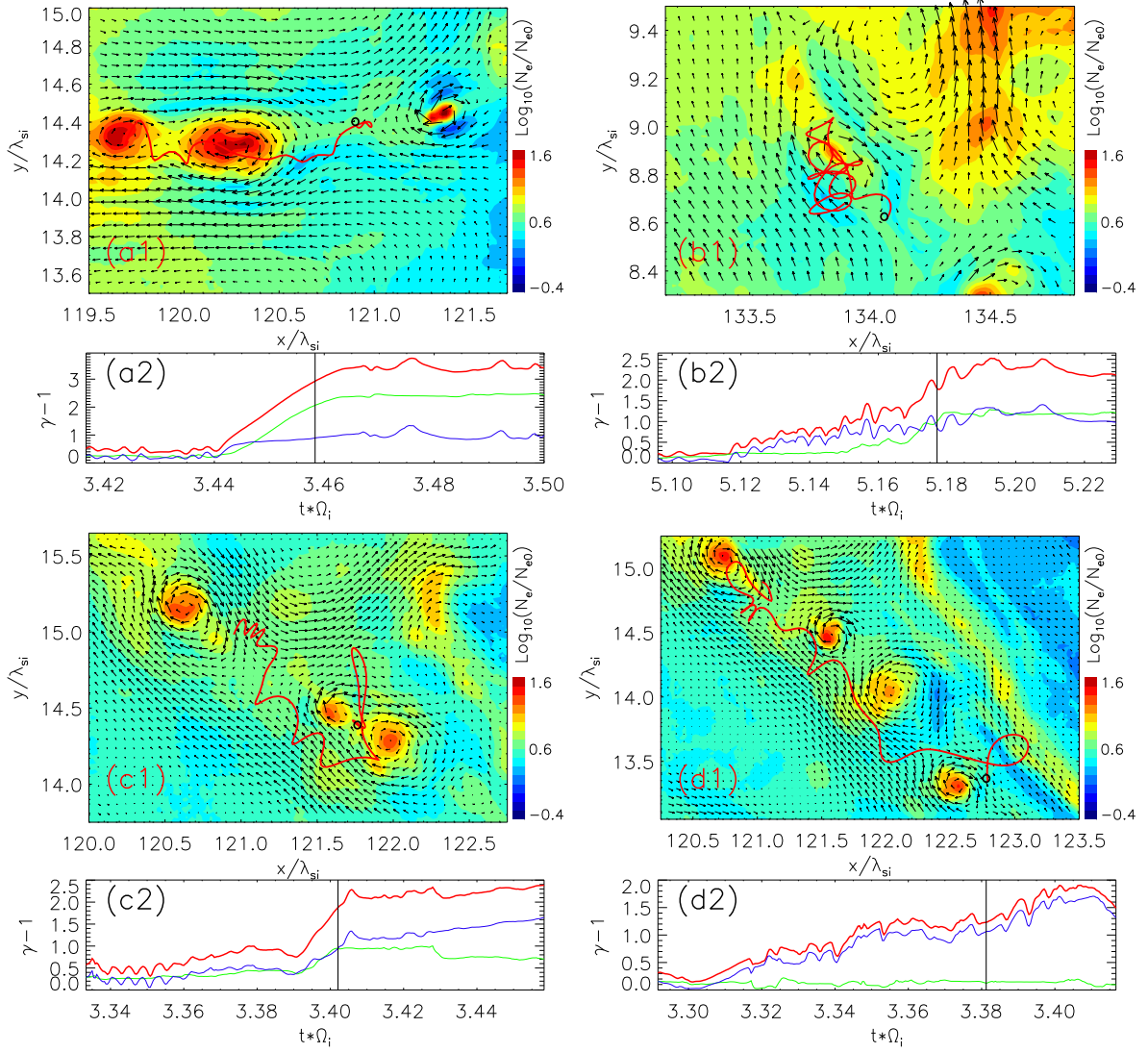
Figure 6.22: Trajectories and energy evolution of four accelerated electrons: two for run B2 (panels a* and b*) and two for run F2 (panels c* and d*). Panels (*1): color – normalized electron density in logarithmic scale; arrows – x-y magnetic-field lines; black circle – position of particle at the specific time marked in panels (*2); red line – trajectory of the electron over $\Delta t = 0.063\Omega_i^{-1}$. Panels (*2): Time evolution of the total kinetic energy of the electron (red line) and its parallel (green line) and perpendicular (blue line) components.

processes are too fast, whereas in the guiding center limit variations of electromagnetic fields during one electron gyroperiod should be small. Using our approach we can distinguish such processes as acceleration by the electric fields along the magnetic field lines (the parallel energy component) and Fermi-like interaction with magnetic structures (the perpendicular energy component).

Trajectories of four sample accelerated electrons that reach nonthermal energies in our simulations are presented in Figure 6.22. Electrons in panels (a1), (b1) and (c1), (d1) are selected from simulation runs B2 and F2, respectively. All particles reach the Lorentz factor

$(\gamma - 1) > 2$ that is above thermal particle energy.

The first electron (Fig. 6.22a) is accelerated by the *z*-component of the electric field at an X-point at $(x,y)/\lambda_{si} = (121, 14.4)$. During acceleration the electron stays in the vicinity of the X-point and only the *z*-component of its momentum (perpendicular to the simulation plane) increases. As panel 6.22a2 shows, the rapid growth of the parallel component of the energy is observed at this stage. This is an example of the Speiser motion (see, e.g.,Speiser, 1965; Hoshino et al., 2001).

The second electron (Fig. 6.22b) is accelerated while it is captured by a magnetic vortex. Both parallel and perpendicular energy components grow because of the acceleration by E_z inside the magnetic island and via contraction of the vortex, respectively. This acceleration process is identified as the "island surfing" mechanism (Oka, Fujimoto, et al., 2010).

The third electron (Fig. 6.22c) experienceS a first-order Fermi acceleration process by bouncing between merging magnetic islands. A charged particle undergoing head-on collision with a magnetic wall (a region with strong magnetic field), can be reflected back with higher energy if the magnetic field strength is high enough to revert particle trajectory. An electron residing in, so-called, anty-X-point (see Section 4.3.3) between merging magnetic vortices can move from one magnetic island to another undergoing head-on collisions. The growth of the perpendicular energy component corresponds to the Fermi-like acceleration, whereas the parallel energy growth occurs because of the E_z field is present in the anty-X-point.

The fourth electron experiences the second order Fermi-like acceleration process (Fig. 6.22d1). Decay of Weibel filaments via magnetic reconnection produces large number of magnetic vortices residing in the shock ramp and around the overshoot. Particles chaotically moving in these regions can be scattered by magnetic vortices. This situation is similar to the original second-order Fermi process (see Section 4.1) when particles undergo head-on, as well as tail-on collisions. The trajectory of accelerated electron is presented in Figure 6.22d1. The total energy evolution is well described by the perpendicular component only, while the parallel component does not change.

Number of other acceleration processes can occur in the magnetic reconnection regions (see Section 4.3.3). However, here we can identify only a few of them on account of the limited time magnetic reconnection has to evolve in the shock that is self-reforming. Typical simulation studies dedicated to magnetic reconnection may cover $\sim 100\Omega^{-1}_{i,mag\ rec}$ (see, e.g., Dahlin et al. (2014); Oka, Fujimoto, et al. (2010)) during which reconnection is steadily driven

in a controlled manner. The value of the ion gyrofrequency, $\Omega_{i,mag\ rec}$, that defines the time scale of magnetic reconnection in our simulations can be estimated by using the strength of the magnetic field that surrounds magnetic filaments. Therefore, the evolution of magnetic reconnection system from the filament formation to the emergence of a single magnetic vortex after island coalescence takes about $\sim 5\Omega_{i,mag\ rec}^{-1}$. Thus our simulations can describe only the early stage of the decay of a Harris current sheet before the reconnection structure is destroyed by the shock self-reformation. In addition, the size of magnetic islands that have merged in downstream close to the end a simulation can reach the size of about $\sim (10-20)\lambda_{si}$, which is comparable to or larger then our simulation box size.

6.6.3 Downstream spectra for different mass ratios

To study electron acceleration efficiency we analyze energy spectra of electrons in the downstream region. The spectra are calculated in a region downstream of the overshoot with size corresponding to two cycles of the shock self-reformation, namely, $L \simeq 25\lambda_{si}$ for the in-plane magnetic field configuration. In this way we average over all spectral distortions arising from the shock reformation (see Section 6.5.4).

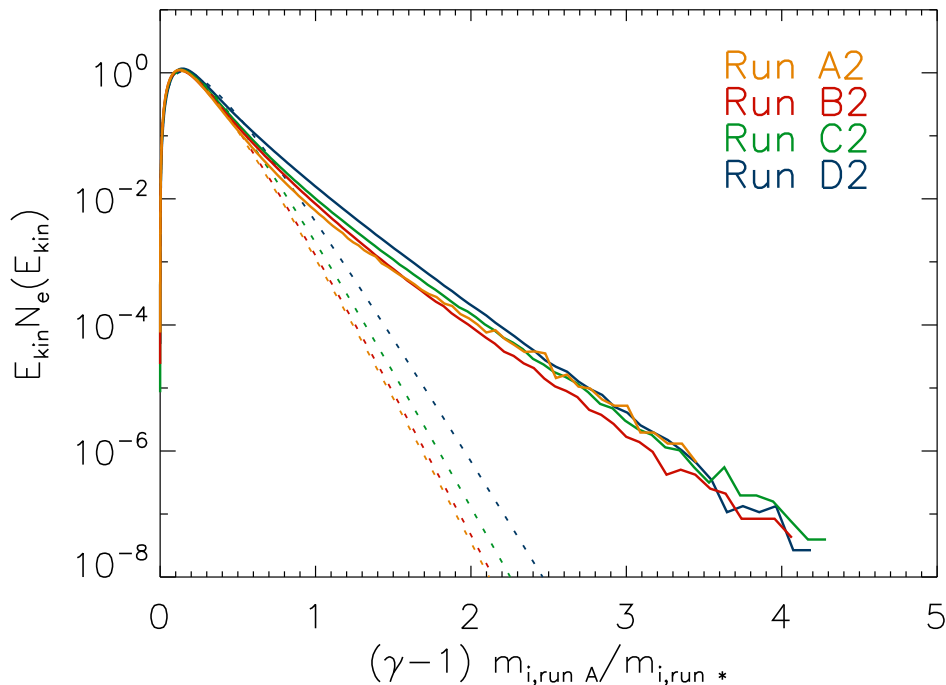
Figure 6.23: Electron spectra in the downstream region of the moderate-β_e shocks in runs A2, B2, C2 and D2. The dashed lines represent fits of a relativistic Maxwellian to the low-energy spectra. Yellow lines correspond to run A2, red lines run B2, green curves to run C2, and blue curves to run D2.

Table 6.4: Downstream spectra parameters.

Run	m_i/m_e	NTEF, %	$k_B T/mc^2$
A1	50	0.1 ± 0.1	0.029
A2	50	0.5 ± 0.2	0.022
B1	100	0.2 ± 0.1	0.053
B2	100	0.7 ± 0.1	0.043
C1	200	0.2 ± 0.1	0.097
C2	200	0.5 ± 0.1	0.093
D1	400	0.4 ± 0.1	0.2
D2	400	0.5 ± 0.1	0.204

Particle spectra for runs with the in-plane magnetic-field configuration are presented in Figure 6.23. The spectra are scaled with the ion-to-electron mass ratio, $(\gamma - 1)_{run*} \, m_{i,runA2}/m_{i,run*}$, where "$*$" corresponds to runs A2, B2, C2 and D2. Dotted lines in Figure 6.23, representing Maxwellian fits to the low-energy spectra, show that the downstream bulk temperature linearly scales with the ion-to-electron mass ratio. Shocks with higher Mach numbers produce stronger heating according to the Rankine-Hugoniot conditions in the MHD description (see Sections 3.2 and 3.3). Also stochastic interactions of electrons with magnetic field turbulence that is stronger at shocks with with higher Mach numbers lead to electron acceleration via the second-order Fermi mechanism to higher energies.

The nonthermal electron fractions (NTEF) and downstream temperatures ($k_B T/mc^2$) for all runs are listed in Table 6.4. NTEF for runs A, B, C and D are statistically indistinguishable. The value of shock Mach number in these simulations implies the same efficiency of the SSA mechanism. We observe similar relation between NTEF for shock propagating in cold and moderate-β_e plasma (see Section 6.5.5). NTEF is higher for moderate-β_e shocks, independent of ion-to-electron mass ratio.

Our previous investigation demonstrates that the nonthermal electron fraction is defined by the intensity of electrostatic Buneman waves. Comparing spectra for various ion-to-electron mass ratios, and hence different abundance of magnetic-reconnection events, we can conclude that magnetic reconnection does not have a significant influence on the downstream electron spectra. Careful analysis of electron trajectories reveals that electrons which cross the Buneman instability zone at the peak intensity of the waves later interact with magnetic reconnection sites at time with the highest VGR. Thus, it is impossible to find a region in the downstream, in

which there are particles accelerated via one of these processes only. A separation of SSA and the acceleration via magnetic reconnection requires additional investigations that would damp the Buneman waves and at the same time enable spontaneous turbulent magnetic reconnection.

CHAPTER 7
SUMMARY AND CONCLUSIONS

This thesis presents results of 2D3V PIC simulations of electron injection and acceleration processes in non-relativistic perpendicular collisionless shocks with high Alfvén Mach number. Such shocks are hosted in young SNRs which are believed to provide the main part of galactic cosmic ray population through the first-order Fermi (DSA) acceleration process. Efficiency of particle injection is still poorly understood, though crucial for realistic modeling of CR spectra at sources. This work focuses on electron pre-acceleration. Two injection mechanisms are considered: shock-surfing acceleration by electrostatic Buneman waves at the shock foot and acceleration related to the spontaneous turbulent magnetic reconnection in the shock ramp. Physical conditions under which these processes operate efficiently are sought. On this line the simulation parameters are chosen to permit the growth of the Buneman waves and trapping of electrons at the shock foot (Matsumoto et al., 2012). We explore the efficiency of electron energization for shocks in plasmas with low and moderate β_e. A 2D3V simulation model is chosen because of computational limitations. However, three orientation angles, φ, between the large-scale magnetic field and the simulation plane are considered to enable us to draw conclusions on pre-acceleration efficiency in fully three-dimensional settings. We also investigate a range of ion-to-electron mass ratios, m_i/m_e. The results can be summarized as follows:

- The collision of two plasma slabs leads to the formation of a double shock system and a CD. Development time of the shocks is about $2\Omega_i^{-1}$. In general, the structure of the shocks is similar in all runs; they consist of the upstream, foot, overshoot, and downstream regions. In detail, the influence of the global magnetic field on the phase-space distribution of shock-reflected ions imposes differences in the evolution of the Buneman and the Weibel instabilities.

- The simulated shocks undergo cyclic self-reformation on account of the nonstationary character of ion reflection at the shock. The period of shock reformation is $\sim 1.55\Omega^{-1}$ which is essentially the value obtained in earlier investigations of high Mach number shocks ($1.5\Omega^{-1}$ in Wieland et al., 2016). This period neither depends on the magnetic-field configuration nor on the plasma beta. For the simulation time of eight ion gyrotimes, $t = 8\Omega_i^{-1}$, roughly three cycles of the shock self-reformation are observed.

- Reflected ions interact with incoming electrons and excite electrostatic Buneman waves

at the leading edge of the foot region. The parameters of our simulations satisfy the trapping condition (Matsumoto et al., 2012), and so electrons should be accelerated by the convective electric field. The intensity of the electrostatic waves, the area they occupy, and, subsequently, the fraction of nonthermal electrons strongly depend on the global magnetic-field orientation. Simulations with the out-of-plane magnetic-field configuration produce the highest fractions of nonthermal electrons. In cases with $\varphi = 0^o$ and $\varphi = 45^o$, part of the counterstreaming motion of reflected ions proceeds in z-direction, but the k_z component of the Buneman waves driven by it is not captured by the xy simulation grid. Consequently, the saturation level of the waves and their ability to trap electrons is less than for $\varphi = 90^o$, for which we observe a higher intensity of Buneman waves at the shock foot and a larger volume coverage. With Equation 6.4 we propose a revision to the trapping condition originally formulated by Matsumoto et al. (2012), that offers an explanation why some of the simulations presented here, and others described in the literature, have a low Buneman efficiency. If the new revised trapping condition (Eq. 6.4) is met, as in our simulation with $\varphi = 90^o$, then the number of electrons undergoing SSA is large, at least as long as the plasma beta $\beta_e \lesssim 1$. A similar modification can be applied to the driving condition, leading to Equation 6.5.

- Shock self-reformation leads to temporal variations in the electrostatic-wave intensity in the foot region, and consequently the electron energization in these regions becomes time-dependent. After crossing the Buneman-wave zone the fraction of nonthermal electrons does not change significantly. The cyclic shock reformation then imposes quasi-periodic fluctuations in the temperature and density of bulk electrons as well as the density of high-energy electrons, that lead to variations in the nonthermal fraction of electrons. For runs with $\varphi = 0^o$ and $\varphi = 45^o$ we observe that the fraction of nonthermal electrons in the downstream region decreases with time. Runs with out-of-plane magnetic field configuration do not show this effect.

- For all simulated shocks we find suprathermal tails in the electron spectra in the downstream region, but the acceleration efficiency depends on the magnetic-field orientation. For all configurations the main acceleration process is through interaction with electrostatic waves in the Buneman wave zone at the shock foot, followed by further energization by turbulent magnetic structures and in the shock overshoot. The weight of the individual contributions by all these processes depends on the magnetic-field

configuration. The cases $\varphi = 0^o$ and $\varphi = 45^o$ lead to the same acceleration processes, and we do not see any significant difference between them. In contrast, the $\varphi = 90^o$ configuration provides a fundamentally different behavior. In this case the intensity of Buneman waves at the shock foot is higher, because the new trapping condition (Eq. 6.4) is satisfied, and the waves are coherent and found in a larger region as the result of coherent ion reflection by magnetic field at the overshoot. One consequence is that electrons gyrating in the foot region can cross the Buneman wave zone more than once, experience more shock-surfing acceleration, and reach a higher energy than they would with a $\varphi = 0^o$ or $\varphi = 45^o$ configuration, for which we do not observe such multiple interactions. The number of high-energy electrons (at $\gamma > 1.5$) in the Buneman zone is correspondingly larger for $\varphi = 90^o$ than it is for the other cases. In all simulations the Buneman instability serves as injector, i.e., electrons are accelerated to suprathermal energies by electrostatic waves at the leading edge of the foot region. The second stage of electron energization is second-order Fermi acceleration by interaction with magnetic filaments in simulations with 0° or 45° configuration, and it is adiabatic acceleration in the case of the out-of-plane magnetic field. For all simulations, the Lorentz factor of the most energetic electron is $\gamma \approx 9$, but the fraction of nonthermal electrons is more then 10 times larger for $\varphi = 90^o$ than for the other configuration on account of the higher SSA efficiency in the foot region. There is no clear trend between the number of high-energy electrons and the β_e value of the plasma into which the shock propagates. For $\varphi = 90^o$ we observe more electrons above $\gamma = 3$ in the moderate-β_e case than for the low β_e. For the other simulations with $\varphi = 0^o$ and $\varphi = 45^o$, we find the opposite trend. This issue will require further studies. However for a given magnetic-field orientation, we observe a higher nonthermal fraction at shocks propagating into moderate-β_e plasma than for low β_e.

- Spontaneous turbulent magnetic reconnection in the shock transition is observed only in the in-plane and $\varphi = 45^o$ magnetic field configurations. The number of magnetic-reconnection sites increases with numerical ion-to-electron mass ratio. Runs with $\varphi = 45^o$ demonstrate almost twice lager value of the magnetic vortex generation rate than simulations with $\varphi = 0^o$. The probability density function of the electron density inside magnetic vortices is different in these two cases. The average electron density inside vortices is smaller for runs with $\varphi = 45^o$ due to the nature of the filament decay process,

in which considerable part of magnetic islands are generated through island mergers in turbulent plasma downstream of the filamentary region, and not via magnetic filaments decay. This decreases the average density of vortices. The probability density function does not depend on the plasma beta. However, the vortex generation rate is about 20% higher for shocks propagating in moderate temperature plasma.

- Interactions of electrons with magnetic reconnection sites lead to electron energization to nonthermal energies. Acceleration occurs in many different mechanisms. We identify few of them, namely, acceleration in the E_z electric field at an X-point of the magnetic reconnection site (Speiser orbits), electron capture in the magnetic islands ("island surfing"), acceleration by bouncing between colliding magnetic islands (first-order Fermi-like acceleration), and stochastic collisions with magnetic vortices (second-order Fermi-like acceleration). These processes are capable of producing electrons with non-thermal energies. However, the live time of the magnetic reconnection in the shock ramp is very short due to shock self-reformation that destroys magnetic filaments. Our simulations can thus cover only the early stage of the magnetic reconnection process. Considerably larger transverse size of the simulation box and longer simulation times are required to observe other acceleration processes at the shock related to magnetic reconnection, such as the surfing acceleration, interaction with plasma outflows during magnetic islands coalescence, etc. (see Section 4.3.3).

- Downstream electron spectra for simulations with different mass ratios demonstrate statistically indistinguishable nonthermal fractions. The downstream bulk temperature linearly scales with the ion-to-electron mass ratio. The nonthermal electron fraction is higher for moderate-β_e shocks for all runs meaning that this trend does not depend on ion-to-electron mass ratio, m_i/m_e, and the global magnetic field orientation, φ. Taking into account similar efficiency of SSA mechanism, we conclude that magnetic reconnection does not impose a significant influence on downstream spectra of electrons. A role of magnetic reconnection in electron injection and separation of SSA and acceleration via magnetic reconnection requires further detailed scrutiny.

Table 7.1: Comparison of the electron pre-acceleration efficiency in the present and in other published simulations.

Note. – We state whether or not the old (Eq. 4.13) and the revised (Eq. 6.4) trapping conditions are met. Notes are presented for simulations with weak nonthermal population and where both old (Eq. 4.13) and the revised (Eq. 6.4) trapping conditions are satisfied.

Run	φ	β_e	Eq. 4.13	Eq. 6.4	Nonthermal population	Notes
B1; B2	0°	$5 \cdot 10^{-4}$; 0.5	Yes	No	Weak	
Kato and Takabe (2010b)	0°	26	Yes	Yes	Absent	High temperature of reflected ions
Matsumoto et al. (2015)	0°	0.5	Yes	No	Weak or absent	
F1; F2	45°	$5 \cdot 10^{-4}$; 0.5	Yes	No	Weak	
Wieland et al. (2016)	45°	0.0015; 0.015	Yes	Yes	Weak or absent	Spectra far downstream
G1; G2	90°	$5 \cdot 10^{-4}$; 0.5	Yes	Yes	Strong	
Matsumoto et al. (2012)(Run A)	90°	0.5	Yes	Yes	Strong	
Matsumoto et al. (2012)(Run B)	90°	0.5	No	No	Weak	
Matsumoto et al. (2012)(Run C)	90°	0.5	Yes	Yes	Strong	
Matsumoto et al. (2012)(Run D)	90°	4.5	Yes	Yes	Weak	Weak driving

This thesis presents evidence for a significant variation in the efficiency of electron acceleration at perpendicular high-Mach-number shocks, that depends on the choice of the orientation of the large-scale magnetic field with respect to the simulation plane. Much but not all of the variation can be traced to the efficiency of driving the Buneman instability at the shock foot. Our findings are summarized in Table 7.1 in the context of other published results (Kato & Takabe, 2010b; Matsumoto et al., 2012, 2015; Wieland et al., 2016). There are three parameters that have an influence on a downstream spectra and final fraction of nonthermal electrons: the electron plasma beta, β_e, the trapping condition in earlier (Eq. 4.13) and in the revised form (Eq. 6.4), and the driving condition that can be likewise revised (Eq. 6.5). For $\varphi = 90^o$ case the old and new trapping conditions are identical, and the nonthermal electron population appears to be sparse if the trapping condition is not satisfied (run B in Matsumoto et al. (2012)) or if a high plasma beta leads to early saturation of the Buneman instability (the thermal velocity of electrons is about half the streaming speed of reflected ions in run D of Matsumoto et al., 2012). A weak population of nonthermal electrons is observed in our runs with $\varphi = 0^o$ and $\varphi = 45^o$ as well as in the simulation described by Matsumoto et al. (2015), because the Alfvén Mach number is too low to satisfy the revised trapping condition. Wieland et al. (2016) discuss shocks with Mach numbers M_A and M_s large enough to drive Buneman waves and trap electrons, even if the modified conditions are applied. Their electron spectra are extracted in the far-downstream region, from which the high-energy electrons leak (see Section 6.5.4). This may explain a very low observed nonthermal fraction of electrons. The modified driving and trapping conditions were also fulfilled in the simulation of Kato and Takabe (2010b) for very large M_A. However, as the authors argue, the high temperature of reflected ions reduced the Buneman wave growth rate by about an order of magnitude. Further systematic studies of high Mach number shocks in a wide parameter range are required to confirm the validity of the revised trapping conditions in configurations with the in-plane and $\varphi = 45^o$ magnetic fields.

Despite that in our simulations with the in-plane and $\varphi = 45^o$ magnetic field configurations the trapping condition in the revised form of Equation 6.4 is not satisfied, still strong electron pre-acceleration occurs via SSA in the shock foot. This processes dominate other electron energization channel associated with turbulent magnetic reconnection. Determination of the role of magnetic reconnection in electron injection thus requires further detailed scrutiny with additional simulations that would separate the SSA from the effects of magnetic reconnection. Such simulations could, e.g., be performed in a range of Mach numbers below and above the

limit provided by the trapping conditions.

We have presented results of 2D3V simulations, but the real world is 3D throughout. The question arises which behavior one would observe in 3D and which of the 2D3V configurations provides the closest match to the 3D case. By definition, all wavevectors lie in the simulation plane, and so for $\varphi = 90^o$ only electromagnetic modes with B_x or B_y components can rotate particles out of the simulation plane. Particle trajectories are thus approximately confined to the simulation plane, and the particle ensemble assumes an effective adiabatic index of 2, as opposed to 5/3 for a 3D monoatomic gas. We indeed observe the corresponding difference in shock speeds, etc., and the 3D shock structure may be not accurately reproduced for $\varphi = 90^o$. On the other hand, with $\varphi = 90^o$ the counterstreaming of reflected ions and the driving of Buneman modes in the shock foot is fully captured by the *x-y* simulation grid. The fair fraction of nonthermal electrons produced in $\varphi = 90^o$ simulations is probably a better indicator of the 3D acceleration efficiency at the shock foot than is the very low abundance of energetic electrons for $\varphi = 0^o$ and $\varphi = 45^o$. Magnetic reconnection in 3D can reveal much more complicated structures (Priest & Schrijver, 1999). Dimensionality may also play important role in the efficiency of acceleration processes in magnetic reconnection regions (see, e.g., Dahlin et al., 2015; Kowal, de Gouveia Dal Pino, & Lazarian, 2011). True 3D simulations are urgently needed to resolve these issues. However, such simulations require extensive computational resources. For example, a 3D simulation with the parameters of our smallest runs A and E (transverse simulation box size, simulation time, ion-to-electron mass ratio $m_i/m_e = 50$), would require about 10 million CPU-hours. Taking into account that the number of magnetic reconnection events observed in runs A and E is very small, much higher mass ratio and also larger simulation box should be used. This significantly increases the amount of required computational resources and is hardly feasible with Peta-scale computing.

The main goal of the work presented in this thesis is to identify physical conditions at collisionless astrophysical shocks under which efficient injection of electrons to the DSA process occurs. The SSA process at high Mach number perpendicular shocks has been shown here to provide significant non-thermal electron populations. However, a self-consistent injection into the first-order Fermi process at shocks has not yet been demonstrated. Irrespective of the fact that a PIC simulation covering vast spatial and energy scales required to observe the DSA process in multi dimensions seems prohibitive under current computational constraints, the microphysics of the SSA mechanism itself may not allow electron acceleration beyond the

energy range observed in our simulations. However, theoretical considerations suggest that SSA is only the first step in the electron injection. Using one-dimensional PIC simulations Amano and Hoshino (2007) showed that nonthermal electrons accelerated via SSA can be further energized by the shock drift acceleration (SDA). Subsequent work by Amano and Hoshino (2010) demonstrated that there exists a critical shock Alfvén Mach number above which an efficient electron injection should occur. The SDA can be treated as an adiabatic mirror reflection process in the de Hoffman-Teller frame. The beam of reflected electrons excites whistler waves in the shock transition, and the critical Mach number for this to occur is:

$$M_A^{inj} \equiv \frac{\cos\theta}{2}\sqrt{\frac{m_i}{m_e}\beta_e} \,. \tag{7.1}$$

Recent observations seem to support this picture. *In-situ* observations of Saturn's bow shock by the *Cassini* spacecraft have shown that the Mach number of this shock can reach values comparable to those observed in SNRs. The analysis of about 500 shock crossings (Masters et al., 2016) reveals non-thermal electrons only at shocks whose parameters satisfy the critical Mach number condition (Eq. 7.1), even though the shock parameters span a wide range of obliquities ($\theta = 10 - 90^o$) and Mach numbers ($M_A = 3 - 200$). Nevertheless, some unresolved problems still remain: even if a shock Mach number is above the critical value, the non-thermal population is not always observed. Another *in-situ* observations of the Earth's bow shock by *Magnetospheric Multiscale Satellite* (MMS) are also in support of the presented theory (Oka et al., 2017). They report a direct evidence for the cyclotron resonance between non-thermal particles and the whistler waves.

Using the injection mechanism of Amano and Hoshino (2007, 2010) one can find a negligibly small portion of reflected electrons for strictly perpendicular shocks ($\theta = 90^o$). The beam density of electrons undergoing SDA reaches the maximum at quasi-perpendicular shocks with $\theta = 75^o - 80^o$ (Amano & Hoshino, 2007). The SSA efficiency at perpendicular shocks is similar to that at quasi-perpendicular shocks (Shimada & Hoshino, 2000; Hoshino & Shimada, 2002; Amano & Hoshino, 2007). Also in Amano and Hoshino (2009a) it was shown that the SSA efficiency in 2D simulations with out-of-plane magnetic field configuration is larger than in 1D case for the same simulation parameters, because y velocity component of reflected ions can also drive Buneman instability. Taking into account these conclusions and parameters of 1D simulation done by Amano and Hoshino (2007) ($m_i/m_e = 100$ and $M_A \simeq 15$), the injection efficiency in at quasi-perpendicular shock with the parameters similar to that in run

G1 (where $m_i/m_e = 100$, $M_A \simeq 35.5$, and the most efficient SSA is observed) can be estimated as larger then the value of $\sim 2 \cdot 10^{-4}$ derived in Amano and Hoshino (2007). The exact value depends on the shock parameters, such as the shock potential that reflects electrons, the escape probability of electrons, the maximum energy cutoff, etc., all of which are poorly constrained. However, this result can be directly compared with X-ray and radio observations of SNRs. The injection efficiency estimated as the fraction of non-thermal electrons is about $\sim 10^{-3}$ for the remnant SN1006 (Bamba, Yamazaki, Ueno, & Koyama, 2003), which is comparable to the value estimated above.

A conclusion of this thesis is that the process of shock-surfing acceleration at high Mach number perpendicular shocks can, under appropriate conditions, pre-accelerate electrons to enable their further injection into the DSA mechanism. These conditions can be provided in young SNR environments that are central to the SNR paradigm of galactic CR production. A discussion above demonstrates that important constraints on this scenario can also come from investigations of other systems, such as planetary shocks. Our simulations can also be useful for studies of quasi-parallel shocks. During the self-reformation of a quasi-parallel shock the direction of the shock normal fluctuates considerably. Because of that the quasi-parallel shock on the scales of the order of the tangential extension of large amplitude pulsations may locally effectively acquire a quasi-perpendicular configuration. On such scales, similar processes of electron acceleration may take place as in the quasi-perpendicular case. However, it needs to be verified whether such effects can significantly contribute to the electron injection in the quasi-parallel shocks.

REFERENCES

Aab, A., Abreu, P., Aglietta, M., Ahn, E. J., Samarai, I. A., Albuquerque, I. F. M., ... et al. (2015, May). Searches for Anisotropies in the Arrival Directions of the Highest Energy Cosmic Rays Detected by the Pierre Auger Observatory. ApJ, *804*, 15. doi: 10.1088/0004-637X/804/1/15

Aab, A., Abreu, P., Aglietta, M., Al Samarai, I., Albuquerque, I. F. M., Allekotte, I., ... et al. (2016, October). Search for ultrarelativistic magnetic monopoles with the Pierre Auger observatory. Phys. Rev. D, *94*(8), 082002. doi: 10.1103/PhysRevD.94.082002

Abbasi, R. U., Abu-Zayyad, T., Allen, M., Amman, J. F., Archbold, G., Belov, K., ... et al. (2008, March). First Observation of the Greisen-Zatsepin-Kuzmin Suppression. *Physical Review Letters*, *100*(10), 101101. doi: 10.1103/PhysRevLett.100.101101

Abdalla, H., Abramowski, A., Aharonian, F., Ait Benkhali, F., Akhperjanian, A. G., Andersson, T., ... et al. (2016a, September). H.E.S.S. observations of RX J1713.7-3946 with improved angular and spectral resolution; evidence for gamma-ray emission extending beyond the X-ray emitting shell. *ArXiv e-prints*.

Abdalla, H., Abramowski, A., Aharonian, F., Ait Benkhali, F., Akhperjanian, A. G., Andersson, T., ... et al. (2016b, September). The supernova remnant W49B as seen with H.E.S.S. and Fermi-LAT. *ArXiv e-prints*.

Abraham, J., Abreu, P., Aglietta, M., Aguirre, C., Allard, D., Allekotte, I., ... et al. (2008, August). Observation of the Suppression of the Flux of Cosmic Rays above 4×10^{19}eV. *Physical Review Letters*, *101*(6), 061101. doi: 10.1103/PhysRevLett.101.061101

Abramowski, A., Aharonian, F., Benkhali, F. A., Akhperjanian, A. G., Angüner, E. O., Backes, M., ... et al. (2016, March). Acceleration of petaelectronvolt protons in the Galactic Centre. Nature, *531*, 476-479. doi: 10.1038/nature17147

Ackermann, M., Ajello, M., Allafort, A., Baldini, L., Ballet, J., Barbiellini, G., ... Zimmer, S. (2013, February). Detection of the Characteristic Pion-Decay Signature in Supernova Remnants. *Science*, *339*, 807-811. doi: 10.1126/science.1231160

Afanasiev et al. (1996).
Proc. Int. Symp. on Extremely High Energy Cosmic Rays; Astrophysics and Future Observations, ed. M. Nagano, ICRR, U. of Tokyo.

Aharonian, F., Akhperjanian, A. G., Bazer-Bachi, A. R., Beilicke, M., Benbow, W., Berge, D., ... Ward, M. (2007, March). Primary particle acceleration above 100 TeV in the shell-type supernova remnant <ASTROBJ>RX J1713.7-3946</ASTROBJ> with deep HESS observations. A&A, *464*, 235-243. doi: 10.1051/0004-6361:20066381

Ahlers, M., & Mertsch, P. (2017, May). Origin of small-scale anisotropies in Galactic cosmic rays. *Progress in Particle and Nuclear Physics*, *94*, 184-216. doi: 10.1016/j.ppnp.2017.01 .004

Aleksić, J., Ansoldi, S., Antonelli, L. A., Antoranz, P., Babic, A., Bangale, P., ... Meyer, M. (2015, March). Measurement of the Crab Nebula spectrum over three decades in energy with the MAGIC telescopes. *Journal of High Energy Astrophysics*, *5*, 30-38. doi: 10.1016/ j.jheap.2015.01.002

Allard, D., Parizot, E., & Olinto, A. V. (2007, February). On the transition from galactic to extragalactic cosmic-rays: Spectral and composition features from two opposite scenarios. *Astroparticle Physics*, *27*, 61-75. doi: 10.1016/j.astropartphys.2006.09.006

Aloisio, R., Matarrese, S., & Olinto, A. V. (2015, August). Super Heavy Dark Matter in light of BICEP2, Planck and Ultra High Energy Cosmic Rays Observations. Journal of Cosmology and Astroparticle Physics, *8*, 024. doi: 10.1088/1475-7516/2015/08/024

Amano, T., & Hoshino, M. (2007, May). Electron Injection at High Mach Number Quasi-perpendicular Shocks: Surfing and Drift Acceleration. ApJ, *661*, 190-202. doi: 10.1086/ 513599

Amano, T., & Hoshino, M. (2009a, January). Electron Shock Surfing Acceleration in Multidimensions: Two-Dimensional Particle-in-Cell Simulation of Collisionless Perpendicular Shock. ApJ, *690*, 244-251. doi: 10.1088/0004-637X/690/1/244

Amano, T., & Hoshino, M. (2009b, October). Nonlinear evolution of Buneman instability and its implication for electron acceleration in high Mach number collisionless perpendicular shocks. *Physics of Plasmas*, *16*(10), 102901. doi: 10.1063/1.3240336

Amano, T., & Hoshino, M. (2010, May). A Critical Mach Number for Electron Injection in Collisionless Shocks. *Physical Review Letters*, *104*(18), 181102. doi: 10.1103/PhysRevLett .104.181102

Archambault, S., Archer, A., Benbow, W., Bird, R., Bourbeau, E., Buchovecky, M., ... Zitzer, B. (2017, February). Gamma-Ray Observations of Tycho's Supernova Remnant with VERITAS and Fermi. ApJ, *836*, 23. doi: 10.3847/1538-4357/836/1/23

Axford, W. I. (1994, February). The origins of high-energy cosmic rays. ApJS, *90*, 937-944. doi: 10.1086/191928

Axford, W. I., Leer, E., & Skadron, G. (1977). The acceleration of cosmic rays by shock waves. *International Cosmic Ray Conference*, *11*, 132-137.

Baade, W., & Zwicky, F. (1934, July). Remarks on Super-Novae and Cosmic Rays. *Physical Review*, *46*, 76-77. doi: 10.1103/PhysRev.46.76.2

Bagenal, F., & Bridge, H. (1987). The magnetosphere of Uranus: Voyager plasma science observations. In *Bulletin of the american astronomical society* (Vol. 19, p. 632).

Bale, S. D., Kellogg, P. J., Larsen, D. E., Lin, R. P., Goetz, K., & Lepping, R. P. (1998). Bipolar electrostatic structures in the shock transition region: Evidence of electron phase

space holes. Geophys. Res. Lett., *25*, 2929-2932. doi: 10.1029/98GL02111

Bamba, A., Yamazaki, R., Ueno, M., & Koyama, K. (2003, June). Small-Scale Structure of the SN 1006 Shock with Chandra Observations. ApJ, *589*, 827-837. doi: 10.1086/374687

Bell, A. R. (1978a, January). The acceleration of cosmic rays in shock fronts. I. MNRAS, *182*, 147-156. doi: 10.1093/mnras/182.2.147

Bell, A. R. (1978b, February). The acceleration of cosmic rays in shock fronts. II. MNRAS, *182*, 443-455. doi: 10.1093/mnras/182.3.443

Bell, A. R. (2004, September). Turbulent amplification of magnetic field and diffusive shock acceleration of cosmic rays. MNRAS, *353*, 550-558. doi: 10.1111/j.1365-2966.2004.08097 .x

Bell, A. R. (2005, March). The interaction of cosmic rays and magnetized plasma. MNRAS, *358*, 181-187. doi: 10.1111/j.1365-2966.2005.08774.x

Berezhko, E. G., Ksenofontov, L. T., & Völk, H. J. (2013, January). The Nature of Gamma-Ray Emission of Tycho's Supernova Remnant. ApJ, *763*, 14. doi: 10.1088/0004-637X/763/1/14

Berezinsky, V., Gazizov, A., & Grigorieva, S. (2006, August). On astrophysical solution to ultrahigh energy cosmic rays. Phys. Rev. D, *74*(4), 043005. doi: 10.1103/PhysRevD.74 .043005

Berezinsky, V., Kachelrieß, M., & Vilenkin, A. (1997, December). Ultrahigh Energy Cosmic Rays without Greisen-Zatsepin-Kuzmin Cutoff. *Physical Review Letters*, *79*, 4302-4305. doi: 10.1103/PhysRevLett.79.4302

Bhattacharjee, P. (2000, March). Origin and propagation of extremely high energy cosmic rays. Phys. Rep., *327*, 109-247. doi: 10.1016/S0370-1573(99)00101-5

Bird, D. J., Corbato, S. C., Dai, H. Y., Dawson, B. R., Elbert, J. W., Emerson, B. L., . . . Thomas, S. B. (1994, March). The cosmic-ray energy spectrum observed by the Fly's Eye. ApJ, *424*, 491-502. doi: 10.1086/173906

Birdsall, C. K., & Langdon, A. B. (1991). *Plasma Physics via Computer Simulation*.

Blandford, R., & Eichler, D. (1987, October). Particle Acceleration at Astrophysical Shocks-a Theory of Cosmic-Ray Origin. *Physics Reports*, *154*, 0–0.

Blandford, R. D., & McKee, C. F. (1976, August). Fluid dynamics of relativistic blast waves. *Physics of Fluids*, *19*, 1130-1138. doi: 10.1063/1.861619

Blandford, R. D., & Ostriker, J. P. (1978, April). Particle acceleration by astrophysical shocks. ApJ, *221*, L29-L32. doi: 10.1086/182658

Blasi, P., & Amato, E. (2012, January). Diffusive propagation of cosmic rays from supernova remnants in the Galaxy. I: spectrum and chemical composition. Journal of Cosmology and Astroparticle Physics, *1*, 010. doi: 10.1088/1475-7516/2012/01/010

Bocchino, F., Orlando, S., Miceli, M., & Petruk, O. (2011, July). Constraints on the local interstellar magnetic field from non-thermal emission of SN1006. A&A, *531*, A129. doi: 10.1051/0004-6361/201016341

Boris, J. P. (1970). Relativistic plasma simulation-optimization of a hybrid code. *Proceedings of the Fourth Conference on Numerical Simulation Plasmas, Naval Research Laboratory, Washington, D.C.*, 3–67.

Breizman, B. N., & Riutov, D. D. (1974, December). Powerful relativistic electron beams in a plasma and in a vacuum /theory/. *Nuclear Fusion*, *14*, 873-907.

Brogan, C. L., Gelfand, J. D., Gaensler, B. M., Kassim, N. E., & Lazio, T. J. W. (2006, March). Discovery of 35 New Supernova Remnants in the Inner Galaxy. ApJ, *639*, L25-L29. doi: 10.1086/501500

Buneman. (1993). TRISTAN: The 3-d electromagnetic particle code. *Computer Space Plasma Physics: Simulation Techniques and Software Eds.: Matsumoto & Omura, Tokyo: Terra*, 67-84.

Buneman, O. (1958, July). Instability, Turbulence, and Conductivity in Current-Carrying Plasma. *Physical Review Letters*, *1*, 8-9. doi: 10.1103/PhysRevLett.1.8

Buneman, O. (1959, August). Dissipation of Currents in Ionized Media. *Physical Review*, *115*, 503-517. doi: 10.1103/PhysRev.115.503

Burgess, D., & Scholer, M. (2007, January). Shock front instability associated with reflected ions at the perpendicular shock. *Physics of Plasmas*, *14*(1), 012108-012108. doi: 10.1063/1.2435317

Burgess, D., Wilkinson, W. P., & Schwartz, S. J. (1989, July). Ion distributions and thermalization at perpendicular and quasi-perpendicular supercritical collisionless shocks. J. Geophys. Res., *94*, 8783-8792. doi: 10.1029/JA094iA07p08783

Bykov, A. M., Chevalier, R. A., Ellison, D. C., & Uvarov, Y. A. (2000, July). Nonthermal Emission from a Supernova Remnant in a Molecular Cloud. ApJ, *538*, 203-216. doi: 10.1086/309103

Cargill, P. J., & Papadopoulos, K. (1988, June). A mechanism for strong shock electron heating in supernova remnants. ApJ, *329*, L29-L32. doi: 10.1086/185170

Carpio, J. A., & Gago, A. M. (2016, January). Impact of Galactic magnetic field modeling on searches of point sources via ultrahigh energy cosmic ray-neutrino correlations. Phys. Rev. D, *93*(2), 023004. doi: 10.1103/PhysRevD.93.023004

Clark, D. H., & Caswell, J. L. (1976, February). A study of galactic supernova remnants, based on Molonglo-Parkes observational data. MNRAS, *174*, 267-305. doi: 10.1093/mnras/174.2.267

Courant, R., Friedrichs, K., & Lewy, H. (1928). Über die partiellen Differenzengleichungen der mathematischen Physik. *Mathematische Annalen*, *100*, 32-74. doi: 10.1007/BF01448839

Cronin, J. W. (1992, November). Summary of the workshop. *Nuclear Physics B Proceedings Supplements*, *28*, 213-225. doi: 10.1016/0920-5632(92)90134-E

Cronin, J. W., Gaisser, T. K., & Swordy, S. P. (1997, January). Cosmic Rays at the Energy Frontier. *Scientific American*, *276*, 44-49, updated in www.physics.utah.edu/ whanlon/spectrum.html. doi: 10.1038/scientificamerican0197-44

Dahlin, J. T., Drake, J. F., & Swisdak, M. (2014, September). The mechanisms of electron heating and acceleration during magnetic reconnection. *Physics of Plasmas*, *21*(9), 092304. doi: 10.1063/1.4894484

Dahlin, J. T., Drake, J. F., & Swisdak, M. (2015, October). Electron acceleration in three-dimensional magnetic reconnection with a guide field. *Physics of Plasmas*, *22*(10), 100704. doi: 10.1063/1.4933212

Dawson, J. M. (1983, April). Particle simulation of plasmas. *Reviews of Modern Physics*, *55*, 403-447. doi: 10.1103/RevModPhys.55.403

Drake, J. F., Swisdak, M., Che, H., & Shay, M. A. (2006, October). Electron acceleration from contracting magnetic islands during reconnection. Nature, *443*, 553-556. doi: 10.1038/ nature05116

Drury, L. O., & Voelk, J. H. (1981, August). Hydromagnetic shock structure in the presence of cosmic rays. ApJ, *248*, 344-351. doi: 10.1086/159159

Fang, J., Yu, H., Zhu, B.-T., & Zhang, L. (2013, October). Gamma-ray properties of supernova remnants transporting into molecular clouds: the cases of IC 443 and W44. MNRAS, *435*, 570-574. doi: 10.1093/mnras/stt1318

Farrar, G. R., Awal, N., Khurana, D., & Sutherland, M. (2015, July). The Galactic Magnetic Field and UHECR Optics. In *34th international cosmic ray conference (icrc2015)* (Vol. 34, p. 560).

Fermi, E. (1949, April). On the Origin of the Cosmic Radiation. *Physical Review*, *75*, 1169-1174. doi: 10.1103/PhysRev.75.1169

Filbet, F., Sonnendrücker, E., & Bertrand, P. (2001, September). Conservative Numerical Schemes for the Vlasov Equation. *Journal of Computational Physics*, *172*, 166-187. doi: 10.1006/jcph.2001.6818

Fodor, Z., & Katz, S. D. (2001, April). Grand Unification Signal from Ultrahigh Energy Cosmic Rays? *Physical Review Letters*, *86*, 3224-3227. doi: 10.1103/PhysRevLett.86.3224

Fried, B. D. (1959, May). Mechanism for Instability of Transverse Plasma Waves. *Physics of Fluids*, *2*, 337-337. doi: 10.1063/1.1705933

Fried, B. D., & Conte, S. D. (1961). *The Plasma Dispersion Function*.

Friedman, A. (1990). Damped time advance methods for particles and EM fields. *US–Japan Workshop on Advanced Computer Simulation Techniques Applied to Plasmas and Fusion*.

Furth, H. P., Killeen, J., & Rosenbluth, M. N. (1963, April). Finite-Resistivity Instabilities of a Sheet Pinch. *Physics of Fluids*, *6*, 459-484. doi: 10.1063/1.1706761

Galeev, A. A., Sagdeev, R. Z., Shapiro, V. D., & Shevchenko, V. I. (1977, February). Relaxation of high-current electron beams and the modulational instability. *Soviet Journal of Experimental and Theoretical Physics*, *45*, 507-517.

Genzel, R., Eisenhauer, F., & Gillessen, S. (2010, October). The Galactic Center massive black hole and nuclear star cluster. *Reviews of Modern Physics*, *82*, 3121-3195. doi: 10.1103/RevModPhys.82.3121

Giacalone, J. (2003, September). The physics of particle acceleration by collisionless shocks. Planet. Space Sci., *51*, 659-664. doi: 10.1016/S0032-0633(03)00101-6

Ginzburg, V. L., & Syrovatsky, S. I. (1961). Origin of Cosmic Rays. *Progress of Theoretical Physics Supplement*, *20*, 1-83. doi: 10.1143/PTPS.20.1

Green, D. A. (1984, July). Statistical studies of supernova remnants. MNRAS, *209*, 449-478. doi: 10.1093/mnras/209.3.449

Greenwood, A. D., Cartwright, K. L., Luginsland, J. W., & Baca, E. A. (2004, December). On the elimination of numerical Cerenkov radiation in PIC simulations. *Journal of Computational Physics*, *201*, 665-684. doi: 10.1016/j.jcp.2004.06.021

Greisen, K. (1966, April). End to the Cosmic-Ray Spectrum? *Physical Review Letters*, *16*, 748-750. doi: 10.1103/PhysRevLett.16.748

Grigorov, N. L., Gubin, Y. V., Jakovlev, B. M., Rapoport, I. D., Savenko, I. A., Akimov, V. V., & Nesterov, V. E. (1971). Energy Spectrum of Primary Cosmic Rays in the 10^{11}-10^{15} eV According to the Data of Proton-4 Measurements. (Abstract). *International Cosmic Ray Conference*, *1*, 170.

Guo, X., Sironi, L., & Narayan, R. (2014, October). Non-thermal Electron Acceleration in Low Mach Number Collisionless Shocks. I. Particle Energy Spectra and Acceleration Mechanism. ApJ, *794*, 153. doi: 10.1088/0004-637X/794/2/153

Hanlon, W. F. (2008). *The energy spectrum of ultra high energy cosmic rays measured by the High Resolution Fly's Eye observatory in stereoscopic mode* (Unpublished doctoral dissertation). The University of Utah.

Harlow, F. (1955). A Machine Calculation Method for Hydrodynamic Problems. *Los Alamos Scientific Laboratory report LAMS-1956.*.

Harris, E. G. (1962, January). On a plasma sheath separating regions of oppositely directed magnetic field. *Il Nuovo Cimento*, *23*, 115-121. doi: 10.1007/BF02733547

Hellinger, P., Trávníček, P., Lembège, B., & Savoini, P. (2007, July). Emission of nonlinear whistler waves at the front of perpendicular supercritical shocks: Hybrid versus full particle simulations. Geophys. Res. Lett., *34*, L14109. doi: 10.1029/2007GL030239

Hess, V. F. (1912, November). Über Beobachtungen der durchdringenden Strahlung bei sieben

Freiballonfahrten. *Physikalische Zeitschrift*, *12*, 1084-1091.

Hillas, A. M. (1984). The Origin of Ultra-High-Energy Cosmic Rays. ARA&A, *22*, 425-444. doi: 10.1146/annurev.aa.22.090184.002233

Hillas, A. M. (2005, May). TOPICAL REVIEW: Can diffusive shock acceleration in supernova remnants account for high-energy galactic cosmic rays? *Journal of Physics G Nuclear Physics*, *31*, R95-R131. doi: 10.1088/0954-3899/31/5/R02

Hooper, D., Sarkar, S., & Taylor, A. M. (2007, March). The intergalactic propagation of ultra-high energy cosmic ray nuclei. *Astroparticle Physics*, *27*, 199-212. doi: 10.1016/j.astropartphys.2006.10.008

Hörandel, J. R. (2004, June). Models of the knee in the energy spectrum of cosmic rays. *Astroparticle Physics*, *21*, 241-265. doi: 10.1016/j.astropartphys.2004.01.004

Hoshino, M. (2005, October). Electron surfing acceleration in magnetic reconnection. *Journal of Geophysical Research (Space Physics)*, *110*, A10215. doi: 10.1029/2005JA011229

Hoshino, M. (2012, March). Stochastic Particle Acceleration in Multiple Magnetic Islands during Reconnection. *Physical Review Letters*, *108*(13), 135003. doi: 10.1103/PhysRevLett.108.135003

Hoshino, M., Mukai, T., Terasawa, T., & Shinohara, I. (2001, November). Suprathermal electron acceleration in magnetic reconnection. J. Geophys. Res., *106*, 25979-25998. doi: 10.1029/2001JA900052

Hoshino, M., & Shimada, N. (2002, June). Nonthermal Electrons at High Mach Number Shocks: Electron Shock Surfing Acceleration. ApJ, *572*, 880-887. doi: 10.1086/340454

Ishihara, O., Hirose, A., & Langdon, A. B. (1980, May). Nonlinear saturation of the Buneman instability. *Physical Review Letters*, *44*, 1404-1407. doi: 10.1103/PhysRevLett.44.1404

Jüttner, F. (1911). Das Maxwellsche Gesetz der Geschwindigkeitsverteilung in der Relativtheorie. *Annalen der Physik*, *339*, 856-882. doi: 10.1002/andp.19113390503

Kato, T. N., & Takabe, H. (2008, July). Nonrelativistic Collisionless Shocks in Unmagnetized Electron-Ion Plasmas. ApJ, *681*, L93. doi: 10.1086/590387

Kato, T. N., & Takabe, H. (2010a, March). Electrostatic and electromagnetic instabilities associated with electrostatic shocks: Two-dimensional particle-in-cell simulation. *Physics of Plasmas*, *17*(3), 032114-032114. doi: 10.1063/1.3372138

Kato, T. N., & Takabe, H. (2010b, September). Nonrelativistic Collisionless Shocks in Weakly Magnetized Electron-Ion Plasmas: Two-dimensional Particle-in-cell Simulation of Perpendicular Shock. ApJ, *721*, 828-842. doi: 10.1088/0004-637X/721/1/828

Kendall, M. K. (1970). *Rank correlation methods.*

Klimontovich, Y. L. (1997). Physics of collisionless plasma. *Phys. Usp.*, *40*, 21-51. doi: 10.3367/UFNr.0167.199701c.0023

Kobzar, O., Niemiec, J., Pohl, M., & Bohdan, A. (2017, August). Spatio-temporal evolution of the non-resonant instability in shock precursors of young supernova remnants. MNRAS, *469*, 4985-4998. doi: 10.1093/mnras/stx1201

Kowal, G., de Gouveia Dal Pino, E. M., & Lazarian, A. (2011, July). Magnetohydrodynamic Simulations of Reconnection and Particle Acceleration: Three-dimensional Effects. ApJ, *735*, 102. doi: 10.1088/0004-637X/735/2/102

Krauss-Varban, D., & Burgess, D. (1991, January). Electron acceleration at nearly perpendicular collisionless shocks. II - Reflection at curved shocks. J. Geophys. Res., *96*, 143-154. doi: 10.1029/90JA01728

Krymskii, G. F. (1977, June). A regular mechanism for the acceleration of charged particles on the front of a shock wave. *Akademiia Nauk SSSR Doklady*, *234*, 1306-1308.

Kulsrud, R. M. (2005). *Plasma physics for astrophysics*.

Landau, L. D., & Lifshitz, E. M. (1959). *Fluid mechanics*.

Langdon, A. B. (1985, October). Implicit Plasma Simulation. Space Sci. Rev., *42*, 67-83. doi: 10.1007/BF00218224

Lawrence, M. A., Reid, R. J. O., & Watson, A. A. (1991, May). The cosmic ray energy spectrum above $4*10^{17}$ eV as measured by the Haverah Park array. *Journal of Physics G Nuclear Physics*, *17*, 733-757. doi: 10.1088/0954-3899/17/5/019

Lembege. (2003). Full Particle Electromagnetic Simulation of Collisionless Shocks. In J. Büchner, C. Dum, & M. Scholer (Eds.), *Space plasma simulation* (Vol. 615, p. 54-78).

Lembege, & Simonet, F. (2001, September). Hybrid and particle simulations of an interface expansion and of collisionless shock: A comparative and quantitative study. *Physics of Plasmas*, *8*, 3967-3981. doi: 10.1063/1.1389862

Lembege, B., & Dawson, J. M. (1987, June). Self-consistent study of a perpendicular collisionless and nonresistive shock. *Physics of Fluids*, *30*, 1767-1788. doi: 10.1063/1.866191

Leroy, M. M. (1983, September). Structure of perpendicular shocks in collisionless plasma. *Physics of Fluids*, *26*, 2742-2753. doi: 10.1063/1.864468

Leroy, M. M., Goodrich, C. C., Winske, D., Wu, C. S., & Papadopoulos, K. (1981, December). Simulation of a perpendicular bow shock. Geophys. Res. Lett., *8*, 1269-1272. doi: 10.1029/GL008i012p01269

Leroy, M. M., Winske, D., Goodrich, C. C., Wu, C. S., & Papadopoulos, K. (1982, July). The structure of perpendicular bow shocks. J. Geophys. Res., *87*, 5081-5094. doi: 10.1029/JA087iA07p05081

Lever, E. L., Quest, K. B., & Shapiro, V. D. (2001, April). Shock surfing vs. shock drift acceleration. Geophys. Res. Lett., *28*, 1367-1370. doi: 10.1029/2000GL012516

Lindman, E. L. (1975, May). "Free-Space" Boundary Conditions for the Time Dependent Wave Equations. *Journal of Computational Physics*, *18*, 66-78. doi: 10.1016/0021-9991(75)90102-3

Longair, M. S. (2011). *High Energy Astrophysics*.

Lowe, R. E., & Burgess, D. (2003, March). The properties and causes of rippling in quasi-perpendicular collisionless shock fronts. *Annales Geophysicae*, *21*, 671-679. doi: 10.5194/angeo-21-671-2003

Marshall, w. (1955). The structure of magneto-hydrodynamic shock waves. *Proc R Soc Lond A*, 233-367.

Masters, A., Sulaiman, A. H., Sergis, N., Stawarz, L., Fujimoto, M., Coates, A. J., & Dougherty, M. K. (2016, July). Suprathermal Electrons at Saturn's Bow Shock. ApJ, *826*, 48. doi: 10.3847/0004-637X/826/1/48

Matsukiyo, S., Ohira, Y., Yamazaki, R., & Umeda, T. (2011, November). Relativistic Electron Shock Drift Acceleration in Low Mach Number Galaxy Cluster Shocks. ApJ, *742*, 47. doi: 10.1088/0004-637X/742/1/47

Matsumoto, Y., Amano, T., & Hoshino, M. (2012, August). Electron Accelerations at High Mach Number Shocks: Two-dimensional Particle-in-cell Simulations in Various Parameter Regimes. ApJ, *755*, 109. doi: 10.1088/0004-637X/755/2/109

Matsumoto, Y., Amano, T., & Hoshino, M. (2013, November). Electron Acceleration in a Nonrelativistic Shock with Very High Alfvén Mach Number. *Physical Review Letters*, *111*(21), 215003. doi: 10.1103/PhysRevLett.111.215003

Matsumoto, Y., Amano, T., Kato, T. N., & Hoshino, M. (2015, February). Stochastic electron acceleration during spontaneous turbulent reconnection in a strong shock wave. *Science*, *347*, 974-978. doi: 10.1126/science.1260168

Morlino, G., & Caprioli, D. (2011). Acceleration of cosmic rays in Tycho's SNR. Mem. Soc. Astron. Italiana, *82*, 731.

Mueller, D., Swordy, S. P., Meyer, P., L'Heureux, J., & Grunsfeld, J. M. (1991, June). Energy spectra and composition of primary cosmic rays. ApJ, *374*, 356-365. doi: 10.1086/170125

Nagano, M., Teshima, M., Matsubara, Y., Dai, H. Y., Hara, T., Hayashida, N., . . . Yoshida, S. (1992, February). Energy spectrum of primary cosmic rays above $10^{17.0}$ eV determined from extensive air shower experiments at Akeno. *Journal of Physics G Nuclear Physics*, *18*, 423-442. doi: 10.1088/0954-3899/18/2/022

Neronov, A. Y., Semikoz, D. V., & Tkachev, I. I. (2009, June). Ultra-high energy cosmic ray production in the polar cap regions of black hole magnetospheres. *New Journal of Physics*, *11*(6), 065015. doi: 10.1088/1367-2630/11/6/065015

Niemiec, J., Pohl, M., Bret, A., & Wieland, V. (2012, November). Nonrelativistic Parallel Shocks in Unmagnetized and Weakly Magnetized Plasmas. ApJ, *759*, 73. doi: 10.1088/0004-637X/759/1/73

Niemiec, J., Pohl, M., Stroman, T., & Nishikawa, K.-I. (2008, September). Production of Magnetic Turbulence by Cosmic Rays Drifting Upstream of Supernova Remnant Shocks. ApJ, *684*, 1174-1189. doi: 10.1086/590054

Nishikawa, K.-I., Niemiec, J., Hardee, P. E., Medvedev, M., Sol, H., Mizuno, Y., ... Hartmann, D. H. (2009, June). Weibel Instability and Associated Strong Fields in a Fully Three-Dimensional Simulation of a Relativistic Shock. ApJ, *698*, L10-L13. doi: 10.1088/0004 -637X/698/1/L10

Northrop, T. G. (1963). Adiabatic Charged-Particle Motion. *Reviews of Geophysics and Space Physics*, *1*, 283-304. doi: 10.1029/RG001i003p00283

Ohsawa, Y. (1985, July). Strong ion acceleration by a collisionless magnetosonic shock wave propagating perpendicularly to a magnetic field. *Physics of Fluids*, *28*, 2130-2136. doi: 10.1063/1.865394

Oka, M., Fujimoto, M., Shinohara, I., & Phan, T. D. (2010, August). Island surfing mechanism of electron acceleration during magnetic reconnection. *Journal of Geophysical Research (Space Physics)*, *115*, A08223. doi: 10.1029/2010JA015392

Oka, M., Phan, T.-D., Krucker, S., Fujimoto, M., & Shinohara, I. (2010, May). Electron Acceleration by Multi-Island Coalescence. ApJ, *714*, 915-926. doi: 10.1088/0004-637X/ 714/1/915

Oka, M., Wilson, L. B., III, Phan, T. D., Hull, A. J., Amano, T., Hoshino, M., ... Lindqvist, P. A. (2017, June). Electron Scattering by High-frequency Whistler Waves at Earth's Bow Shock. ApJ, *842*, L11. doi: 10.3847/2041-8213/aa7759

Okuda, H. (1972, December). Nonphysical Noises and Instabilities in Plasma Simulation due to a Spatial Grid. *Journal of Computational Physics*, *10*, 475-486. doi: 10.1016/ 0021-9991(72)90048-4

Papadopoulos, K. (1988, May). Electron heating in superhigh Mach number shocks. Ap&SS, *144*, 535-547. doi: 10.1007/BF00793203

Petruk, O., Dubner, G., Castelletti, G., Bocchino, F., Iakubovskyi, D., Kirsch, M. G. F., ... Telezhinsky, I. (2009, March). Aspect angle for interstellar magnetic field in SN 1006. MNRAS, *393*, 1034-1040. doi: 10.1111/j.1365-2966.2008.14251.x

Priest, E. R., & Schrijver, C. J. (1999, December). Aspects of Three-Dimensional Magnetic Reconnection - (Invited Review). Sol. Phys., *190*, 1-24. doi: 10.1023/A:1005248007615

Protheroe, R. J., & Szabo, A. P. (1992, November). High energy cosmic rays from active galactic nuclei. *Physical Review Letters*, *69*, 2885-2888. doi: 10.1103/PhysRevLett.69 .2885

Quest, K. B. (1985, April). Simulations of high-Mach-number collisionless perpendicular shocks in astrophysical plasmas. *Physical Review Letters*, *54*, 1872-1874. doi: 10.1103/ PhysRevLett.54.1872

Rambo, P. W., Ambrosiano, J. J., Friedman, A., & Nielsen, D. E., Jr. (1989, July). Temporal

and spatial filtering remedies for dispersion in electromagnetic particle codes. In *Presented at the 13th conference on the numerical simulation of plasmas, santa fe, nm, 17-20 sep. 1989.*

Riquelme, M. A., & Spitkovsky, A. (2009, March). Nonlinear Study of Bell's Cosmic Ray Current-Driven Instability. ApJ, *694*, 626-642. doi: 10.1088/0004-637X/694/1/626

Riquelme, M. A., & Spitkovsky, A. (2011, May). Electron Injection by Whistler Waves in Non-relativistic Shocks. ApJ, *733*, 63. doi: 10.1088/0004-637X/733/1/63

Rothenflug, R., Ballet, J., Dubner, G., Giacani, E., Decourchelle, A., & Ferrando, P. (2004, October). Geometry of the non-thermal emission in SN 1006. Azimuthal variations of cosmic-ray acceleration. A&A, *425*, 121-131. doi: 10.1051/0004-6361:20047104

Sagdeev, R. Z. (1966). Cooperative Phenomena and Shock Waves in Collisionless Plasmas. *Reviews of Plasma Physics*, *4*, 23.

Savoini, P., & Lembege, B. (1994, April). Electron dynamics in two- and one-dimensional oblique supercritical collisionless magnetosonic shocks. J. Geophys. Res., *99*, 6609-6635. doi: 10.1029/93JA03330

Schmitz, H., Chapman, S. C., & Dendy, R. O. (2002a, November). Electron Preacceleration Mechanisms in the Foot Region of High Alfvénic Mach Number Shocks. ApJ, *579*, 327-336. doi: 10.1086/341733

Schmitz, H., Chapman, S. C., & Dendy, R. O. (2002b, May). The Influence of Electron Temperature and Magnetic Field Strength on Cosmic-Ray Injection in High Mach Number Shocks. ApJ, *570*, 637-646. doi: 10.1086/339787

Schneiter, E. M., Velázquez, P. F., Reynoso, E. M., & de Colle, F. (2010, October). An MHD study of SN 1006 and determination of the ambient magnetic field direction. MNRAS, *408*, 430-435. doi: 10.1111/j.1365-2966.2010.17125.x

Schneiter, E. M., Velázquez, P. F., Reynoso, E. M., Esquivel, A., & De Colle, F. (2015, May). 3D MHD simulation of polarized emission in SN 1006. MNRAS, *449*, 88-93. doi: 10.1093/mnras/stv279

Schopper, R., Thorsten Birk, G., & Lesch, H. (2002, June). High-energy hadronic acceleration in extragalactic radio jets. *Astroparticle Physics*, *17*, 347-354. doi: 10.1016/S0927-6505(01)00156-6

Seo, E. S., Ormes, J. F., Streitmatter, R. E., Stochaj, S. J., Jones, W. V., Stephens, S. A., & Bowen, T. (1991, September). Measurement of cosmic-ray proton and helium spectra during the 1987 solar minimum. ApJ, *378*, 763-772. doi: 10.1086/170477

Shaisultanov, R., Lyubarsky, Y., & Eichler, D. (2012, January). Stream Instabilities in Relativistically Hot Plasma. ApJ, *744*, 182. doi: 10.1088/0004-637X/744/2/182

Shimada, N., & Hoshino, M. (2000, November). Strong Electron Acceleration at High Mach Number Shock Waves: Simulation Study of Electron Dynamics. ApJ, *543*, L67-L71. doi: 10.1086/318161

Shklovskii, I. S. (1953). *Radioastronomiia.*

Slane, P., Lee, S.-H., Ellison, D. C., Patnaude, D. J., Hughes, J. P., Eriksen, K. A., ... Nagataki, S. (2014, March). A CR-hydro-NEI Model of the Structure and Broadband Emission from Tycho's Supernova Remnant. ApJ, *783*, 33. doi: 10.1088/0004-637X/783/1/33

Smets, R., Delcourt, D., & Fontaine, D. (1998, September). Ion and electron distribution functions in the distant magnetotail: modeling of Geotail observations. J. Geophys. Res., *103*, 20407-20418. doi: 10.1029/98JA01369

Speiser, T. W. (1965, September). Particle Trajectories in Model Current Sheets, 1, Analytical Solutions. J. Geophys. Res., *70*, 4219-4226. doi: 10.1029/JZ070i017p04219

Stroman, T., Pohl, M., & Niemiec, J. (2009, November). Kinetic Simulations of Turbulent Magnetic-Field Growth by Streaming Cosmic Rays. ApJ, *706*, 38-44. doi: 10.1088/0004 -637X/706/1/38

Su, M., Slatyer, T. R., & Finkbeiner, D. P. (2010, December). Giant Gamma-ray Bubbles from Fermi-LAT: Active Galactic Nucleus Activity or Bipolar Galactic Wind? ApJ, *724*, 1044-1082. doi: 10.1088/0004-637X/724/2/1044

Swann, W. F. (1933, February). A Mechanism of Acquirement of Cosmic-Ray Energies by Electrons. *Physical Review*, *43*, 217-220. doi: 10.1103/PhysRev.43.217

Tavani, M., Giuliani, A., Chen, A. W., Argan, A., Barbiellini, G., Bulgarelli, A., ... Salotti, L. (2010, February). Direct Evidence for Hadronic Cosmic-Ray Acceleration in the Supernova Remnant IC 443. ApJ, *710*, L151-L155. doi: 10.1088/2041-8205/710/2/L151

Tidman, D. A., & Krall, N. A. (1971). *Shock waves in collisionless plasmas.*

Treumann, R. A. (2009, December). Fundamentals of collisionless shocks for astrophysical application, 1. Non-relativistic shocks. A&A Rev., *17*, 409-535. doi: 10.1007/s00159-009 -0024-2

Ucer, D., & Shapiro, V. D. (2001, August). Unlimited Relativistic Shock Surfing Acceleration. *Physical Review Letters*, *87*(7), 075001. doi: 10.1103/PhysRevLett.87.075001

Uchiyama, Y., Aharonian, F. A., Tanaka, T., Takahashi, T., & Maeda, Y. (2007, October). Extremely fast acceleration of cosmic rays in a supernova remnant. Nature, *449*, 576-578. doi: 10.1038/nature06210

Umeda, T., Kidani, Y., Matsukiyo, S., & Yamazaki, R. (2014, February). Dynamics and microinstabilities at perpendicular collisionless shock: A comparison of large-scale two-dimensional full particle simulations with different ion to electron mass ratio. *Physics of Plasmas*, *21*(2), 022102. doi: 10.1063/1.4863836

Umeda, T., Omura, Y., Tominaga, T., & Matsumoto, H. (2003, December). A new charge conservation method in electromagnetic particle-in-cell simulations. *Computer Physics Communications*, *156*, 73-85. doi: 10.1016/S0010-4655(03)00437-5

Umeda, T., Yamao, M., & Yamazaki, R. (2008, July). Two-dimensional Full Particle Simulation

of a Perpendicular Collisionless Shock with a Shock-Rest-Frame Model. ApJ, *681*, L85. doi: 10.1086/590408

Umeda, T., Yamao, M., & Yamazaki, R. (2009, April). Electron Acceleration at a Low Mach Number Perpendicular Collisionless Shock. ApJ, *695*, 574-579. doi: 10.1088/0004-637X/695/1/574

Vay, J. L. (2008, May). Simulation of beams or plasmas crossing at relativistic velocity. *Physics of Plasmas*, *15*(5), 056701. doi: 10.1063/1.2837054

Villasenor, J., & Buneman, O. (1992, March). Rigorous charge conservation for local electromagnetic field solvers. *Computer Physics Communications*, *69*, 306-316. doi: 10.1016/0010-4655(92)90169-Y

Vink, J. (2012, December). Supernova remnants: the X-ray perspective. A&A Rev., *20*, 49. doi: 10.1007/s00159-011-0049-1

Wang, X., Filippenko, A. V., Ganeshalingam, M., Li, W., Silverman, J. M., Wang, L., . . . Wong, D. S. (2009, July). Improved Distances to Type Ia Supernovae with Two Spectroscopic Subclasses. ApJ, *699*, L139-L143. doi: 10.1088/0004-637X/699/2/L139

Webber, W. R. (1998, October). A New Estimate of the Local Interstellar Energy Density and Ionization Rate of Galactic Cosmic Cosmic Rays. ApJ, *506*, 329-334. doi: 10.1086/306222

Weibel, E. S. (1959, February). Spontaneously Growing Transverse Waves in a Plasma Due to an Anisotropic Velocity Distribution. *Physical Review Letters*, *2*, 83-84. doi: 10.1103/PhysRevLett.2.83

West, J. L., Safi-Harb, S., Jaffe, T., Kothes, R., Landecker, T. L., & Foster, T. (2016, March). The connection between supernova remnants and the Galactic magnetic field: A global radio study of the axisymmetric sample. A&A, *587*, A148. doi: 10.1051/0004-6361/201527001

Wibig, T., & Wolfendale, A. W. (2004, October). At what particle energy do extragalactic cosmic rays start to predominate? *ArXiv Astrophysics e-prints*.

Wieland, V., Pohl, M., Niemiec, J., Rafighi, I., & Nishikawa, K.-I. (2016, March). Nonrelativistic Perpendicular Shocks Modeling Young Supernova Remnants: Nonstationary Dynamics and Particle Acceleration at Forward and Reverse Shocks. ApJ, *820*, 62. doi: 10.3847/0004-637X/820/1/62

Winske, D., & Quest, K. B. (1988, September). Magnetic field and density fluctuations at perpendicular supercritical collisionless shocks. J. Geophys. Res., *93*, 9681-9693. doi: 10.1029/JA093iA09p09681

Wu, C. S. (1984, October). A fast Fermi process - Energetic electrons accelerated by a nearly perpendicular bow shock. J. Geophys. Res., *89*, 8857-8862. doi: 10.1029/JA089iA10p08857

Yamazaki, R., Kohri, K., Bamba, A., Yoshida, T., Tsuribe, T., & Takahara, F. (2006, October). TeV γ-rays from old supernova remnants. MNRAS, *371*, 1975-1982. doi: 10.1111/j.1365-2966.2006.10832.x

Yee, K. (1966, May). Numerical solution of inital boundary value problems involving maxwell's equations in isotropic media. *IEEE Transactions on Antennas and Propagation*, *14*, 302-307. doi: 10.1109/TAP.1966.1138693

Zatsepin, G. T., & Kuzmin, V. A. (1966). Upper limit of the spectrum of cosmic rays. *Sov Phys JETP Lett*, *4*, 78-80.